

Precise 3-D Localization and Simulation of Topographic Objects in Synthetic Aperture Radar Images

Vorgelegt von

M.Sc.

Adnan Saeed

geb. in Rawalpindi, Pakistan

von der Fakultät IV - Elektrotechnik und Informatik
der Technischen Universität Berlin

zur Erlangung des akademischen Grades

Doktor der Ingenieurwissenschaften

- Dr.-Ing. -

genehmigte Dissertation

Promotionsausschuss:

Vorsitzender: Prof. Dr. Marc Alexa

Gutachter: Prof. Dr.-Ing. Olaf Hellwich

Gutachter Prof. Dr.-Ing. Rolf Schuhmann

Gutachter: Prof. Dr.-Ing Omar Siddiqui (Taibah University, Saudi-Arabien)

Tag der wissenschaftlichen Aussprache: 12 December 2018

Berlin 2018

Acknowledgement

My most humble and sincere thanks to Allah Almighty, with his divine grace, help and mercy I was able to complete my work. May Allah help us to perform our duties, to strengthen us on the path of righteous and to guide us towards all that will bring good to us here and hereafter.

My gratitude to my supervisor Prof. Dr. Olaf Hellwich, without his help and guidance it would not have been possible for me to complete this work in time. I found him finest as a person and as a mentor in terms of scientific and even personal support. The skills and knowledge I have gained throughout this period, I perceive it as a valuable asset of my life. As an expression of gratitude, I beg to dedicate it to his name. He has always judged me liberally, I hope he will judge these pages in the same spirit.

I thank my parents, my mother (Tallat Saeed) who is and will be a support in every exam of my life. My father (Kh. Saeed Uddin) whose presence made me felt strong and I especially thank my wife, Warda Adnan, for the constant support and encouragement she has given me throughout to achieve me my goal and taken unsurpassed care of our children Mustafa and Mujtaba.

Abstract

The geometric localization accuracy for Terrasar-X resulting due to very precise orbit determination is a prominent feature in the current generation of SAR satellites. If the most prominent error sources are accounted for, the 2-D position of targets can be estimated with high accuracy. Such a method is referred to as SAR geodesy. Having two such acquisitions from different orbits, a 3-D position can be retrieved by a method called stereo SAR. In a SAR image, visibility of a unique scatterer from different orbits, especially ascending and descending is not very common. To overcome this obstacle a unique designed corner reflector pair, visible in cross heading orbits is deployed and its positioning accuracy is estimated. It was demonstrated that high accuracy of satellite orbit localization can be transferred to image-based positioning not only in 2-d but also in 3-d space.

Electromagnetic surface characteristics were estimated by use of CST software of computer simulation technology, Darmstadt. A novel SAR simulation technique, using this general-purpose electromagnetic simulation software, CST, was implemented which allowed us to vary radiometric sensor characteristics as well as material properties for the modeled objects. A complete SAR processing algorithm was also implemented which processed the data that resulted from such a simulation. The developed simulator was not able to handle larger real-world objects and computational resources were depleted with manifold increase in memory requirement with a little increase in the object size. Hence only small sized objects and basic geometric shapes were simulated and tested with this simulator.

For large building and bigger man-made objects, a previously developed, direct SAR image simulation technique, was used to simulate a model from cross-directional orbits. The main goal of having different orbital directions was detection and identification of common scattering points in the SAR image obtained from different geometries. Ultimately, a better understanding of the appearance of the regular patterns in the SAR images, by the urban buildings was resulted.

Several case studies were performed for buildings in Berlin and Potsdam. Precise digital 3d models were developed using a combination optical, laser and geodetic measurements and then they were simulated. Different materials such as glass, metal, concrete and ceramic were grouped into different layers with different electromagnetic and reflection properties. The simulated phase centers were mapped onto the building facades and hence localizing the origin of the signal from the modeled structure. As predicted, corner reflections that occurred at the window corners were of strongest amplitude whereas direct and diffuse reflections were minimal. When multiple bounce reflections were considered, it revealed a regular pattern where the scatterer appeared to occur below the ground level in the SAR image, thus explaining the unknown SAR image characteristics.

Zusammenfassung

Die geometrische Lokalisationsgenauigkeit für Terrasar-X, die auf einer sehr präzisen Bahnbestimmung beruht, ist ein herausragendes Merkmal der aktuellen Generation von SAR-Satelliten. Wenn die prominentesten Fehlerquellen berücksichtigt werden, kann die 2-D-Position von Zielen mit hoher Genauigkeit geschätzt werden. Eine solche Methode wird als SAR-Geodäsie bezeichnet. Wenn zwei solcher Erfassungen von verschiedenen Umlaufbahnen stammen, kann eine 3-D-Position durch eine Methode, die als Stereo-SAR bezeichnet wird, abgerufen werden. In einem SAR-Bild tritt die Sichtbarkeit eines einzigen Streuers aus verschiedenen Umlaufbahnen, insbesondere aufsteigend und absteigend, nicht sehr häufig auf. Um dieses Problem zu überwinden, wird ein neu entworfenes Eckreflektorpaar verwendet, das in Kreuzkursbahnen sichtbar ist und dessen Positionierungsgenauigkeit geschätzt wird. Es konnte gezeigt werden, dass die hohe Genauigkeit der Satellitenorbitbestimmung nicht nur im 2-d, sondern auch im 3-d-Raum auf die bildbasierte Positionierung übertragen werden kann.

Elektromagnetische Oberflächeneigenschaften wurden durch Verwendung der CST-Software der Computer-Simulationstechnik, Darmstadt, geschätzt. Eine neuartige SAR-Simulationstechnik unter Verwendung dieser allgemeinen elektromagnetischen Simulationssoftware, CST, wurde implementiert. Diese ermöglichte es uns, radiometrische Sensoreigenschaften sowie Materialeigenschaften für die modellierten Objekte zu variieren. Die resultierenden Simulationsdaten wurden mit einem speziell dafür implementierten SAR-Verarbeitungsalgorithmus ausgewertet. Der entwickelte Simulator war nicht in der Lage, größere Objekte aus der realen Welt zu handhaben, und die Rechenressourcen wurden bereits bei einer Zunahme des Speicherbedarfs bei einer kleinen Vergrößerung der Objektgröße erschöpft. Daher wurden mit diesem Simulator nur kleine Objekte und geometrische Grundformen simuliert und getestet.

Für große Gebäude und größere künstliche Objekte wurde eine zuvor entwickelte, direkte SAR-Bild-Simulationstechnik verwendet, um ein Modell aus querverlaufenden Umlaufbahnen zu simulieren. Das Hauptziel unterschiedlicher Orbitalrichtungen war die Erkennung und Identifizierung von gemeinsamen Streupunkten im SAR-Bild, die sich aus verschiedenen Geometrien ergeben. Letztendlich wurde ein besseres Verständnis für das Erscheinungsbild der durch städtischen Gebäude verursachten regelmäßigen Muster in den SAR-Bildern möglich.

In Berlin und Potsdam wurden mehrere Fallstudien anhand von Gebäuden und Kuppeln, von denen präzise digitale 3D-Modelle durch eine Kombination von optischen, Laser- und geodätischen Messungen erstellt wurden, durchgeführt. Verschiedene Materialien wie Glas, Metall, Beton und Keramik wurden in verschiedene Schichten mit unterschiedlichen elektromagnetischen und Reflexionseigenschaften gruppiert. Die simulierten Phasenzentren wurden auf die

Gebäudefassaden abgebildet und lokalisieren so den Ursprung des Signals in der modellierten Struktur. Wie vorhergesagt, hatten Eckenreflexionen, die an Fensterecken auftraten, die stärkste Amplitude, während direkte und diffuse Reflexionen minimal waren. Wenn Triple Bounce betrachtet wurde, zeigte sich ein regelmäßiges Muster, bei dem der Streuer unterhalb des Bodens im SAR-Bild auftrat, wodurch die unbekanntes SAR-Bildeigenschaften erklärbar werden.

Table of Contents

Chapter 1

1.1. Motivation	1
1.2. Most Relevant Work (State of the art)	2
1.3. Reader's Guide	6

Chapter 2

2.1. Synthetic Aperture Radar: An Overview	7
2.2. Raw data Generation	8
2.2.1. Raw data Generation: The Echo	9
2.2.2. Raw data Generation: Pulse Sampling Requirements	10
2.2.3. Raw data Generation: Pulsed Radar Operation	10
2.2.4. Raw data Generation: Pulse Repetition Frequency	11
2.2.5. Raw data Generation: 2-D Array	12
2.2.6. Raw data Generation: Impulse Response	13
2.3. SAR Processing	15
2.3.1. SAR Processing: Focusing	15
2.3.2. SAR Processing: Complex SAR Signal	17
2.3.3. SAR Processing: Block Diagram	18
2.3.4. SAR Processing: Doppler Frequency & Bandwidth	20
2.3.5. SAR Processing: Matched Filtering (Illustrative)	22
2.3.6. SAR Processing: Frequency Domain	25
2.3.7. SAR Processing: Point Target Response	26
2.3.8. SAR Processing: Range Cell Migration (RCM) and Correction	28
2.3.9. SAR Processing: Speckle Effect	29
2.3.10. SAR Processing: Multibook Processing	31
2.4. Special Imaging Mode: ScanSAR, Spotlight	33

Chapter 3

3.1. TerraSAR-X's Orbital Accuracy and Keynotes	36
3.1.1. The TSX Multimode SAR Processor (TMSP)	37
3.1.2. Level 1b Products and Annotations	39
3.1.3. Corrections and Geometric Accuracy	39

3.1.4.	Azimuthal Localization	40
3.1.5.	Range Localization	40
3.2.	Double Corner Reflector (DCR)	41
3.2.1.	Use of Corner Reflectors in Remote Sensing	41
3.2.2.	Bi-Directional corner reflector	42
3.2.3.	RCS Simulations using CST	42
3.2.4.	CR deviation from theoretical perfection	44
3.2.5.	Construction and Mounting DCR's	47
3.2.6.	Azimuthal Orientation	51
3.2.7.	Elevational Orientation	52
3.3.	Localization Method and Accuracy	52
3.3.1.	Point Target Analysis (PTA).....	53
3.3.2.	Orbital Interpolation	54
3.3.3.	Space Intersection.....	55
3.3.4.	Atmospheric and other Corrections	57
3.4.	Results and Discussion	59

Chapter 4

4.1.	Introduction	62
4.1.1.	Need for Simulation	62
4.1.2.	Comparison and Motivation for CST	63
4.2.	Simulation Workflow	68
4.2.1.	Coordinate System and Units	68
4.2.2.	Materials	68
4.2.3.	Modelling 3-d Structures	70
4.2.4.	Boundaries and Symmetry	71
4.2.5.	Excitation Signal.....	73
4.3.	Solvers Overview	74
4.3.1.	Time Domain Solver	75
4.3.2.	Frequency Domain Solver	76
4.3.3.	Asymptotic Solver	77
4.4.	SAR Processing	77
4.4.1.	Complex TSX's Focusing Algorithm	77
4.4.2.	Simplified SAR Range Doppler Algorithm for Simulation	79

4.4.3.	Single Target Simulation (Sphere).....	80
4.4.4.	Single Target Simulation (Corner Reflector).....	84
4.4.5.	Multiple Targets Simulation	88
4.5.	Limitations of Time and Size	90
4.5.1.	Understanding the MESH	90
4.5.2.	Accounting for Error Sources.....	92
Chapter 5		
5.1.	POV-Ray and its Modelling Environment	93
5.2.	Introduction to RaySAR.....	94
5.2.1.	SAR Adaptation in RaySAR	95
5.2.2.	Reflection Bounce Count	96
5.3.	CAD Modelling Using Blender and Case Studies.....	98
5.3.1.	Technical University Berlin ‘T-Building’.....	98
5.3.2.	Simplified Dome, Potsdam.....	104
5.3.3.	Dome, Charlottenburg Palace, Berlin	106
5.3.4.	The Snake Building, Berlin	108
Chapter 6		
6.1.	Summary	112
6.2.	Future work.....	113
6.2.1.	Modification and Testing of SAR Algorithms	113
6.2.2.	Calculation of ITRF Coordinates for the Scatterers.....	113
6.2.3.	Localization with Pole-Base	113
Appendix		116
Pov-Ray Modelling.....		116
References.....		118
List of Figures		123
List of Tables.....		127
List of Abbreviations		128

Chapter 1: Introduction

1.1. Motivation

A two-dimensional SAR image coordinate vector in combination with three-dimensional satellite antenna positions given in a global reference frame provides two constraints to determine the three unknown coordinates of a point on the earth surface in a global reference frame, i.e. they are limiting the unknown location of the point to the “range circle”. Two images from e.g. ascending and descending orbits allow to estimate the point coordinates by intersecting the range circles.

SAR satellite image data is provided with an image resolution in the 1m range. Compared to this, the satellite orbit data is determined with an accuracy an order of magnitude better, i.e. in the 1 dm range or better. Therefore, the global positioning accuracy of imaged objects depends both on the accuracy of the orbit and on the accuracy of the localization of the object in the images. One might expect that object position accuracy from SAR is limited by the comparatively low image resolution. However, previous work (Balss *et al.*, 2014), (Eineder *et al.*, 2011), (Cong *et al.*, 2012), (Balss *et al.*, 2013), has demonstrated that in case of corner reflectors positioning accuracies in the range of the orbit accuracy may be achieved. This is being made possible by the exceptional signal strength and the detailed given knowledge with respect to the signal model of corner reflectors in the image.

In this thesis we want to demonstrate positioning of objects in a global reference frame with help of SAR imagery not only for corner reflectors but also for weaker while still well-pronounced signals stemming from more natural objects. Such objects could be for instance small ensembles of roofs and walls.

The base allowing to achieve this goal is that the object's image can be simulated, as soon as object geometry and sensor orientation with respect to the object are known. Seen from that point of view the image is a function of the object parameters and the sensor orientation parameters. When the sensor orientation parameters and the image are given, the unknown object parameters can be solved for – provided the function is invertible, which is possible in principle as soon as two or more images from different viewing directions are available. The accuracy of the solution can be high even if the spatial resolution of the image is low as long as the radiometric parameters of the image are sensitive to and dominated by the object parameters to be solved for.

As opposed to previous approaches, in this thesis we do not only want to demonstrate that the high accuracy of satellite orbits can be successfully transferred to image-based positioning, but we also want to investigate positioning in 3D. This should enable geodesy to integrate the resulting positions into geodetic networks, e.g. resulting

from DORIS, GPS, SLR, and VLBI measurements, and finally, densify existing networks. We want to demonstrate such geodetic applications by:

- using ascending and descending orbit data from compact objects to determine the 3D position of these objects, and
- comparing the 3D positions with results of fully geodetic approaches.

Finally, further benefit for geodesy will be that, via the generation of simulated SAR images and subsequent correlation with acquired real images, our approach allows to obtain precise global coordinates for geo-objects whose geometry is known in detail.

In the following we summarize the state of the art regarding the domains mentioned. Regarding the terminology used, “identification” will be used to address recognition of an object in an image, “localization” will be used for determining image coordinates of an object, and “positioning” will refer to the computation of 3-D object space coordinates, here in ITRF.

1.2. Most Relevant Work (State of the art)

Due to the availability of high-accuracy orbit data for the TerraSAR-X (TSX) satellite it is possible to use it as a measurement device that achieves accuracies in the range of a few centimeters. This has initially been demonstrated by (Eineder *et al.*, 2011) and further elaborated by (Cong *et al.*, 2012) for the exemplary objects of corner reflectors whose coordinates have been determined by independent reference measurements. In their work comparisons between SAR and reference measurements have been conducted by projecting the reference coordinates onto the line of sight of the SAR sensor. The performance of the approach has been evaluated by (Balss *et al.*, 2013) and in particular (Gisinger *et al.*, 2015).

In the same work it has been demonstrated that repeated measurement at identified homologous points allowed to observe earth tide effects with centimeter accuracy – provided atmospheric effects are taken into account.

From the measurement configuration of (Eineder *et al.*, 2011) we can infer that not only points signaled by corner reflectors, but arbitrary points can be localized with comparable absolute accuracy – provided they are sufficiently salient in the image and identifiable in their natural environment. This includes the question where a point that has been geocoded accurately by SAR sensing is actually located w.r.t the object details a human observer on ground perceives, e.g. visually. For instance, it can most probably be assumed that the SAR-geocoded point is located with cm accuracy on the earth surface represented by a Digital Terrain Model while it is not possible to tell where it is located in relation to a corner of a house nearby. This is due to the fact that it is currently impossible to identify house corners in SAR images sufficiently well – while any point in

the image though being unidentifiable in the real world can be geocoded with cm accuracy.

Geocoding SAR image data is an issue for more than 20 years. Geocoding of the TSX data being of major interest in this thesis is treated by (Roth, Huber and Kosmann, 2004). More recent work was concerned with the combination of optical and SAR image data and the question which geocoding model to use (Zhang, Balz and Liao, 2012). Of major interest for the proposed thesis is the work of (Zhu *et al.*, 2014) who use tomographic SAR in combination with the above-mentioned approach suggested by (Eineder *et al.*, 2011). Their work focuses on determining the absolute positions of TomoSAR scatterers; however, comparable to us they mention the issue of point identification (in terms of the explanation given in the preceding paragraph) as a research issue unsolved so far. In addition, in this thesis we will concentrate on combining views from ascending and descending orbits with the help of given shape information about the object seen from different sides i.e. we will not limit our work on points being identifiable in both ascending and descending imagery, but e.g. pairs of points joint by known object geometries. Then accurate geocoding of objects by SAR will be possible substantially more frequently as also objects looking different from different sides could be handled.

Consequently, our work will require the ability to acquire detailed 3D models of the objects to be identified.

3-D models of single or several buildings and building blocks can be acquired with help of optical cameras, e.g. video cameras mounted on cars. In the image sequences loop closure information can be used to reduce errors occurring due to successive concatenation of camera view points along the camera path (Wefelscheid, Hänsch and Hellwich, 2012). Nevertheless, in a stereo model resulting from combination of many cameras deviations of the resulting model geometry from reality are unavoidable. Investigations have shown that a reconstruction accuracy in the sub-mm range can be achieved (Chang, Datchev and Habib, 2009). However, this does not mean that the goals of this thesis cannot be achieved. For our work it is particularly important that local accuracies (with respect to object sizes of several meters) are particularly high while global or regional reconstruction errors (comparison of points dozens of meters apart from each other) are of minor importance. Accuracy problems could also be eased by the use of laser scanners or markers serving as control points allowing to add “rigidity” to surface reconstructions.

Based on acquired/given object geometries SAR image data can be simulated for certain antenna positions. Then electromagnetic surface characteristics as well as radiometric sensor characteristics have to be taken into account. Methods with large computational efforts allow to simulate the SLC signal pixel by pixel considering all object details. For this purpose, we will make use of the CST software of Computer

Simulation Technology AG, Darmstadt. The software will allow to model scatterers of different materials arranged in variable geometries.

Relevant categorization in SAR simulation is made by (Franceschetti, Migliaccio and Riccio, 1995) introducing 'SAR Image simulator' and 'SAR raw data simulator'. In a SAR image simulator, the object of simulation is the image which is generated by appropriate input data with no availability of any intermediate product. SAR raw data simulators are developed in order to provide test data for processing algorithms or radiometric analysis. Another classification with regard to evaluation of backscattering is 'point' and 'extended scene' simulator. Point simulator is focused on system parameters and might rely upon an artificial scene. Extended scene simulator needs a more sophisticated backscattering model.

Image simulators are applied for the purpose of providing a priori knowledge about man-made objects. For instance, ray tracing methods are applied in (Wohlers *et al.*, 1980) simulating SAR image signature of airplanes. The main motive was to provide the test data for automated object identification. This simulation was limited to direct backscattering only. Recently, (Balz and Stilla, 2009) approximated the double reflection in his simulation approach. (Brunner *et al.*, 2011) presented a ray tracing approach for simulating appearance of basic building shapes.

RaySAR (Auer, Hinz and Bamler, 2010) is a 3-d SAR simulator based on ray tracing methods, implying an enhanced version of the open-source software POV-Ray for simulating radar signals in 3-d, i.e. azimuth, range, and elevation. As a result, the simulated signal contributions can be compared to object geometries reconstructed by interferometric SAR methods. The focus of the simulation concept is on local urban scenes imaged by very high-resolution (VHR) SAR sensors and on the geometric correctness of simulated signals. Random scattering is neglected as the main goal is to identify and understand deterministic reflection effects occurring at individual man-made objects. A combination of two basic reflection models is used to simulate the spatial distribution of diffuse and specular reflection signals. RaySAR provides images in two steps. First, the modeled scene is sampled by an enhanced version of the POV-Ray ray tracer. Thereafter, the detected signal contributions are imposed with a pixel grid and summed in order to derive the final image.

CohRaS (Coherent Raytracing SAR Simulator),(Hammer and Schulz, 2009), is a SAR simulator based on ray tracing methods. The ray tracer itself is based on the concept developed by (Amanatides and Woo, 1987). This simulator is intended mainly for the simulation of small scenes with high resolution for creating training data for classifiers and sample data for the training of image analysts. The only restriction imposed on the geometry of the 3D model, is that all polygons need to be convex. The focus is set on the fast calculation of many small images, as this is needed for classification.

SARViz (Balz and Stilla, 2009) is a real-time SAR image simulation system. The preface “real-time” is used in the computer graphics sense, which, in our case, means more than 20 simulations or frames per second. The size of each frame is typically 1024x768 pixels. SARViz uses the rasterization approach implemented on Graphics Processing Units (GPU), which allows very fast simulations, but has certain limitations regarding the geometric and the radiometric accuracy. For example, rasterization does not allow simulating multiple bounces, because the path of the waves throughout the scene is not known.

Simulators for providing raw data are based on physical models describing reflection phenomena. (Speck, Turchi and Süß, 2007) presented a raw data simulator based on separate models for 3-d objects such as buildings or vehicles and background.

The use of a *General-Purpose* EM simulator for simulating SAR is rare. Some of the basic experiments on the generic EM simulator FEKO, to test its suitability for the SAR simulation was done by (Mishra and Mulgrew, 2009). Their main focus was towards generating a synthetic aperture radar (SAR) image database of ground targets, using a generic EM simulator.

1.3. Reader's Guide

This thesis is structured as follows: Chapter-2 elaborates the basics on synthetic aperture radar technique with the required mathematics and detailed illustrations. This chapter is structured in an illustrative way focusing the readers with limited SAR knowledge. Chapter-3 details the information about the TSX satellite mission and then the method used to localize a target using a double directional reflector in the acquired TSX images. The accuracy of localization is also a segment of this chapter. Chapter-4 discusses the novel simulation technique using a general-purpose simulator to simulate SAR images and then it discusses its limitations of use with respect to time and computational resources required. Last chapter, chapter-5, models and simulates large scale man-made buildings for SAR images. Towards the end, new findings resulting from such simulations are discussed.

Chapter 2: Basics on Synthetic Aperture Radar

This chapter elaborates on the basic principle of Synthetic Aperture Radar (SAR). The current text is adapted from a lecture series by Prof Dr. Olaf Hellwich and Dr. Andreas Reighber presented at Technical University Berlin. Readers having sufficient SAR knowledge can skip this to the next chapter.

2.1. Synthetic Aperture Radar: An Overview

SAR always operates in the side looking geometry. Platform flies and the antenna looks in an inclined way onto the terrain right or left side of the flight path. It tries to form a long synthetic aperture that allows high resolution in range direction due to the frequency modulated impulse and in azimuth direction due to the frequency modulation that occurs as a consequence of the Doppler effect. From that, it follows that the resolution of SAR image is independent of the range of the objects from the antenna and that it is also independent of the wavelength being used. A smaller real antenna allows to synthesize a longer synthetic aperture, the shorter the antenna more widely open the antennas beam is which is why we see the same places on the surface of the earth for a longer time and that allows us to a generate a synthetic aperture to have many impulses being sent during which a specific object is visible. Those impulses are then used to focus synthetic beam to a high-resolution beam. However, spaceborne SAR typically provides a lower resolution than airborne SAR because of the signal-to-noise ratio constraints. We need to have a higher power that is achievable with a larger antenna. Not being able to use a smaller antenna limits the highest achievable resolution. In general, we can say it is a typical characteristic of SAR that from airplanes (close to the terrain) the resolution is higher than from satellite out in space.

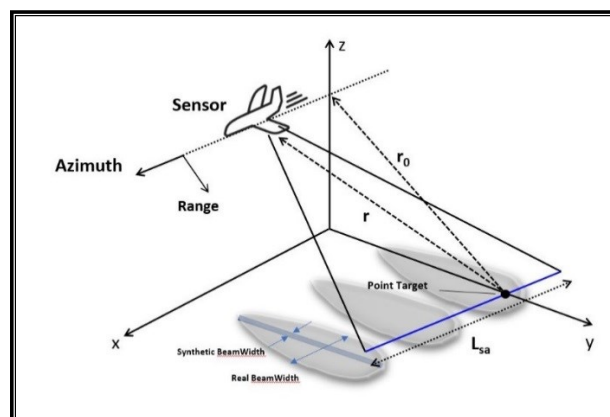


Figure 1 SAR Geometry

Figure 1 shows the basic geometry of SAR data acquisition, we see the platform(sensor) and it is looking in a side looking geometry onto the terrain. A swath is covered by the impulses this swath is also known as antennas footprint. In the case of real beam width, this footprint is quite large because we want to cover a wider field, more area on the earth surface. Then 'synthetic aperture' is used in order to generate a narrow synthetic beam width.

2.2. Raw data Generation

We observe 2-dimensional recording of the data on the ground with each of the impulse we are covering. By sending impulses repeatedly we are generating the second dimension of each image.

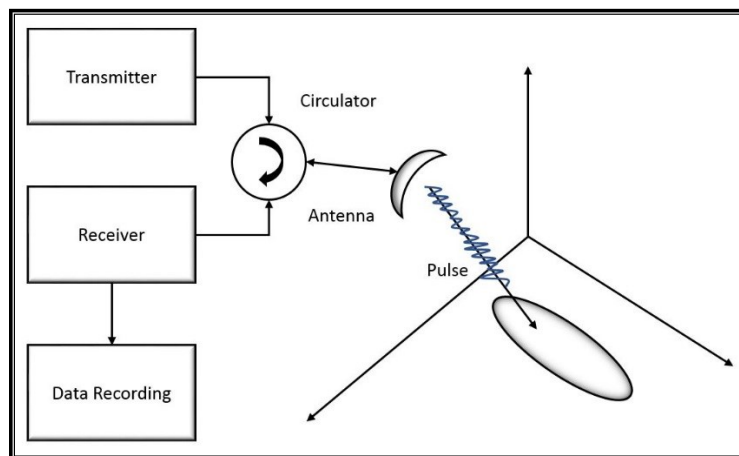


Figure 2 SAR Switching Operation

Initially, the antenna transmits the radar impulse, the circulator switches on to receive mode and when there is an echo coming back from the ground the Echo is recorded. Sometime later the next impulse is transmitted. Very basic switching operation is seen in the Figure 2.

The impulse travels down to the ground with speed of light, it is deflected on the ground, partially some of the radiation is absorbed and some is reflected in different directions. The energy that is backscattered in the direction of the sensor is recorded, that recorded energy is called the back-scattering cross-section or σ_0 , which is used as an abbreviation for the back-scattering cross-section. The term backscattering cross section refers to the interpretation of the reflection on the ground that is proportional to the size of an object we are seeing which is why the term 'cross-section' is being used.

After the reflection on the ground, the echo is recorded by the antenna which has been switched by the circulator in to the receive mode. In the receiver the signal is measured on the antenna, amplified, converted to a baseband, the result is digitized through an

analog-digital converter and recorded in local memory. That is some substantial signal processing by the radar sensor's hardware.

2.2.1. Raw data Generation: The Echo

The radar itself transmits an impulse into a spatial opening angle, we are having a wide-open antenna in azimuth direction it is even more opened vertical to azimuth. In azimuth direction, we want to see a certain section on the ground because that allows us to generate a long synthetic antenna and process the data that is showing the Doppler effect in order to achieve a higher resolution. So synthetically we get a very narrow beam in flight direction. But in the direction vertical to flight direction we want to have an even wider opening because that controls how wide the spots on the ground is which is covered by many impulses. Subsequently, we certainly prefer to cover a wider range on the ground because that is giving us big images and allowing us to see many parts of the earth's surface in the same image. At this point, one can say that the antenna is focused quite well in azimuth direction but badly in the elevation direction. The generated pulse should be very short in time, it is frequency modulated and emitted. It hits the ground and it starts reflecting in near range first and travel further over the swath last until it reaches far range. This latter part of echo is generated partially while the platform is moving towards the center. So, for a certain time after the emission, no echoes are received. Waiting after a fixed time it starts recording and that delay time is called range delay. The echoes from the path closer to the sensor arrive first and then those further away from the sensor arrive later. This results in an echo that it much longer than the originally emitted. The impulse sent (range direction) by the antenna is not that short because it may be frequency modulated. In other direction (azimuth), we are synthetically making it shorter. The echo is recorded with the high sampling rate, we have a high resolution in the range direction and therefore we have to sample the Echo with high frequency with many data samples for each impulse. The sensor does not only record's the amplitude but also the phase information. It means that the phase information in SAR is meaningful, telling us that it needs to be a coherent sensing method so the impulse that is generated and emitted into space contains coherent radiation. Coherent radiation means the phase of the signal emitted is under full control of technology. It is similar to a laser impulse, in coherent radiation at any time during the generation of the impulse we can say which phase over the wavelength it has at a specific time. So, if we are looking at the data itself this may be the curve of the echoes and each of the numbers we are recording represents the 'complex data sample' at one part in the curve. Complex meaning a point in the complex number plane consisting of a real and imaginary part or in other words in amplitude and phase angle. This is happening for every impulse, it is recorded for a particular time moment.

2.2.2. Raw data Generation: Pulse Sampling Requirements

The impulse is sent while the platform is flying and along with that direction, we are having a time which is the runtime towards the ground. So, the Echo shape of a single pulse is sampled in the receiver that means if we want to achieve a synthetic pulse duration τ_p , due to the use of a bandwidth B_r , than the sampling rate r_s needs to be larger than that bandwidth.

$$r_s \geq B_r = 1/\tau_p$$

If we want to have a resolution on the ground of 1m and record 2048 samples covering the range of a 2km, this corresponds to a range sampling rate of 150 MHz which is dominating the number of samples in the recorded data. The result of that forms one line of the raw data.

2.2.3. Raw data Generation: Pulsed Radar Operation

The SAR is operated as a pulsed radar, it is not necessarily so but for all the important systems its done in this way. Meaning that platform sends one impulse after the other that travels through the ground echo traveling back to the antenna and it is recorded by the antenna. Despite the fact that it is certainly not so, but it assumes that the sensor stops while impulse is hitting the ground echo is reflected and recorded. We do not have a model where the airplane is required to move between the emission and reception of the impulse.

The sensor has recorded some echo after some time, the sensor is located at a position x_0 plus travel speed time difference t , now the second line is recorded. A new microwave pulse is emitted which illuminates the new part of the swath much overlapping with the older pulse because we want to use the synthetic aperture principle. Again, echo is recorded and forms the second line of the data. Our simplification does not take into account distance covered by plane flying any further while the echo travels back and forth.

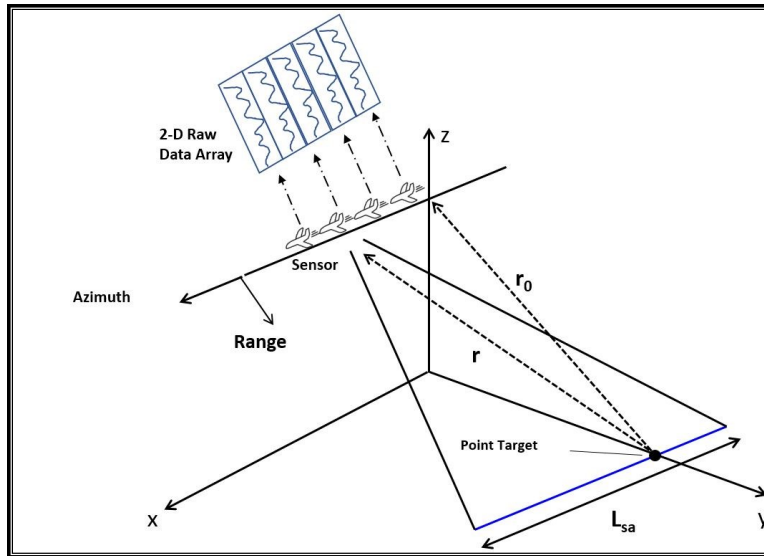


Figure 3 RAW data in a 2-D Array

In this way, we are recording the echoes of one impulse after the other, so we have a two-dimensional raw data array. Step by step the entire radar raw data is recorded and typically thousands of pulses are transmitted and received per second. In case of the real aperture radar image, everything is completed already and in the case of SAR, the case is much more complex because the post-processing of data is necessary. The so-called SAR processing is the formation of the synthetic aperture also called 'the focusing' because we are now taking the beam that is wide open in the azimuth direction and make it artificially narrow such that we can highly resolve the terrain on the ground. At the sensor, we are sending an impulse receiving an echo and so on, this does not theoretically happen that way but its technically necessary that the antenna does that exactly on the ground.

2.2.4. Raw data Generation: Pulse Repetition Frequency

There is a time difference between the two impulses being sent which governs pulse repetition frequency (PRF) and that time difference is $1/PRF$. As the sensor flies relatively fast it also quickly transmits many impulses, at the same time in between the pulses the echo has to be received. During transmission of the pulses no reception is possible otherwise there would be a mix between the emission and reception. So, the PRF is an important design parameter of the SAR system. The range between the platform and ground must fit this PRF. The signal travels with the speed of light and so the echo is arriving at the platform at a certain point in time and then no impulse is allowed to be sent because the sensor must be ready to record the echo. For satellite, several pulses are being emitted before the echo of the first impulse in a sequence comes back. If we are having PRF that is too high than necessarily we have to stop recording in time which is possibly making the observed swath smaller. We stop

recording despite the fact there's still some echo's coming back from the ground because sensor is already dedicated to the generation of the next impulse. If, however, the PRF is too low, the azimuth signal that is frequency modulated due to the Doppler effect is under sampled and we are not having enough samples in order to really see the effect of the frequency modulation. So, in the design of SAR, we cannot freely choose the PRF.

As seen in Figure 4 there is a sensor, it is looking sideways to the ground, there is the swath being covered, looking at a particular point in the middle of the swath that has range known as slant range from the sensor. The observation is made under a certain depression angle to the horizontal direction that is called ' θ ' here while the sensor is flying at a height ' h '.

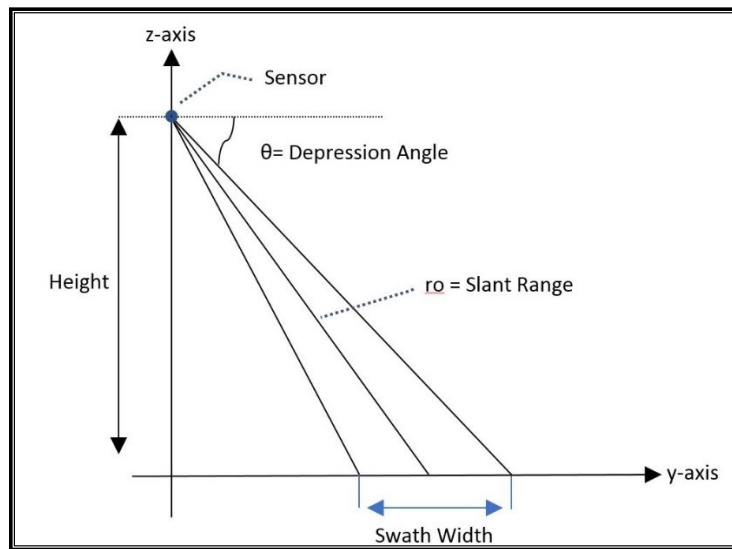


Figure 4 SAR Geometry 2-d Illustration

2.2.5. Raw data Generation: 2-D Array

Impulse after impulse we are receiving data, each echo has a certain number of samples, so the 2-d raw data is stored in a 2-d array of complex values (Figure 5). We are having two directions, that is the azimuth time t , going in X with respect to image and there is a range time, the runtime of the impulse τ . Typically the range time is called 'fast time' also because there we are confronted with the speed of light, and that fast time is related to slant ranges position. Time along the flight path is 'slow time' because it refers to the velocity of the sensor.

The sensor with its speed is bringing us to different positions along the azimuth direction and that is happening much slower, so typically fast time is measured in microsecond or millisecond and the flight time or slow time is measured in seconds or minutes.

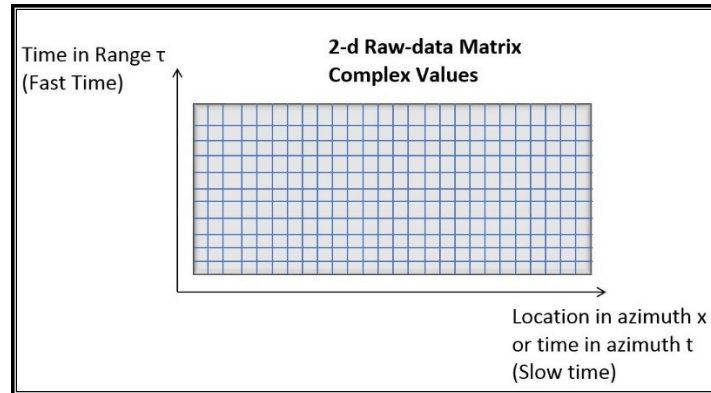


Figure 5 Raw Data Matrix

There is a relationship between fast time and the range of a particular sample, which is equal to half the speed of light times the run time of the impulse from the antenna to the ground and back to the receiver

$$r_s = c\tau/2$$

In the same way for the place along the flight path of the positions x is equal to velocity of the platform times the slow time along the flight path.

$$x = vt$$

2.2.6. Raw data Generation: Impulse Response

Referring to Figure 6, an airplane flying and sending a frequency modulated chirp that records a certain place on the ground and because the antenna is widely opened the antenna footprint is large. If there are many impulses generated along the flight path than due to the wide opening of the beam, we see the effect of objects on the ground over longer flight distance. If there's a point on the ground like this building on a plain only and we are recording the raw data, we can see the impact of the house for a longer time.

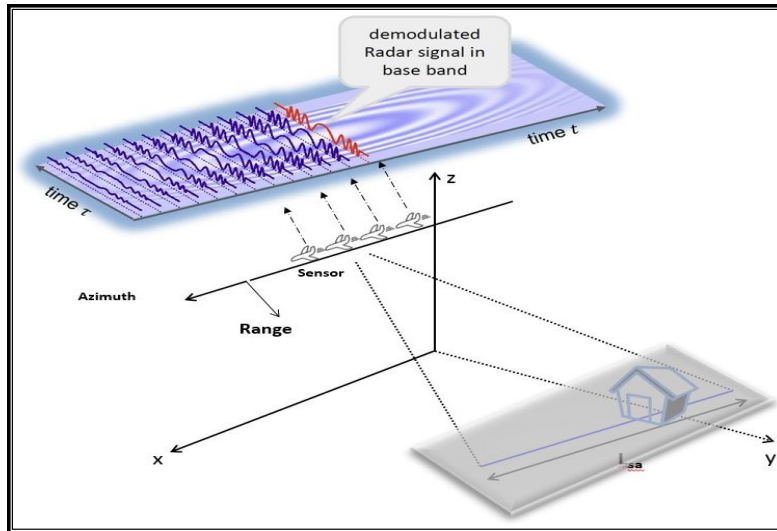


Figure 6 Single house target visualization

The echo from the ground is influenced by the echo that is stemming from the house because its inside of the beam and reflecting the parts of the echo for that longer flight distance. The signal shown here is the demodulated radar signal in the baseband that is a part of the hardware data processing of the sensor and as a consequence of the generation of this simple visualization, we can see echo as if the building is a single point in an otherwise empty space. Nothing much is happening as long as we are not seeing anything on the ground but then the lowest point on the ground gets into the beam and we are having an effect on the data. We see (Error! Reference source not found., top) the waves going from white to black are changing fast they are having a short wavelength meaning that the frequency is increased during the approach to the objects and then the distance does not change and hence the frequency does not change.

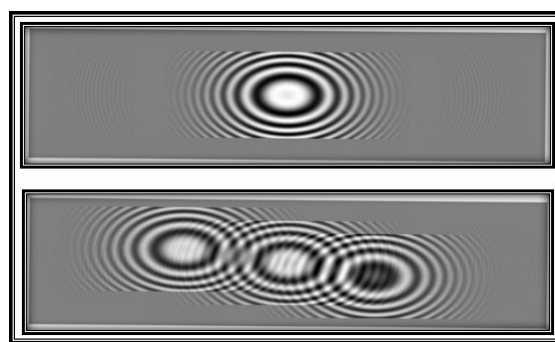


Figure 7 One (top) and Three (bottom) point targets Raw Data

There is the longer part where the recorded signal doesn't change much because the distance remains the same and after that we are flying away from the point on the ground there we are having a frequency modulation impact; the signal has decreased frequency with relation to the original signals frequency. To end, it gets darker as we do not see anything anymore. At the corners its quite dark because terrain is absolutely

flat, and the energy is reflected away from the sensor. In other words, this data set is recorded from a single point reflecting which is located in an empty volume. For a simulated data set of the very simple scenery of three points only, the raw dataset is also shown (**Error! Reference source not found.**, bottom).

2.3. SAR Processing

Up till now we have discussed the geometry, layout and discussed the acquisition method for a basic SAR system. After acquiring the scattered electromagnetic data, a series of processing steps are required which will convert the obtained RAW data into a focused SAR image. Following are some steps common in almost all SAR processing algorithms.

2.3.1. SAR Processing: Focusing

In the first step of SAR processing, we do the range compression by matched filtering with the reference function that tells us how every impulse was frequency modulated. The resulting range compressed data for three targets is visualized (Figure 8, center).

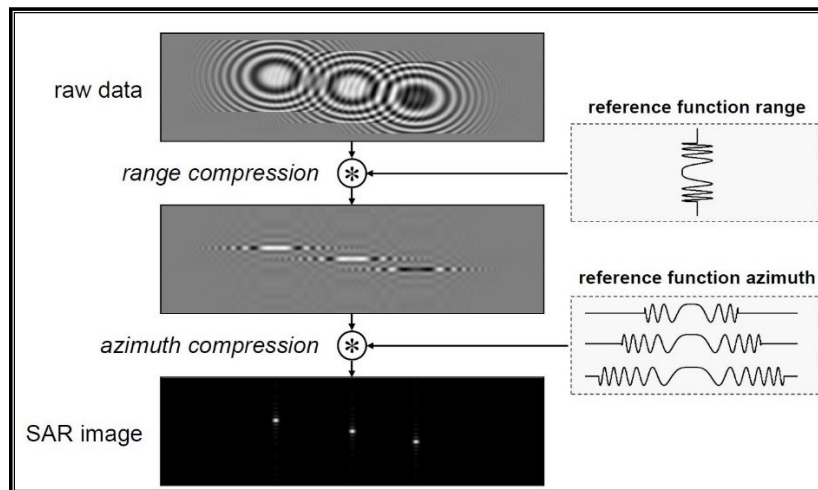


Figure 8 SAR Focusing

In range direction, perpendicular to the flight path we are already seeing a high spatial resolution. We can easily pinpoint each of the points on the ground with better accuracy than while it was still as blurry in the raw data, now we already have a high resolution in the range direction. We have to do a second match filtering operation that uses a frequency modulation due to the natural Doppler effect. The beam goes into a certain spatial angle in the near range we are seeing a smaller part of the ground in each of the beams and therefore the frequency modulation happens over a smaller distance while in far range the frequency modulation is happening over a longer distance. For each and every distance range in the dataset, we have to use a different reference function when we do the matched filtering in the azimuth direction.

We need to have reference function for the point that is closer to us that shown here and for the point that is further away we have other reference function (Figure 8, right bottom).

After the SAR processing, we see high-resolution image where each and every one of these simple objects have become a little point in the dataset (Figure 8, bottom).

The second matched filtering (azimuth) is the actual SAR technique. In SAR we are making use of the same kind of computation twice with range compression and azimuth compression but classically the 'Synthetic Aperture' is happening in the azimuth direction.

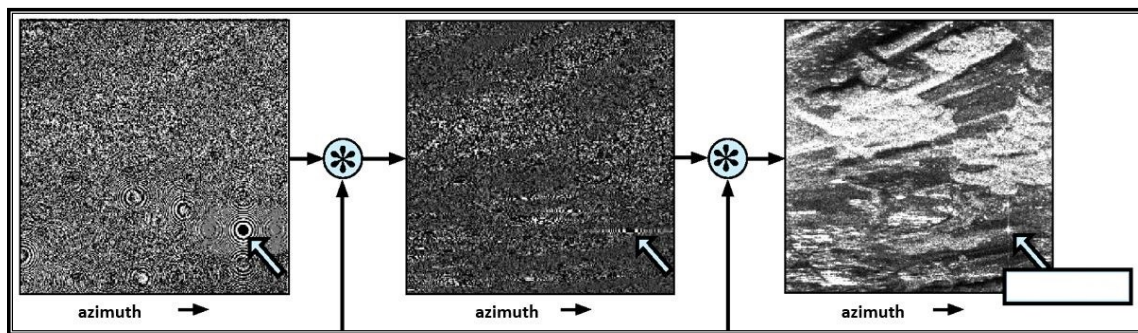


Figure 9 SAR Processing real dataset

The last example was a very simple example, Figure 9 shows the similar processing but on a real-world dataset. In the raw data, we are frequently not seeing much detail because the data is very low resolution sometimes if there's a very strong reflector we can see that in the unprocessed raw data. Here (Figure 9, left pointer) is a structure in the raw data quite visible, we can only visualize the amplitude part of the data because we are not able to show both phase and amplitude for a human eye. We see one very bright spot and after range compression, it is already in focus in range direction.

Then follows the azimuth compression, we see (Figure 9, right) the image having the full resolution and a bright point is so-called point target which may be a corner reflector that is of use in SAR technology. In order to provide control point information which has highly accurate coordinates determined by surveying methods a corner reflector is used. The direct result of the data recording is originally not what we call an image it is rather a mix of data in which we do not see anything. The raw data needs to be transformed to image data by a SAR processor. The step of the formation of the synthetic aperture by the artificial enlargement of the antenna length is done in this matched filtering operation.

It is computationally quite expensive. The result is then a high-resolution SAR image, which is again a matrix of complex values called 'single look complex image' (SLC). For

each and every pixel in the image, we do not only have the grey values shown here but we are also having a phase information so each pixel in the image is one point in the complex number plane. Essential is the exploitation of the characteristic shape of the received signal and we are making particularly use of the phase history.

2.3.2. SAR Processing: Complex SAR Signal

To summarize, we are having a sensor for generating a coherent signal we are recording the Echo with respect to amplitude and phase and each and every point on the ground is seen over by many recorded pulses.

The backscattering is a linear superposition of the contributions of all illuminated objects. We imagined for the sake of simplicity a single reflecting point in an empty volume but certainly this is not true with respect to the surface of the earth. For a real-world we may have millions of points and all the points reflects simultaneously when they are illuminated by the radar's antenna. The recorded data always contains all the contributions of all these points.

The SAR processing i.e. the focusing operation are two match filtering operations they have to make sure that all these contributions of the illuminated objects are separated from each other again. The processing is a mathematically linear operation and it is sufficient to analyze the response of a single object. The total result is the sum of all the individual results we can put them together and we can easily separate them by processing all the raw data pixels. We add everything and nevertheless that all the contributions are in the same elements of the data matrix we are still able to separate them from each other afterwards.

To understand the origin of a complex-valued signal we can imagine that there is a point on the ground, the target, and that is reflecting with a certain strength. From that strength, we are getting the amplitude of the recorded data. Assuming that there is an isotropic reflection of the impulse on the ground i.e. the point may reflect radiation into other directions in space. Every point on the ground individually has the different capability of scattering the signal. Recording the Echo, the amplitude is sigma-naught σ_0 , radar backscatter. The idea that the impulse that is reflected by the ground is isotropically scattering into all the directions in space is not completely true but one can imagine that is done by certain normalized object and that is why we are calling σ_0 the backscatter cross section.

The amplitude corresponds to the power of the backscattering at the particular location on the ground and maybe damped somehow. We still need to get a phase angle in order to generate a complex number. Having that particular amplitude, phase needs to be extracted by looking at the distance of the point from the center. So, the phase is directly related to the real distance between sensor and the object. The radar passes by

the target closest in the distance r_0 , this happens when the platform is perpendicular to the target. Then it continues to fly by a particular distance along the x-direction, the real distance of a target on the ground from the antenna is computed according to the Pythagoras theorem.

$$\varphi(x) = \frac{4\pi}{\lambda} \sqrt{r_0^2 + x^2}$$

Dividing the real distance by wavelength we get number of wavelengths from the antenna to the ground and then multiply by $2(2\pi)$ in order to get an angle. Factor 2 arise from the fact that the signal runs from the internet to the ground and back again.

We are not getting the phase of all the wavelength on the way from the antenna to the ground and back, but we are just recording the phase of the last incomplete wave on the traveling distance of the signal.

The point on the ground may occur when the antennas beam width footprint begins to see the scatterer and here the first echo is recorded. At the end point of the beam widths footprint, the target is seen the last time. At this point the last echo from that particular object is recorded. All these recorded echoes are processed in the focusing operation and we are using all these different recordings to generate the final SAR image.

2.3.3. SAR Processing: Block Diagram

Referring to Figure 10, is a simplified block diagram of a complete SAR processor. There is an analog to digital converter to store and process the data digitally into the onboard memory

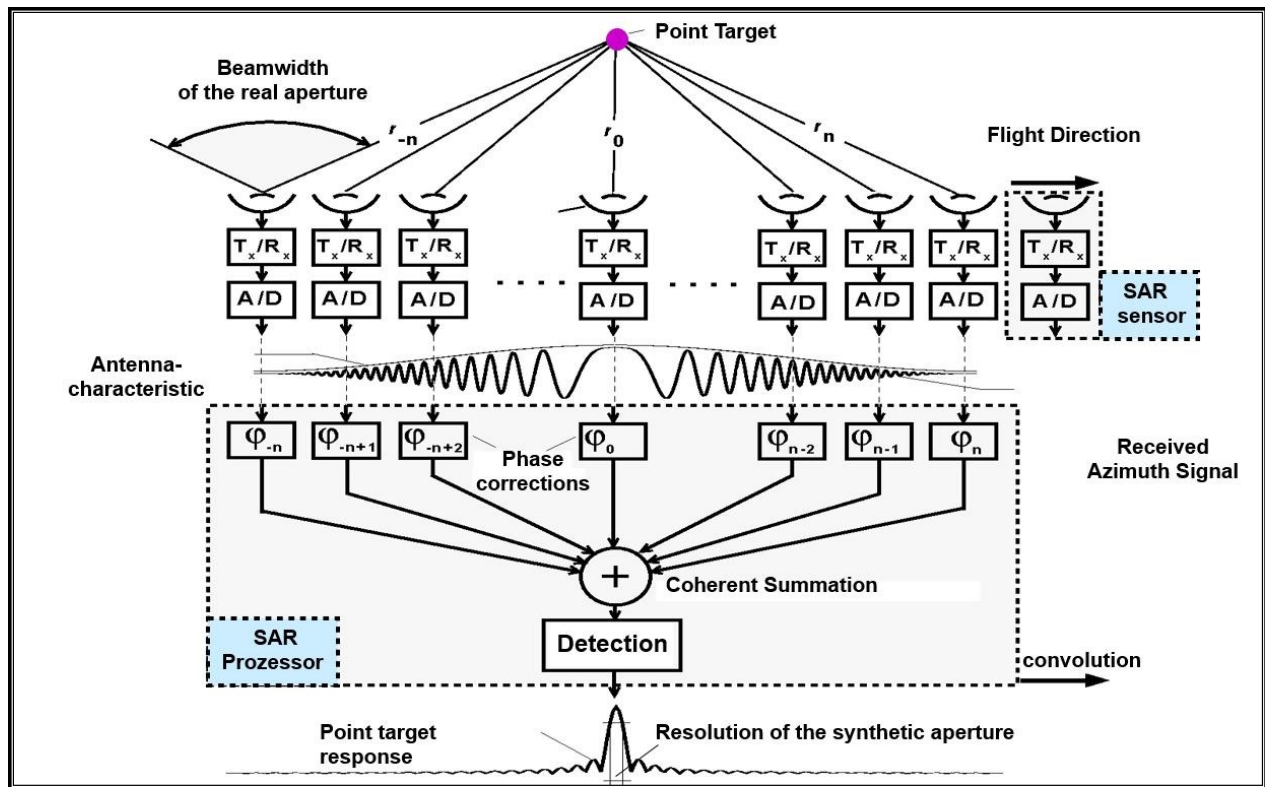


Figure 10 SAR processor coherent summation block diagram

A reference function that apply to these individual recordings, we multiply with the reference function values and then we do the coherent summation, store the result in the output called a single look complex image. If there is a single strongly reflecting point target, then we can detect the location of that point by thresholding the bright point information in the single look complex SAR data, called as the detection step at the end of the processing.

As mentioned before, the sensor approaches the point on the ground, gets as close as possible at the distance r_0 , where it is perpendicular to the point and then it progresses with flight. We can compute all the different ranges for the different impulses that have been emitted.

$$r(t) = \sqrt{r_0^2 + v^2(t - t_0)^2}$$

It is range r_0 squared, added to the speed of the airplane squared, v^2 , times the time difference between the actual time of the impulse 't' and time ' t_0 '. When the sensor is at the position perpendicular to the target location, that time difference is squared. We can also do a Taylor approximation, so we are having the approximate range distance r :

$$r(t) \approx r_o^2 + \frac{v^2(t - t_o)^2}{2r_o}$$

From the distances we can compute the phases. The distance is divided by the wavelength λ , multiplied by two (the signal travels back and forth), multiplied with 2π to get a phase in radians. Phase being positive, or negative is rather a matter of definition.

$$\varphi(t) = -\frac{4\pi}{\lambda} \left(r_o + \frac{v^2(t - t_o)^2}{2r_o} \right)$$

We can compute frequencies from the phases when we derivate a phase ($d\varphi$) with respect to time (dt), we have a phase frequency. We get the frequency after converting angle to wavelength by subdividing by 2π .

$$f(t) = -\frac{1}{2\pi} \cdot \frac{d\varphi}{dt} = -\frac{2v^2}{\lambda r_o} (t - t_o)$$

Inserting the derivative gives us two times velocity squared, divided by wavelength times range.

$$k_a = \frac{2v^2}{\lambda r_o}$$

This is the azimuth chirp rate k_a that is happening due to the Doppler effect the signal experiences because the sensor is flying by the target on the ground.

2.3.4. SAR Processing: Doppler Frequency & Bandwidth

Plotting the phase function having initial time to set to 1 sec and to simulate we assume that the speed of the platform of 70 m/s, the wavelength being used is 5cm, so it is a C-band radar. The distance between the plane from the opening to the ground of 5000 meters we get the phase curve, a parabola.

Frequency modulation, however, is a linear straight line, we first have an increase with respect to the reference frequency and then we have a decrease because we have passed by the object further away. The more we are increasing 'the change of distance' the higher the frequency modulation is. For a certain time, the frequency development is linear. When we record amplitude, we can assume that the amplitude is a rectangular impulse, we can observe the change of the real or imaginary values by plotting the curves. The real parts of signal wave fluctuate more when we are coming by and it stops fluctuating when we are at a perpendicular position to it and when we increase the distance then the wavelengths get shorter.

The frequency that constitutes the Doppler effect frequency modulation was seen in a previous equation. We have a linear dependence on the time which is a written as time

difference vs the point in time when the sensor is closest to a particular target on the ground. This individual target time t_0 , and the time difference t are changing, and frequency is linear to the time difference and hence a straight line (Figure 11). This line is individual for each point on the graph (Figure 11) for each object. For object one we are seeing at a particular time t_0 , one frequency development and object is visible at a time t is having another (shifted) frequency development.

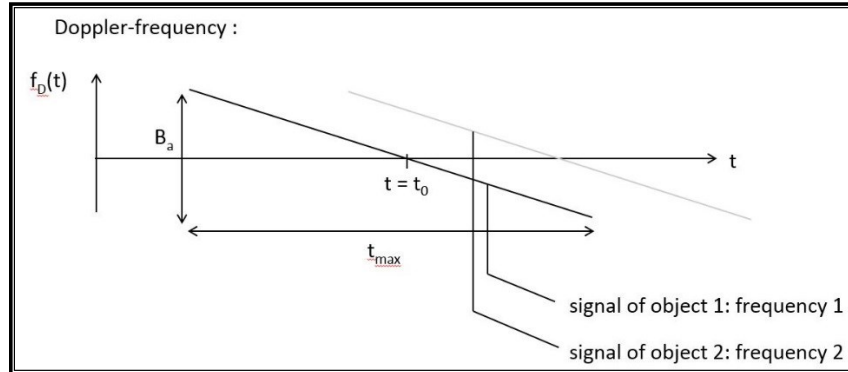


Figure 11 Doppler Frequency

The steepness of the curve is the consequence of factor k_a and are only constants in the expression for every point. The plane flies with the constant speed the wavelength being used is not changing and r_0 is individual to the particular point on the ground. The function f is linear that however is certainly only true for a limited time duration for the time when the point on the ground is inside of the antennas widely open beam in flight direction. Furthermore, for a wider beam width illuminating the scene for a much longer time, then certainly this wouldn't be a linear function, this linear function is only stemming from the Taylor approximation that we have used. It is efficient because we know that our radar is only illuminating a limited angle in space.

Therefore, for this little time difference that we are seeing points on the ground, it is bearable that we use the Taylor approximation.

The duration in which we see the point on the ground is t_{max} and that multiplied was the speed of the plane v is giving us how long is a synthetic aperture is or length of synthetic aperture l_{sa} divided by the speed of the platform is giving us the time at which we see the point on the ground.

$$t_{max} = \frac{L_{sa}}{v}$$

Over this time the impulse is experiencing a Doppler effect which is giving us the bandwidth of the signals frequency modulation and that results from two times the velocity of the airplane subdivided by the mechanical length of the antenna.

$$B_p = f\left(-\frac{t_{max}}{2}\right) - f\left(\frac{t_{max}}{2}\right) = \frac{2v}{L}$$

For the Doppler frequency first, we are looking forwards at $-t_{max}/2$, and observe the frequency. We split the time t_{max} into one half in which we are approaching the point on the ground and then we are getting away from that point for another time period $+t_{max}/2$. The Doppler frequency change is the frequency difference at the point in time when the target was entering the beam and the point when the target was exiting the beam. When we can insert these two expressions we get the required bandwidth. It is two times speed of the platform divided by the length of the synthetic aperture. The total bandwidth of the signal is called the Doppler bandwidth and it corresponds to the maximum variation in frequency modulation within the synthetic aperture.

Shorter the antenna is the larger doppler bandwidth since we have a wider beam width and also certainly higher relative velocities occur when we are seeing the targets in the wider beam. The Doppler bandwidth is an important parameter with respect to the choice of a suitable PRF.

PRF needs to be high when the Doppler bandwidth is large. The PRF is a frequency with which radar pulses are emitted and received. It is controlling the distance between two emitted pulses, time distance of light distance. If PRF is smaller than the Doppler bandwidth than the received signal cannot be recorded correctly because we are not fulfilling the Nyquist sampling theorem. This theorem says that for a continuous signal with the maximum frequency of f_{max} must be sampled with at least a frequency of $2 \times f_{max}$. For every wave we are having two samples, we need at least two supporting measurements otherwise we cannot infer that wave characteristics. Then, however, we can reconstruct the discrete digital signal without any loss of information. So, the Doppler bandwidth asks for a particular PRF and if we make sure that the Doppler bandwidth is high, which is generally something would like to have, then we need to have a high PRF. This may be complicated as we otherwise want to have our antenna recording long echoes to cover a wide swath.

2.3.5. SAR Processing: Matched Filtering (Illustrative)

Now we see how the data that is summed in the same pixels of the raw data set can be separated for each location individually with the help of SAR focusing operation. For example, we have two points on the ground that contribute to the signal we want to see the echo contributions of these two points. For each of the points, we are recording a certain phase information, there is also an amplitude but that is individual to each point and we cannot change it because it is depending on what is located on the surface of the Earth.

What it is a more under control are the phases and they are depending on the distances that occur in between the sensor and the ground. Pythagoras theorem is used to

compute the distance of the antenna at a position x from the ground. We are having the phase φ of a position x along the flight path that is computed according to the previously mentioned formula. Applying Taylor approximation and then we get:

$$\Phi(x) = \frac{4\pi}{\lambda} \sqrt{(x^2 + r_o^2)} + \Phi_{obj} \approx \frac{4\pi}{\lambda} \frac{x^2}{2r} + const$$

showing us that the phase history is following a parabola. The phase is developed according to that parabola and for another point in the same distance of closest approach to the sensor, we are having the second parabola. However, that is happening at a different position of the closest approach of the first point. After that, we are summing all the different complex numbers in the raw data signals we've seen it in the simplistic simulation example before (Figure 12).

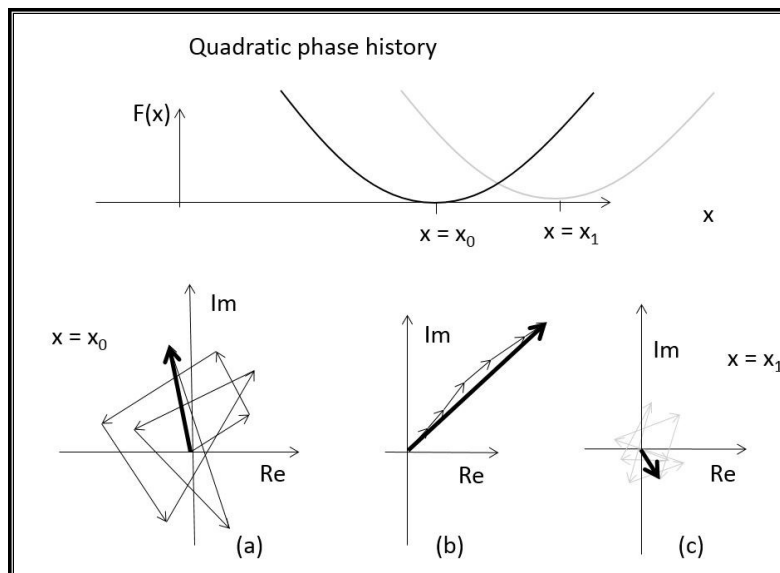


Figure 12 Phase history of a scatterer: coherent (b) and non-coherent (c) summation

Then convolution is conducted with the reference function which is a multiplication with a filter kernel function that follows the theoretical signal of a single point in empty space. The convolution operation is making sure that the phase history is taken into account and we are summing the echoes of all the points on the ground coherently in the raw data matrix. Influence of a particular point is happening over the length of the synthetic aperture. That is repeated for every possible offset between the raw signal and the filter kernel. Afterward, the focusing operation which is the SAR processing operation is a deconvolution with a filter kernel.

As seen before phase history has a parabolic nature (Figure 12, top), a second-degree polynomial. Its lowest point is happening at the distance of closest approach. For the phase of each individual data sample in the raw data we must subtract all the contributions of the full wavelength. We can imagine the phase to be a pointer in a circle

(fig 13 top) and the phase angle are the arrows direction in the clockwise display. For each impulse, we have a different phase angle now all the contributions are having individual angles. These angles are resulting from the individual distance of the point onto the ground from the sensor that was flying at a particular position at x . The clock hands pointing to the different directions corresponding to the phases when we are approaching the point on the ground than the clock hand rotates fast and then it rotates slower. The curve is not steep anymore when we are close and is absolutely horizontal when we are at closest approach to the point on the ground. At this point, the clock hand stands still and then it starts rotating faster from one impulse to the other again as the curve is getting steeper also seen in the parabola.

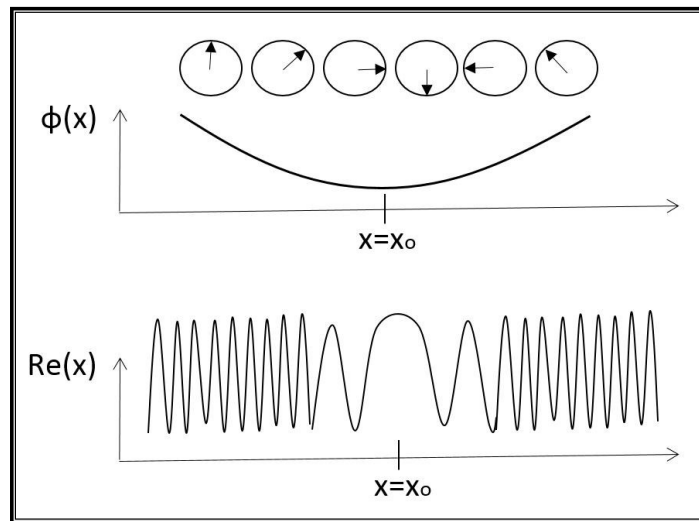


Figure 13 Phase and amplitude illustrated

When we want to see that different phase change speed along the flight we can also plot the real component of the complex signal consisting of amplitude and phase (fig 13 bottom). We see the wave having a short length when the point is coming into the beam first then the wave is getting longer lengths and finally doesn't even have the appearance of a wave anymore when we are the closest approach and then it is getting shorter wavelength again when we are flying away from the point on the ground. This is the data that each point contributes to the raw data matrix and each points contribution in the raw data matrix are sitting in different pixels according to the location of the point inside of the image. The same contribution occurs for each individual point however they are distributed differently in the raw data matrix.

Now we do a convolution operation with the reference function, the convolution operation is repeating that same phase history, we are turning each clock hands arrow with the individual knowledge of its location in the data matrix in the same direction for one particular point. All the other contributions are summed into the raw data matrix

are treated in a way such that the reference function does not contain the individual points responses phase angles correctly and therefore only the individual points that are located at the particular position x_0 is getting its contributions adjusted into the same direction. These contributions are summed 'coherently' so we see it very bright in the resulting curve and all the other points contributions in the data matrix are 'suppressed' as they are pointing into random directions and they are not summed coherently.

With the matched filtering we are making sure that only the local contributions of that particular location they are summed coherently. For two points (x_0 and x_1 , Figure 13) contributions in the raw data matrix when the matched filtering operation is adapted to the position x_0 then we are turning all the contributions of this point along the flight direction into the same angle in the complex data matrix of the processing output. While the points that do not refer to that particular location, for instance of the contribution of a point with position x_1 this points contribution are randomly summed and are therefore getting a very small output at this particular location. The single point is dominating so we can separate x_0 point contribution from x_1 point contribution clearly. The points contributions that match the position of the reference function at this point of the matched filtering operation gets coherence summation while the other point gets incoherent summation where a random sum occurs that is not influencing the final output.

Later, when the reference function has been shifted from the location x_0 to the location x_1 then we are summing more contributions of the point at location x_1 coherently which means they are getting summed into a consistent direction in the complex number plane while all other contributions are summed wrongly or incoherently.

2.3.6. SAR Processing: Frequency Domain

To summarize, we are having a raw data set, we read the raw data matrix compare containing complex values then line by line then we convolve the data with the reference function. Once a convolution in one line has been done we have to adapt the range and the reference function to the late larger range of the next azimuth line and then we do that convolution. Its due to the fact that in near range the beam of the radar antennas only covering a small part and in far it is covering a wider distance, this needs to be considered when the raw data is compressed by the focusing in azimuth. Row by row we are changing the reference function. Each time the convolution in one row is conducted, we save the image matrix and the output is the called single look of complex image data.

Not only the SAR focusing is done but prior to that also in the range direction a matched filtering has to be conducted. There we are using the reference function stemming from the Frequency modulation of the original SAR impulse and after range compression, we

have range compressed data and that is then further processed by the SAR matched filtering. For doing the data processing accordingly we have to take into account that often the processing is not done in a spatial domain but in the frequency domain.

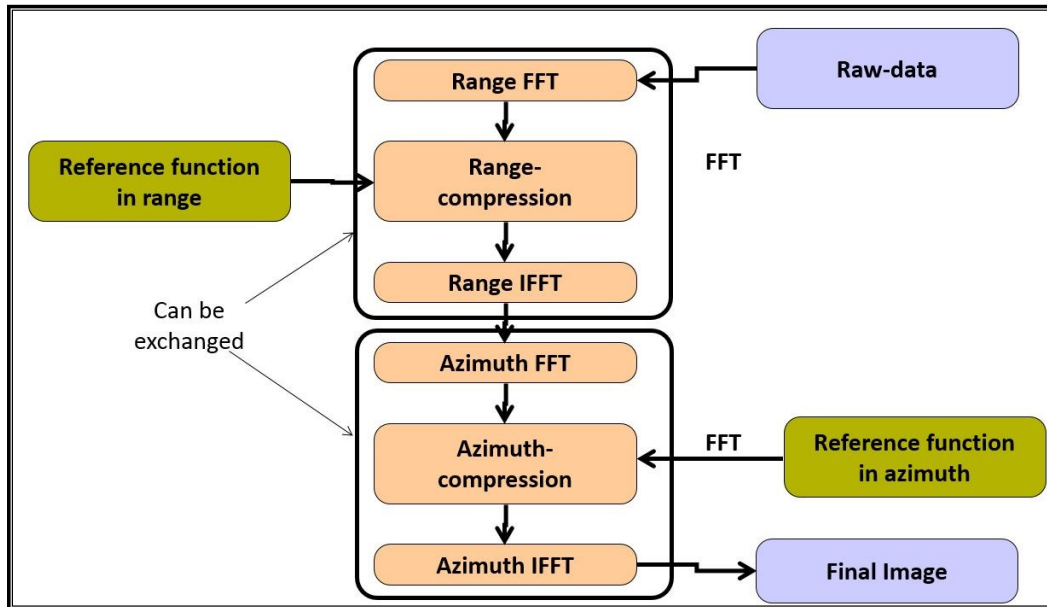


Figure 14 Flow chart SAR processing (frequency domain)

The raw data is first transformed by a fast Fourier transform in range direction then we do range compression by a multiplication operation in the frequency domain. Then inverse fast Fourier transform in order to get the data back in the spatial domain. After that the same thing is conducted in the azimuth direction so we do an azimuth fast Fourier transform, do azimuth compression by multiplication in the frequency domain not doing a convolution in the spatial domain and the result is inversely Fast Fourier transformed back into spatial domain and we get the single look complex image.

2.3.7. SAR Processing: Point Target Response

Once we consider what happens with respect to two points on the ground than we have to note that originally the two points on the ground are having its contributions to the raw data in a large subsection of the raw data matrix. For the two points (fig. 15), the ground is scanned by the antenna lobe which is widely opened moreover we are having raw data with frequency modulated impulses having a long duration in time, so the reflections of a single point are arriving in a considerably large part of the raw data matrix. The second point that is to be recorded in a different part of the raw data matrix, but these two points already overlap by contributing to these pixels where the two rectangles overlap together (Figure 15, top).

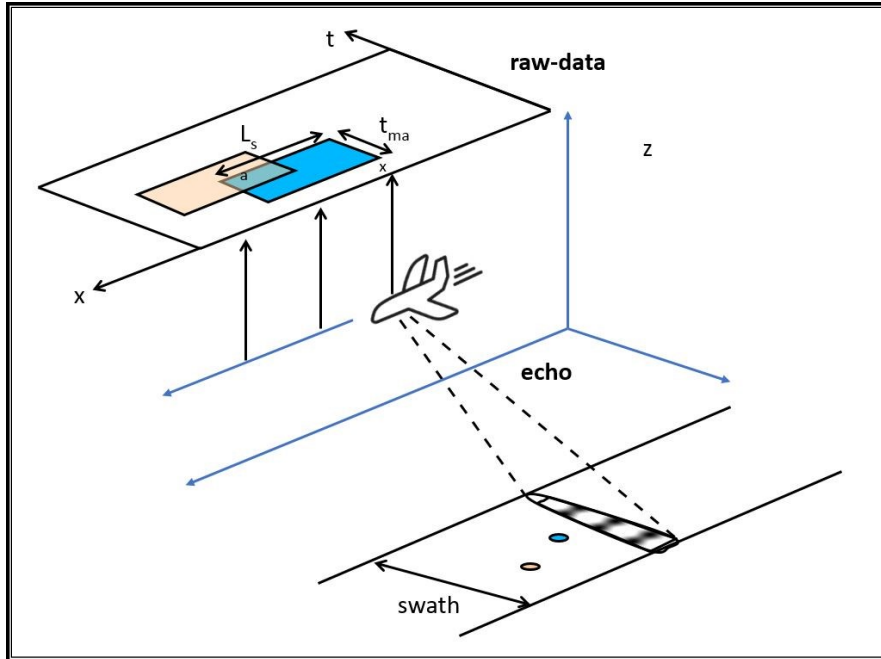


Figure 15 Two scatters visualized in raw data matrix

After the range compression and the azimuth compression (a convolution in range and azimuth) processing, the contributions of the two points are not distributed over larger parts in the image any longer, but we have focused their contributions to a couple of pixels that correspond to the exact locations of the points. For a three-dimensional zoom into the single look complex data than for a single point, the matrix would look like a two dimensional $\text{sinc}(x)/x$ function (Figure 16, right). Now we have achieved a spatial resolution in range direction and spatial resolution in azimuth direction that is quite high compared to the original low resolution where the points are actually blurred over a large part of the raw data matrix.

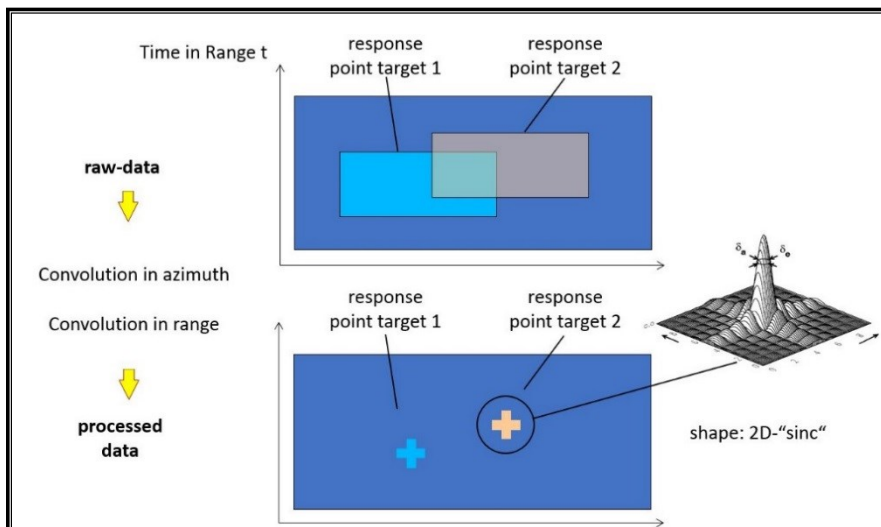


Figure 16 Point target after compression in SLC image

2.3.8. SAR Processing: Range Cell Migration (RCM) and Correction

We did not yet consider what actually happens to the position in which the contributions of the single points are stored in the raw data matrix. Once we are flying the antenna past certain point target on the ground that the distances of the point changes. When the plane is approaching, distances are large, we are passing by the point somewhere on the side in a slanted viewing direction, up to a certain point where the airplane is at the point of closest approach, and then distances are getting larger again. These distances are certainly also realized when you consider the places in which the information is stored in the raw data matrix. The contributions of the single point target on the ground are actually not located in an absolutely rectangular region but it is following a 'curve' according to the change of the distance. Before approaching the point, distance is larger which gets smaller until the closest point of approach and then increases again as we move away. This curve is approximately a parabola (Figure 17, top), so all the contributions of the point target are distributed on that parabola. The range cell of the point target in the raw data matrix migrates and that RCM we must consider when we do the SAR focusing operation.

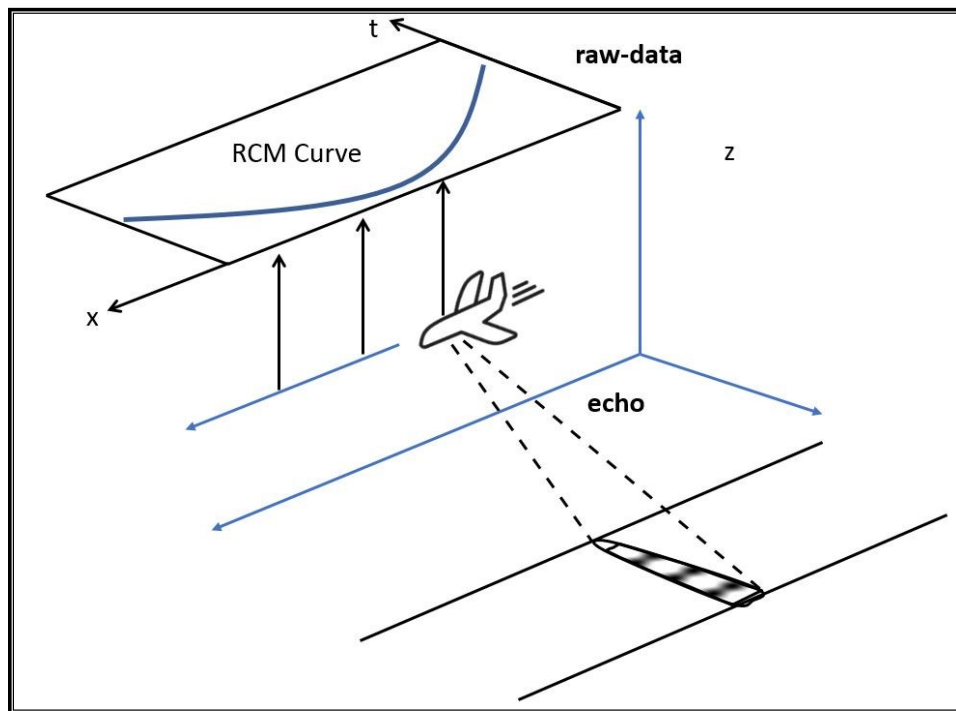


Figure 17 Range cell migration curve

The echo time defines the column in the raw data where an echo is stored. This time is longer when we are further away from the point and shorter when we are closer by. The time when an echo of the target is received varies with the azimuth position (the position along the flight path) and point target response shows a curvature called RCM Curve.

In a simulated example (Figure 18, left) raw data received from a single strong target in the middle of the image and responses are shown where all the contributions are on parabola curves in the raw data matrix. Then we do a range compression done in the same way for each of the columns in the raw data matrix and we are focusing the information of that strong scatterer in the middle on that RCM curve.

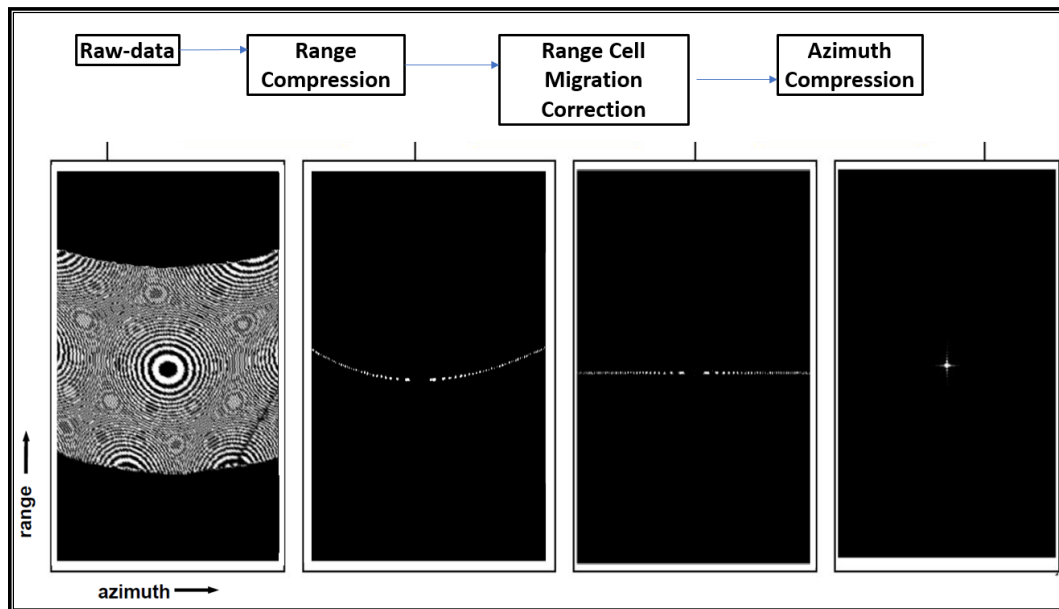


Figure 18 SAR simulated example

Now we have to process the data in order to correct for RCM so that we get a data matrix where the information of the single point is not on the parabola anymore but located on a straight line. After that, we can do an FFT and do the operation in the frequency domain which focuses all the information in the *sinc* of this particular point.

It is certainly not only happening for one single point in a simulation but for every point in the image independent of whether it has a strong amplitude or not whether it is bright or a dark point in the image. However, for the bright points, we can see the effects more easily. For a real scenario, after the range focusing, we may see a lot of parabolas in the image. Then we do, however complicated in operation it maybe, a RCM correction and that corrected data is then azimuth focused resulting in a single look complex image.

2.3.9. SAR Processing: Speckle Effect

A large fluctuation of the amplitudes is due to the 'Speckle Effect'. We use coherent radiation so all the waves, after the impulse generation, have the known phase and are propagating through the atmosphere until they are reflected on the ground. On the ground, we have to take into account that a pixel size is much larger than one wavelength. The resolution or the pixel size may, for instance, be 1m while we are using

a radar radiation in C-Band and having a wavelength of 5 cm. All the coherent radiation hits the ground in that resolution cell on two different items located on the Earth which are reflecting the impulse. The different items are not only distributed over that one square meter of the resolution cell but may have a volumetric structure like a tree on the with the stem, twigs, leaves of trees and so on, which altogether reflect a little part of the radar signal. The reflection happens at a particular position of the object. When the Echo is reflected back to the radio antenna the originally coherent radiation is not really coherent anymore, because little contributions from the different items in the resolution cell on the square meter they are on their way according to the phase position it has at the time and at the position of reflection.

When the summation is conducted of all the little contributions at the receiving antenna then there is a 'random summation' of contributions in the complex number plane and we are having overlap of wave peaks with wave peaks and also with wave valleys, sometimes it may happen that waves peaks strengthen each other and we have a bright spot and on other pixels we have accidental elimination of wave peaks and wave valleys and there is darkness in the image. Even for homogeneous surfaces like the meadow or field, we are having both very bright and very dark pixels. It is due to random superimposition of the tiny contributions of the different items that are located in the different pixel's surfaces on the ground.

This speckle is something we do not like in the image as the SAR image looks quite blurry. To eliminate the problem, we do not have a lot of options that maintain the original images resolution. We can only average neighboring pixels. There is a lot of effort in the averaging operation to eliminate the speckle effect and get a clear visual representation of the items that are located on the surface of the Earth.

Many speckle filtering operations try to make sure that the averaging is only conducted inside of homogeneous services on the ground and not across the boundary between two different homogeneous services.

So, we are averaging the pixels inside of a field or inside of a street, but we do not want to average the field pixels with the street pixels. That is the task of 'multi-look processing' we are averaging several looks to the same or a similar place on the ground. It is because of the speckle effect that homogeneous areas appear grainy and blurred but the pointwise objects, however, are not affected and are imaged quite well as they have a strong contribution and consists of an object that is spatially limited with very small a place inside of the resolution cell. Such point wise objects, such as reflectors are often used in order to provide control points in the SAR data may be imaged quite right and are not blurry.

We would like to average all the pixels that are suffering from the speckle effects that are getting its signal from many items scattered over the resolution cell and we do not

want to blur those locations where the echo is actually not stemming from the full resolution cell but rather more from a single location in the resolution cell.

For a place where the wall of the building touches the ground is not something that is spatially very widely distributed but it is at a particular location and that generates a double bounce effect that is very bright in the image. It is therefore not suffering from the speckle, we do not have the accidental summation of echo here in the resolution cell but the wall with respect to the wavelength of the radar is located very stable at a particular location.

Image analysis of such a speckled image can be very complicated and we would like to have an image that suffers less from the speckle effect. To reduce this effect, we do multi-look processing that results in an improved radiometric resolution while the spatial resolution is reduced to some extent as we are doing some averaging.

2.3.10. SAR Processing: Multibook Processing

In multilook processing, we are actually doing the radar image several times. We have already said the general idea of the SAR is to use a radar beam that is widely open and covering a larger distance on the ground and then we are analyzing all the impulses that are looking at the same location on the ground together and use all these many impulses in order to build the synthetic antenna. Then we get a very narrow radar beam an artificial beam giving us a high-resolution image.

This principle can be compromised in a way to get an image that suffers less from the speckle effect. We generate the image several times by subdividing the long synthetic antenna into three equally long parts such that we are generating one image while the radar antenna is looking forwards, second image that is generated from the impulses that look at a specific point target in a side looking direction and third image is generated where the radar is looking a little bit backwards. We are using first one-third of the impulses in order to do the azimuth compression the first time, the next one-third of impulses are used for a second image and last one-third used to process the third image.

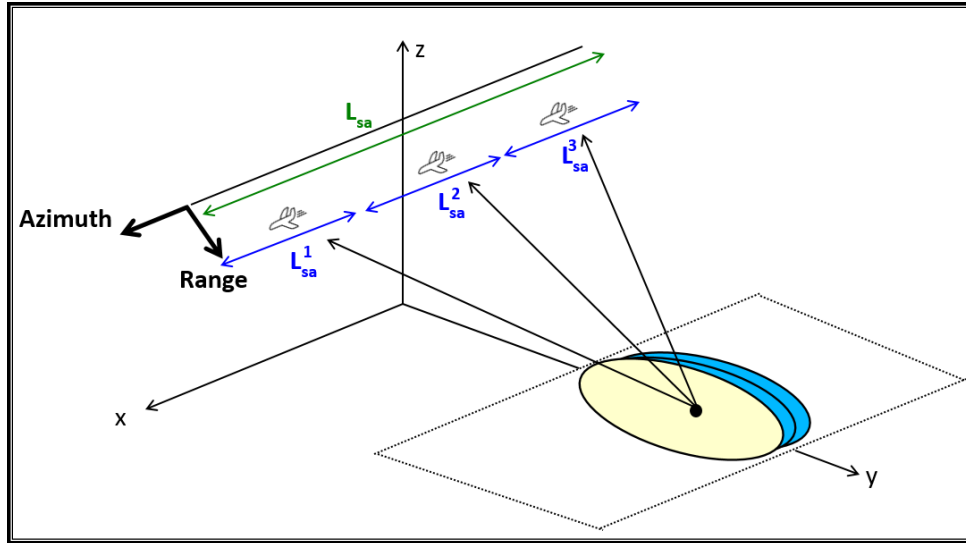


Figure 19 Multibook Processing

The Doppler frequency is correlated with the look angle. Using the idea of the synthetic antenna creatively and processing different subparts of the synthetic aperture, the azimuth spectrum can be split into several statistically independent pieces. Each piece delivers an independent complex single look SAR image. Multi look means we are having a first look, a second look and a third look for the different thirds of the possible synthetic antenna, doing much shorter antennas several times. The resulting three images they can be averaged. When we are averaging them we only do that with the amplitude information in the single look complex images and that is called 'in-coherent averaging'. Such a method can also be applied in the range direction by subdividing the frequency modulated range impulses into several pieces.

We see (Figure 20, left) a one look processed image created using the maximum length of the synthetic aperture and we see quite good spatial resolution, but the image looks speckled. For the other image (Figure 20, right) we are having a nine-look image. In range and in azimuth direction we split the possible aperture it into three parts each, and that allows us to average nine-looks. The pixel size is three times as large as in the single look part and the advantage is that the speckle effect is not as present anymore and image looks much smoother. The disadvantage, however, is that we do not have the same high spatial resolution anymore. Multi-look images are usually processed in addition to the single complex image with the highest possible resolution. Having the single look complex data, the averaging can be done possibly in any way preferable considering different kinds of speckle filtering.

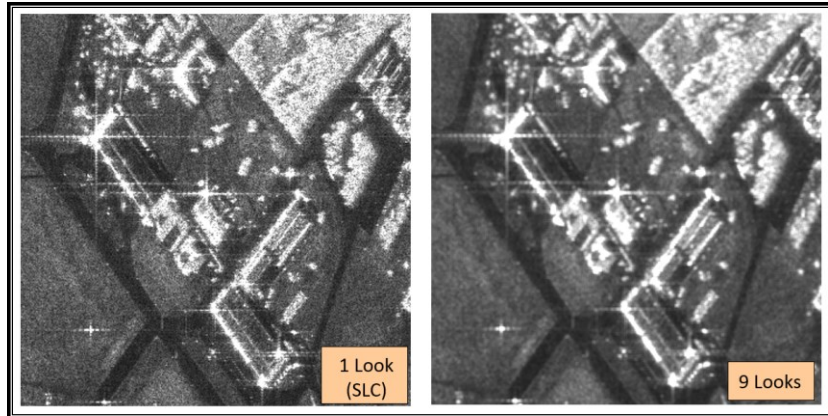


Figure 20 One look vs nine looks

Multi-look images better suited for amplitude analysis, having more justified amplitudes where we are not having the random fluctuation of the brightness the same degree as in the original single look image.

2.4. Special Imaging Mode: ScanSAR, Spotlight

There are special imaging modes of SAR antennas of that are operated on the satellites. A scansar processing is possible where the beam of the radar is steered to different swathes on the ground, just in order to cover a wider swath on the expense of a reduced range resolution.

This steering of viewing direction of SAR antenna in the scansar mode is eliminating the problems where switching is required for transmit and receive mode. In this mode we are still be able to maintain a certain PRF to get sampling rate enough to cover certain swath on the ground.

With the scheme of switching the antenna to look two different swathes allows us to record low-resolution images in a smart manner and cover a large swath on the ground typically 500km wide.

The wide swath of the scansar mode is subdivided into several swathes while electronic control of the viewing direction of the antenna takes care of acquisitions on different parts on the ground. As a user of the images, we may not notice it because the providers of the SAR data take care of a good processing of the data such that we do not see any problem with the different sub swathes getting close to each other.

It is also possible to increase the resolution even further by making the change in viewing direction on the ground for a larger time than what usually is in a normal mode. This is done by electronically looking forwards to a particular region of focus on the ground and then steering the antenna slowly such that we are looking perpendicular to the flight direction and later on looking backward. Then we have an artificially super

wide beam and that can also be subject to much more complicated SAR focusing operation. We get a synthetic length on an antenna that may reach upto 2300 km. For example, when we are having a satellite in sun-synchronous mode, it may fly 650 km high and the point under the track may be 650 km away from the area that is being imaged, and we may then consider start looking to that point 650km prior to the closest point and continue to record with a steered antenna 650 km passed that point than we are actually able to generate an improved spatial resolution in the range of a 'decimeter' even for SAR images acquired from satellites. Then, however, we are imaging a single area and not a strip where we are concentrating the attention to a particular region and ignoring everything that is before and after and in the vicinity. We are basically flying by the area of interest and use all the impulses that are send over this 1300 km in order to record the responses from our area of interest which may be quite small like 100m. The advantage is that then we get locally an extremely high resolution. Such a mode is termed as spotlight mode.

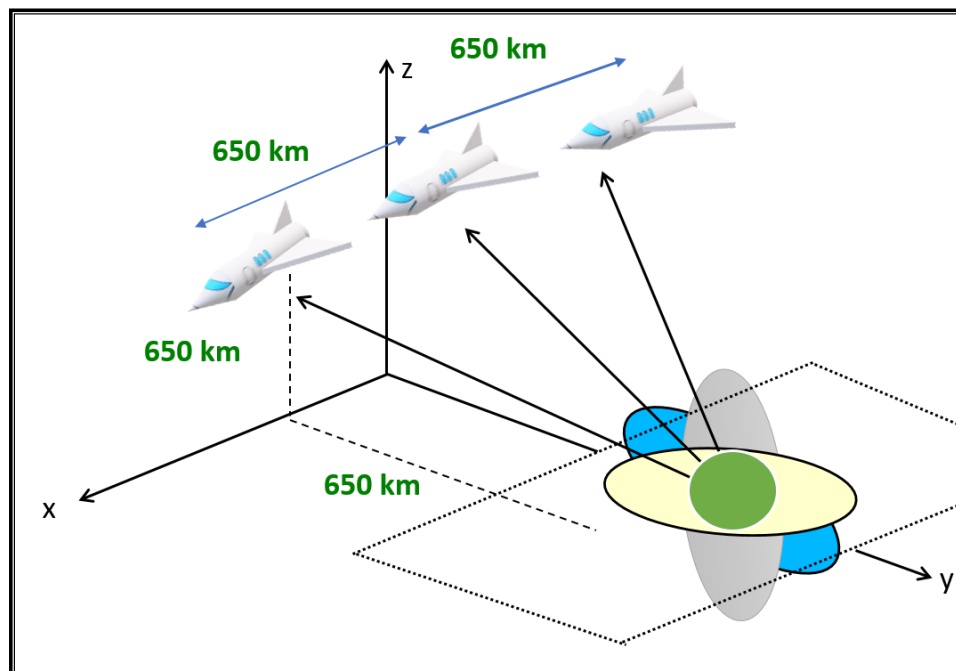


Figure 21 Spotlight mode in SAR processing

Is the standard strip map image (E-SAR) we get a pixel size of 3m in azimuth direction and in the spotlight mode the pixel size is reduced to 46 cm. We have a lot more detail in the spotlight image than in the classical strip map SAR image. The processing is quite complicated in order to come from the raw data to the high-resolution image. The best thing would be to do everything in the time domain and be very adaptive to the individual range cell Migration for instance but that is certainly is complicated due to the many correlation or convolution operations in the time domain. We prefer to do some processing in the Frequency domain and replace the contributions by

multiplication however we still have to take care of the RCM by applying similar RCM correction to a location that is located close to each other. Finally, very special SAR modes require a very particular processing schemes that are adapted to the special characteristics of the underlying radar signals we've just seen these scansar and the spotlight mode. More details can be found for in the book 'Digital processing of SAR data' (Cumming and Wong, 2005).

Chapter 3: Localizing TerraSAR-X images using Double Corner Reflectors

This chapter elaborates on the localization accuracy of SAR images. At the beginning, some basic properties and configurations for TSX are reviewed, including the available TSX image products and their accuracies. Later on, a novel method is used for the localization of double corner reflectors, where the aim is to transfer the high precision of TSX orbits to localize selected points on the ground. Simulation with radar cross section (RCS) calculations of the designed reflectors is performed. Construction and mounting of reflectors are discussed in detail with the TSX image acquisition. Lastly, the image localization is performed using orbital interpolation where the sources of errors and their corrections are done.

3.1. TerraSAR-X's Orbital Accuracy and Keynotes

TerraSAR-X (TSX) was launched on 15 June 2007 and has been in operational service since January 2008. It is an imaging radar satellite, for the continuous observation of earth's surface. This satellite is developed under a partnership between the German Space Center (DLR) and European Aeronautic Defense and Space Company (EADS) Astrium. The commercial rights are held by this geo-information service provider Astrium.

The payload of this satellite is a SAR antenna as a phased array operating at X-band frequency of 9.6 GHz and wavelength of 3.1 cm. At an altitude of 514 km the satellite orbits in a polar orbit acquiring radar images for the earth. The orbit for TSX is a sun-synchronous orbit where the solar panels are always facing the sun for optimum energy. The lifetime of this satellite was planned for five years but after eleven years, it is still completely operable and providing high-resolution radar images, irrespective of weather conditions and sun illumination. The key orbital parameters and launch information is listed in Table 1 and

Table 2 respectively.

Table 1 Summarizing the orbital parameters of the TSX satellite

Orbital parameters	
Reference system	Geocentric
Orbital Height	Low Earth
Semi-major axis	6,886.39 km (4,279.00 mi)
Eccentricity	0.0001445
Perigee	514 km (319 mi)
Apogee	516 km (321 mi)
Inclination	97.44 degrees
Period	94.79 minutes
Epoch	25 January 2015, 02:35:23 UTC

Table 2 Launch site, date and other spacecraft properties for TSX

Spacecraft properties and Mission	
Manufacturer	EADS Astrium
Launch mass	1,230 kg (2,710 lb)
Launch date	15 June 2007, 02:14 UTC
Rocket	Dnepr
Launch site	Baikonur 109/95

3.1.1. The TSX Multimode SAR Processor (TMSP)

At the ground segment data processing is done by the TSX multimode processor known as TMSP (Roth, Huber and Kosmann, 2004). With the multimode capability, the same processor is used for processing all types of receiving modes including strip map, scan sar, and spotlight. The processing is performed in two stages where the data is screened in the first stage and then level 1b processing is performed according to the user's request. In the screening process after the data reception, the data is analyzed for quality. Then the parameters for chirp replica, doppler centroid etc. are estimated. Quick look images for all the received data are generated at this stage.

The processing in the second stage is dependent on the user request where the scene detail and type of product is specified before the processing starts. Phase preserved single look slant range complex data is continuously generated at this level by the processor. The focused image pixels are annotated with range delay time ' τ ' and zero doppler time ' t '. To overview, the detailed TMSP level 0 and level 1b processing are shown in the Figure 22 and Figure 23 respectively.

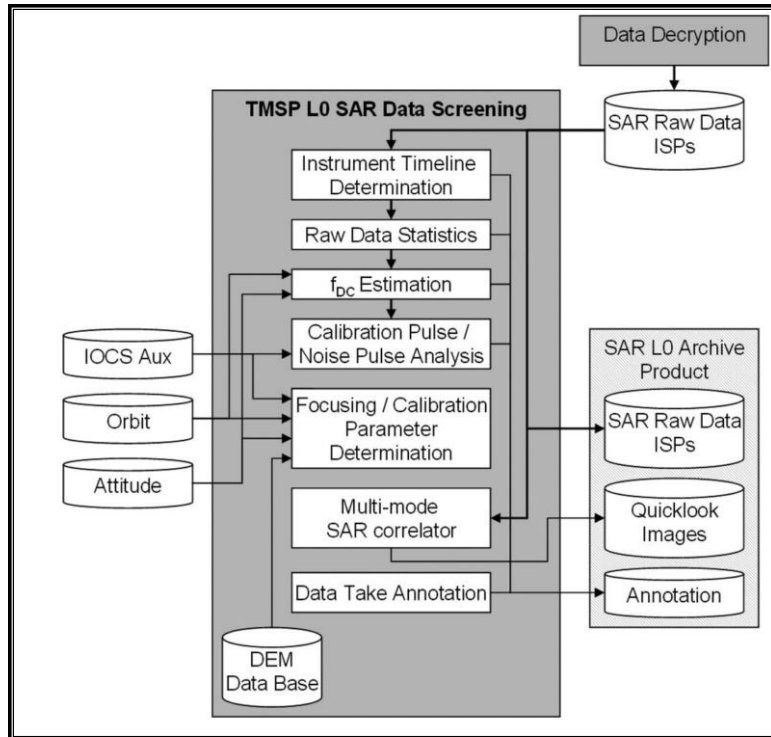


Figure 22 Overview TMSP Level-0 SAR Data screening process (Breit et al., 2010)

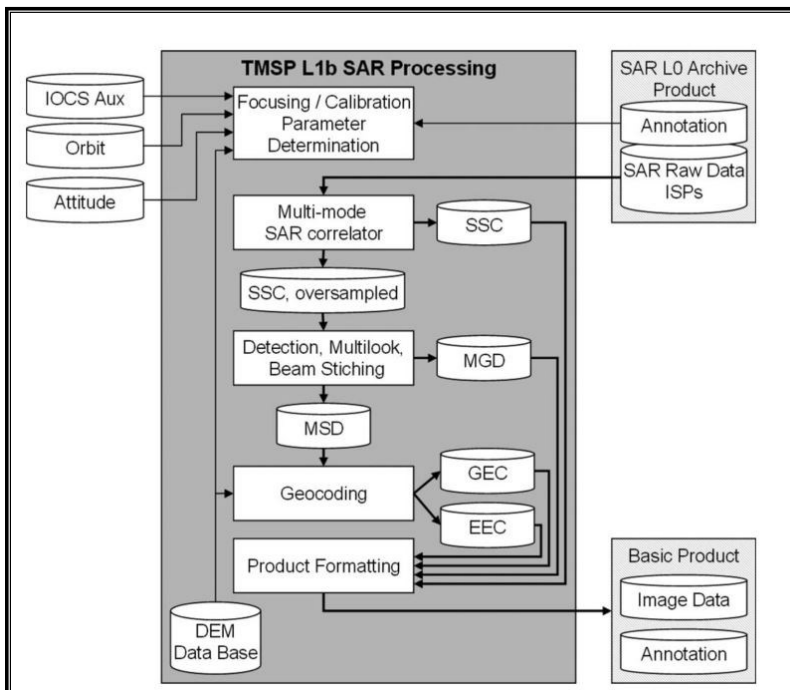


Figure 23 Overview TMSP Level 1 SAR data process (Breit et al., 2010)

3.1.2. Level 1b Products and Annotations

The basic TSX processing modes (data acquisition modes) include Stripmap mode (SM) Scansar mode (SC) Spotlight mode (SL) and high-resolution spotlight (HS) all modes except scansar are available in single and double polarizations.

After the acquisitions several products are available to users including single look slant range complex (SSC), multilook ground range detected (MGD), geocoded ellipsoid corrected (GEC) and enhanced ellipsoid corrected (EEC).

In SSC, complex data is obtained in the single look slant range complex image. The coordinate axes are zero doppler time and range delay time.

MGD is a projection of range delay time axis onto the elevated ellipsoid and the azimuth axis is also linearly scaled from the scene center till the corners of the image.

In GEC, the product is available in the Universal Transverse Mercator (UTM) coordinates where ellipsoidal corrections are made but the terrain corrections are not incorporated. An average scene height is added to the ellipsoidal correction and WGS-84 ellipsoid is used for the correction.

In EEC, the terrain corrections are also applied. The fact that the digital elevation models (DEM's), used for geocoding are much lower in resolution compared to the TSX data, a geocoded terrain model is not processed by the TMSP processor.

The TMSP is also capable of processing different polarization modes where dual and quad mode polarizations are achieved by pulse by pulse toggling.

The range resolution, as mentioned before is solely dependent on the bandwidth of the chirp signal. This resolution is 0.6m for the highest used bandwidth for TSX. For different acquisition modes, the azimuth resolution is summarized in Table 3.

Table 3 Azimuth resolution for TSX in different modes

	HS (m)	SL (m)	SM (m)	SC (m)
Single Polarization	1.1	1.7	3.3	18.5
Double Polarization	2.2	3.4	6.6	-

3.1.3. Corrections and Geometric Accuracy

After the calibration phase of TSX, the pixel localization accuracy was enhanced from 2 m to 1 m level. Where the possible error sources at this level are due to variations in range delay, and other orbital errors are due to variations in the solar activity. A geometric precision is expected because of the highly accurate TSX's orbit. Moreover,

the internal instrument delays and the calibrations for send receive timings are also very precise. To achieve this geometric accuracy, the phase center of TSX antenna is to be localized precisely in space. The location correction of azimuth (transmit and receive location) and other SAR corrections also need to be performed within the processor.

There are two possible orbits (orbital information) to process the SAR data: The science orbit with 3-d orbital accuracy of 20 cm and rapid orbit with a 3-d accuracy within 2 meters. The science orbit is available for processing within five days where as rapid orbit can be used within hours of data acquisition.

The annotated products, available with the ordered products, contain orbit state vectors in the earth-fixed coordinates system. A Chebyshev approximation of degree seven is recommended for interpolation within the given spacing of 10 seconds. Altitude readings every second are also available which are used during the processing to shift the geometric center of SAR antenna, hence the processor can locate the antenna center with the required accuracy.

3.1.4. Azimuthal Localization

Firstly, to localize a pixel within the SAR image, it is required to find the reference azimuth time. The raw data is focused to the zero doppler location within the TMSP processor. This means that the azimuthal plane is 'exactly perpendicular' to the orbital direction, which is the direction for the zero doppler. It is important to note here that the annotated azimuth pixel time is not the time when the radar signal comes in contact with the earth's surface. The assumption that the platform is stationary during the transmission and reception of pulses, also known as 'stop and go' approximation does not take into account the time required for the pulse to travel to the ground and the distance traveled by the platform between transmission and reception of echoes. This correction is performed inside the TMSP processor in the range time during the azimuth focusing. This correction is applied in the frequency domain as a linear phase offset and compensates for the distance covered by the platform during the transmit and receive time duration. If uncorrected, may account for error in the accuracy of meter range.

Another correction for the azimuth time to be accounted for is the instrument tagging time delay. This shift of -0.18 ms needs to be incorporated for the calculation of coordinates. It is approximately 1.27 m on the ground (Fritz, Breit and Eineder, 2008).

3.1.5. Range Localization

The time from the SAR antenna phase center to the pixel's area on ground is the measured fast time or range time for a focused pixel. The annotated range time gives the two-way radar pulse traveling time, they are corrected for known internal instrumental delays but are not corrected for atmospheric influences (Fritz, Breit and

Eineder, 2008). This instrument delay which introduces an error of around 32m in the range direction if not accounted for. This instrumental contribution is well calibrated.

The fact that the pulses pass through a dispersive medium which is the ionosphere and a nondispersive medium which is the troposphere, where the speed of the electromagnetic radiation is less than that in the vacuum, causes the range distances to be overestimated. The ionospheric delay depends on the total electron count (TEC), which is frequency dependent, and on the refractive constant (K).

$$\Delta R_{iono} = \frac{K \cdot TEC}{f^2 \cdot \cos(i)}$$

This ionospheric delay (ΔR) at the TSX frequency ($f = 9.65$ GHz), and the current angle of incidence ($i=30^\circ$) leads to a delay of 2.4 cm. It is compensated for by a constant average TEC of 5 (TEC-units, $10^{16} \text{ el}/\text{m}^2$) for the complete image scene and the refractive constant K of $40.3 \text{ m}^3/\text{s}^2$. The delay caused by the troposphere, on the other hand, is significant and greater in magnitude compared to the ionospheric delay. It depends upon the water vapor content and the angle of incidence and is discussed in detail by (Jehle *et al.*, 2008)

The TMSP uses a simple atmospheric model with a constant path delay of 2.3m in the reference direction. This is equivalent to 1.6m in the near range and 4m in the far range.

3.2. Double Corner Reflector (DCR)

3.2.1. Use of Corner Reflectors in Remote Sensing

RCS is the measure of a target's ability to reflect incident radar signals back to the radar receiver. In other words, it is a measure of the ratio of backscatter power per 'unit solid angle' in the direction of the radar to the power density that is intercepted by the target.

Artificial corner reflectors (CR's) are commonly used for calibration and quality measurements of SAR systems (Gray *et al.*, 1990), (Van Zyl, 1990). Usually, three identical metal plates which are connected at right angles to each other form a triangular corner reflector. Because each plate is perpendicular to the other two, the incident wave falling upon the reflector returns to SAR sensor in the same direction. The distance between sensor and imaged pixel is precisely measured by the time delay of the received signal. The sources of errors are determined by measuring additional time delay while positioning the CR at a known distance and recording the returns with the known sampling frequency. This delay is considered in the calibration of SAR systems. Moreover, other sources of error can also be accounted for. The sharp response of a CR can be localized with higher accuracy than a blurred object. The reflecting area and the geometric phase center of a CR can be determined accurately on the order of millimeters. Exploiting these characteristics, CR's are deployed at various ground

locations to act as reference points for monitoring the displacement of earth surface, landslides and engineered structures such as roads, dams, buildings etc. Particularly, trihedral design of corner reflectors offering high RCS and insensitive to misalignments are the main reasons for their broad applications. CR has an opening angle of almost 40° before the reflected power falls below the -3dB limits.

3.2.2. Bi-Directional corner reflector

A two-dimensional SAR image coordinate vector in combination with three-dimensional satellite antenna positions given in a global reference frame provide two constraints for determining the three unknown coordinates of a point on the earth surface in a global reference frame, i.e. they are limiting the unknown location of the point to the “range circle”. Two images from e.g. ascending and descending (AD) orbits allow estimating the point coordinates by intersecting the range circles. This method of using a pair of SAR images to determine the coordinates is known as Stereo-SAR.

Stereoscopic SAR data may be obtained from a number of configurations, same side and opposite side pairs using different orbits. The predominant configuration is an acquisition from ‘adjacent ascending’ or ‘adjacent descending’ orbits. The reason of such a configuration is limited SAR acquisition geometry, signal interaction with a complex 3-d object scene and rarely occurring targets with similar scattering from both ascending and descending orbits. However, in current work opposite orbits are used with scattering from a uniquely designed double-sided corner reflector (DCR) and thus fulfilling ideal situation for the intersection geometry.

The fact that similarly constructed CR’s could be considered a single point source reflector for both the AD orbits was the motivation for such a bidirectional design. The acquisition of SAR image using TSX was constrained to only one side look direction towards the right. This limited the SAR acquisition geometry even further. Having a very large -3db beam-width (mentioned earlier) it was still not realizable to make a reflector visible from AD orbits having one side fixed together for both the reflectors. To overcome this, a modification was made in the design discussed later in section 3.2.5.

A similar bi-directional design of a CR was reported by (Quin and Loreaux, 2013), but due to its rigidity, only single side was imaged during ascending orbital pass only. Hence rejecting the purpose for being visible in both AD passes without a modification in orientation. Another small-sized bidirectional reflector tile was reported by (Cuenca *et al.*, 2014) exploiting the large 3db beam width. For this tiled reflector the RCS observed was significantly lower than expected and the reflector was undetectable.

3.2.3. RCS Simulations using CST

CST is a general-purpose EM simulator (detailed discussion in section 4.1.2), it offers accurate efficient computational solutions for electromagnetic design and analysis in

arbitrary three-dimensional structures. The main product of CST is 'CST Studio Suite' which comprises of various modules dedicated to specific application areas.

For the RCS calculations, 'EM Module' was used. The RCS of a target can be viewed as a comparison of the strength of the reflected signal from a target to the reflected signal from a perfectly smooth sphere of cross-sectional area of 1 m^2 . The description of RCS includes the fact that not all of the radiated energy (by the transmitter) falls on the target. A target's RCS (σ) is visualized as the product of three factors:

$$\sigma = \text{Reflectivity} \times \text{Directivity} \times \text{Projected cross section}$$

where reflectivity is the percent of intercepted power reradiated (scattered) by the target. Directivity is the ratio of the power scattered back in the radar's direction to the power that would have been backscattered isotropically. The projected cross section is the cross-sectional area of the target under observation.

For a triangular trihedral CR, its RCS can be calculated using the following formula

$$\sigma = \frac{4\pi a^4}{3\lambda^2}$$

where a is the small length of the corner reflector in meters, λ is the wavelength of the radar signal in meters, σ is RCS in meters-squared.

The elevation angle refers to angle between the horizontal plane and the beam pointing towards the sensor above the horizontal. A horizontal line in the direction of horizon would be pointing at zero elevation. The CR was placed with one side parallel to the horizontal as seen in Figure 24.

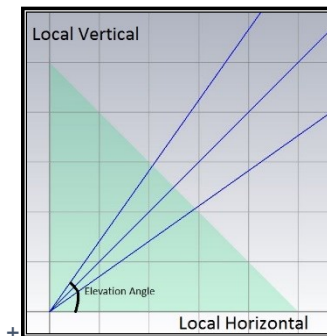


Figure 24 Elevation angles for a horizontally placed CR (RCS calculation)

Initially, a CR pair of side 0.5m was constructed and mounted. Later the size was increased to 1m as the former was not visible in the acquired image. The effect on RCS due to the induced gap was also simulated.

RCS for three different elevations were compared (Table 4) to verify the boresight angle (35.26° from horizontal) commonly misinterpreted as 45° . There was a slight drop in the

RCS due to induced gap but quite acceptable for the CR to be fabricated in the laboratory. Figure 25 compare the effect of the gap in between plates resulting in some loss of 3db beam width in the azimuth direction.

Table 4 CST Simulated RCS at different elevations for corner reflector

Trihedral CR length 1 m wavelength (λ) 0.03m	Elevation Angle (degrees)	RCS (dBm^2) w/o gap	RCS (dBm^2) with gap
	35.26°	35.531	35.1
	45°	35.5	34.52
	54.74°	33.17	31.67

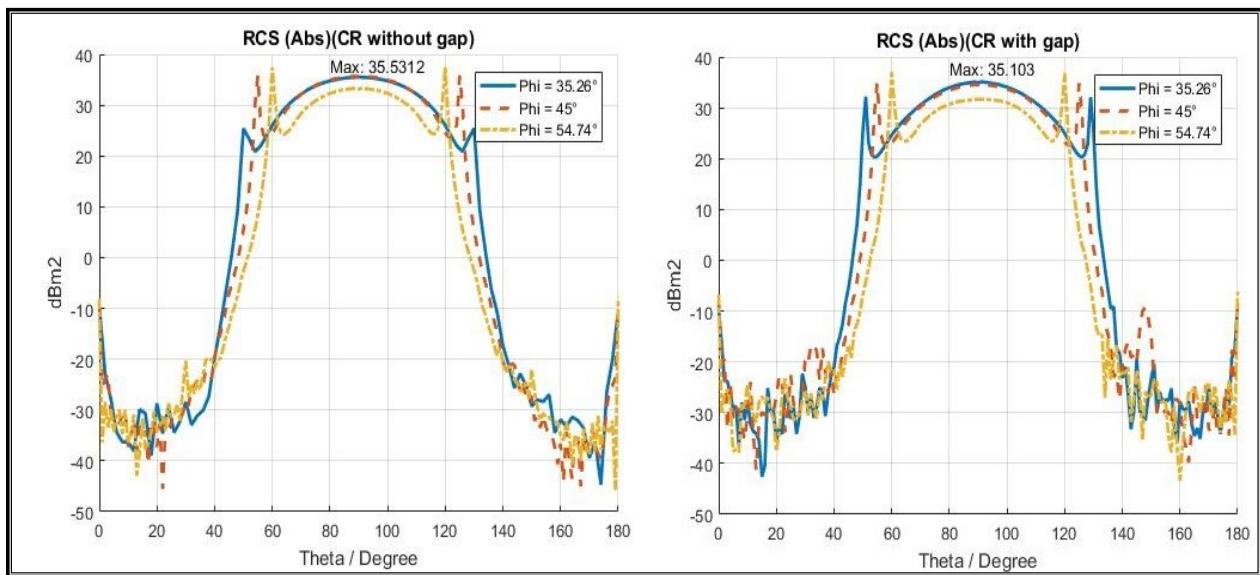


Figure 25 (Left) RCS in Azimuth (CR without gap); (Right) RCS in Azimuth (CR with gap)

3.2.4. CR deviation from theoretical perfection

The uncertainty of the RCS for a CR is mainly governed by the following factors:

- Misalignment from cardinal direction
- Inter-plate orthogonality error
- Plate curvature deviation
- Surface irregularities

Inter-plate orthogonality was the most important tolerance observed and maintained because the reflector’s RCS decreases rapidly as the angle departs from 90° due to the destructive interference of waves reflected from different areas of the plates. This deviation in the inter-plate orthogonality was modelled and results were verified.

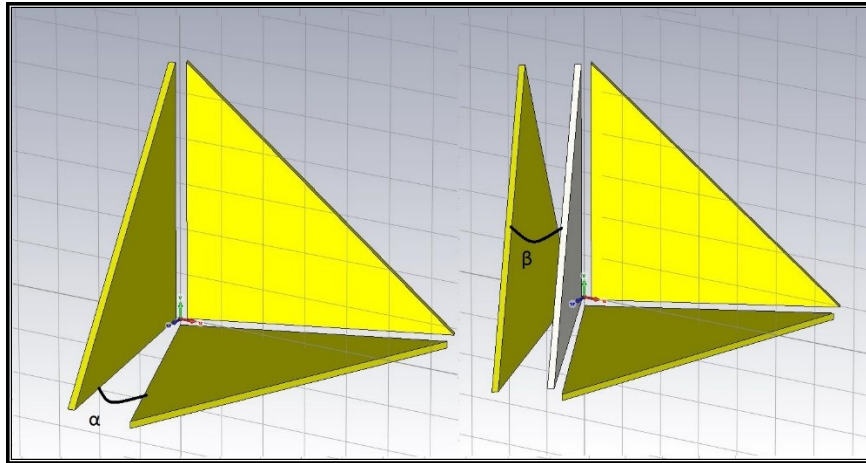


Figure 26 Inter-plate orthogonality deviation modelled for RCS calculation

In the first setup, one side (short edge) of the CR was rotated while keeping the other side fixed (angle α seen in Figure 26, left). With this rotation (α) the orthogonality was deviated for one triangular side only. The rotated side was still orthogonal to the other triangular side. Starting from one degree, RCS was measured at four different positions of α .

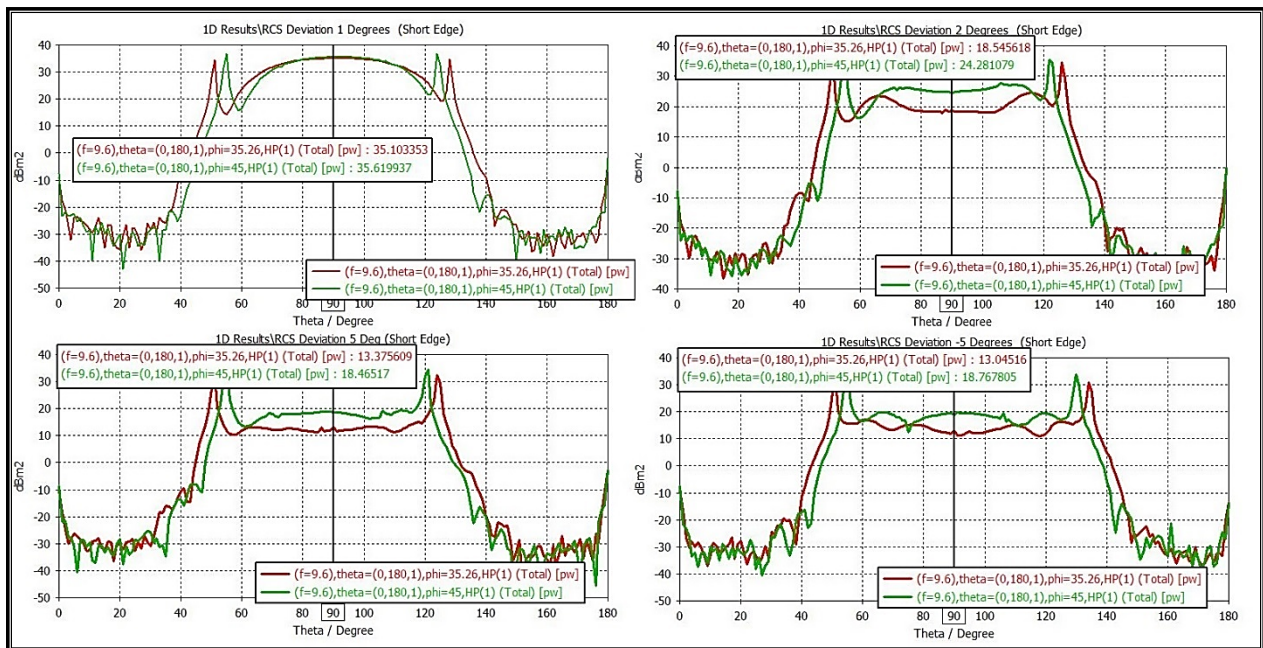


Figure 27 RCS results for different degrees of deviation of α

Figure 27 plots the results of calculated RCS for different values of α . These RCS values were measured at two different elevation angles (35.26° and 45°) for each α .

In the second setup, other side (long edge) of the CR was rotated (angle β seen in Figure 26, right). With this rotation (β) the orthogonality was deviated for both of the triangular

sides of the CR. Again, starting from one degree, RCS was measured at four different positions of β .

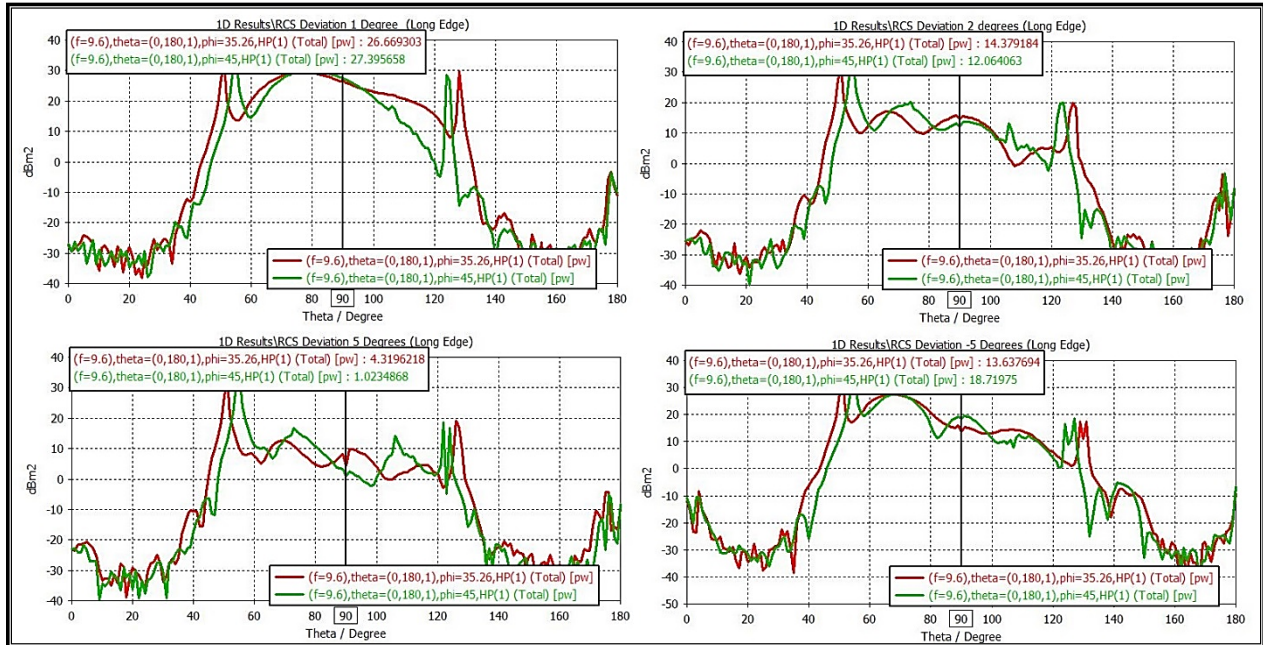


Figure 28 RCS results for different degrees of deviation of β

Figure 28 plots the results of calculated RCS for different values of β . These RCS values were measured at two different elevation angles (35.26° and 45°) for each β .

Table 5 summarize the results for the RCS calculated for the elevation angle of 35.26° . With one-degree deviation of α , there was no significant decrease in RCS value. But as the deviation was increased one more degree, the RCS was reduced to almost half of the original value. The last column in Table 5 measures the difference of RCS from the RCS of a perfect CR. As the deviation was increased to five degrees, the RCS continued to decrease. In the last deviation α was rotated in the opposite direction so as α was negative five degrees. The RCS drop with opposite rotation was similar in magnitude to that of the positive rotation of equal magnitude.

The results were even worse with the deviation of β which rendered one side of the CR non-orthogonal to both other sides. The β rotation of even one degree, decreased the RCS with significant magnitude. With a rotation of five degrees almost all power was lost and did not returned to the sensor (RCS field monitor in this case). With a negative rotation of β , the loss in reflected power was less as compared to the positive rotation of same value. Moreover, it was also verified that the 3-dB beam-width (opening azimuth angle) of the CR also decreased with a slight deviation.

Table 5 RCS comparison at different deviation angles

	Plate deviation (degrees)	Max measured RCS at boresight, dBm^2 ($\phi = 35.26^\circ$)	RCS drop from original, dBm^2 ($35.5 - \text{RCS measured}$)
Short side rotation of CR, α	$\alpha=1^\circ$	35.10	0.4
	$\alpha=2^\circ$	18.54	16.96
	$\alpha=5^\circ$	13.37	22.13
	$\alpha=-5^\circ$	13.04	22.46
Long side rotation of CR, β	$\beta=1^\circ$	26.67	8.83
	$\beta=2^\circ$	14.37	21.13
	$\beta=5^\circ$	4.32	31.18
	$\beta=-5^\circ$	13.63	21.87

3.2.5. Construction and Mounting DCR's

Two requirements were taken care of during its construction: (1) the CR should be able to split in parts so that it could be transported to a rooftop with a narrow passage and (2) the pair should be designed flexible enough to be adjusted in azimuth and elevation while keeping one corner attached (Figure 30). A flexible design should allow to readjust the CR to different satellite tracks for several measurements and having one end attached, absolute distance measurements can be made between the center points of two separated CR's and hence obtaining precise location.

With the required side length of one meter for the CR, the first problem was catered by subdividing each triangular side into four smaller triangles each of 0.5 m sides. Screwed with precision, back support was added for stability. An intentional gap of four millimeters was induced between orthogonal plates to filter rain precipitation and withdraw wind forces. To realize the second requirement of being adjustable and having two degrees of freedom, one side of the CR was attached to a vertical metal rod. The CR was free to revolve and could be screwed fixed to required direction. This accomplished the azimuth rotation from 0° to 180° . Having two such CR's attached back to back all 360° scene was covered by the pair.

Sliding this vertical rod from the base, while keeping the top end of the CR's intact, lifted the CR from local vertical and thus achieving the elevational adjustment. The maximum amount of elevation achieved was dependent on the distance of the slide from the center. Sliding away both the rods at far extremes, a horizontal distance up to 1m could be adjusted. With this distance, the maximum achievable elevation of the base plate was 30° , enough to be imaged by TSX. This slide and rotate mechanism is better perceivable with the CAD diagrams shown in Figure 29 and Figure 30.

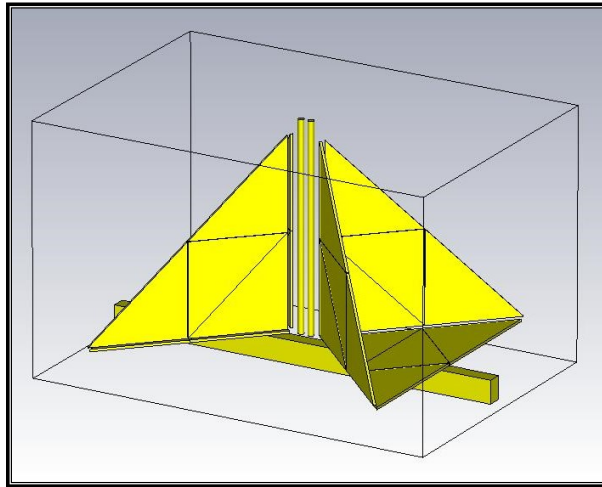


Figure 29 Corner Reflector Pair (Zero Elevation)

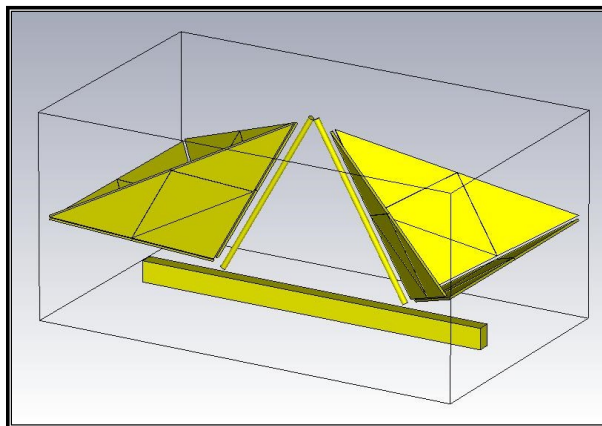


Figure 30 Corner Reflector Pair (30° Elevated)

A free service from DLR was available to compute reference target alignment angles for the TSX mission. This service allows to enter geographic coordinates of reference targets and to specify a relevant time frame. Based on these inputs the alignment angles for the target are computed. (DLR, 2015). Coordinates of the CR installation location were measured using geodetic means (differential GPS). These coordinates were fed to the online DLR service which calculated the visibility (in time) of TSX satellite over this position. Moreover, satellite look direction (left or right), satellite pass direction (AD), azimuth and elevational angles, to align a CR at a specific time, were also calculated by this service.

Table 6 Time and location for TSX image acquisition

Coordinates / Satellite pass Time		Azimuth	Incidence Angle	Sat Look / Pass Direction
52.511795° N 13.327393° E	2016-06-03 16:43:47	168.67°	27.34°	Right/Ascending
	2016-06-05 05:25:08	10.46°	33.20°	Right/Descending

Table 6 summarizes the computed data for the orientation of reflectors to be mounted in Berlin, Germany. According to the calculations, TSX was expected to pass across the mentioned coordinates at this time (2016-06-03, 16:43:47). For the CR to be visible to TSX at this time, it was to be oriented at an azimuth of 168.87°. Magnetic declination (variation between true north and magnetic north) for Berlin is 3°53' and was corrected for. The incidence angle from the local vertical (at the position of CR) to point at the boresight of satellite was to be 27.34°. The orbital pass of TSX was in ascending direction with the TSX antenna pointing to the right of the direction of travel.

Mounting the CR's in the right orientation was purely geometric, adjusting the following two directions precisely, resulted in the maximum backscatter.

A rooftop at the premises of Technical University Berlin was selected as an ideal location for the installation of the reflector pair (Figure 32). With no vegetation or urban obstacles, the line of sight was uninterrupted from DCR to the satellite passes (AD).



Figure 31 Side view and front view of the reflector with small triangular plates (0.5m side length) assembled together to form a bigger reflector (1m side length)



Figure 32 Mounted reflectors viewing in different orbital directions

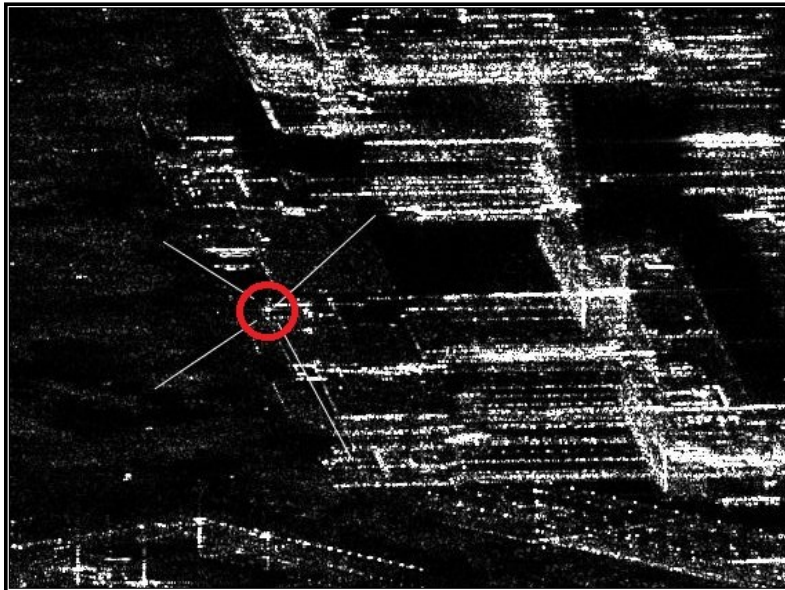


Figure 33 CR as seen in the high resolution TSX image from the ascending orbital pass

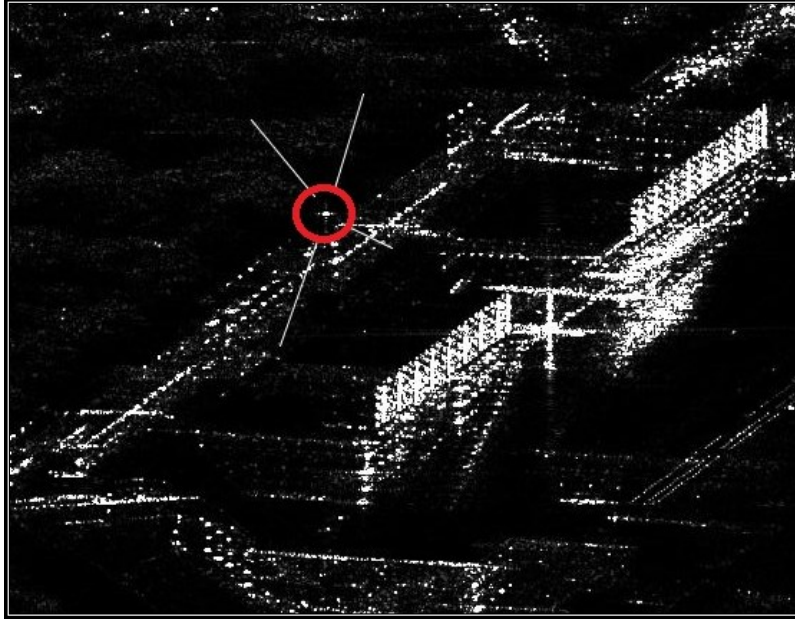


Figure 34 CR as seen in the high resolution TSX image from the descending orbital pass

3.2.6. Azimuthal Orientation

Theoretically, rotating the reflector around the base edge while pointing in the same direction does not change the RCS. The front edge of the CR was made parallel to the flight direction of the satellite with the open part of the reflector facing towards the satellite (Figure 35). This position was relatively easy to be measured and oriented.

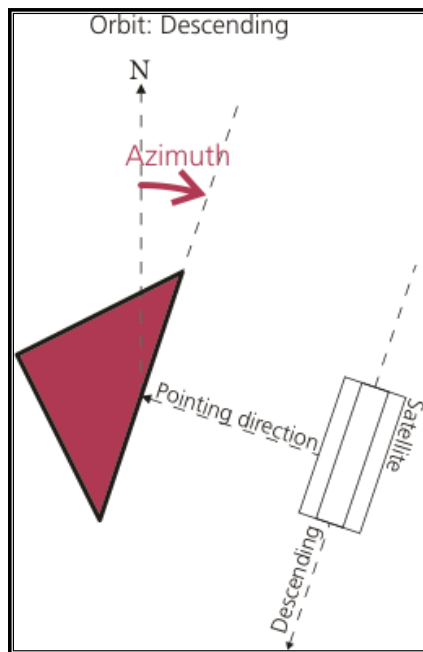


Figure 35 Azimuthal orientation (DLR, 2015)

3.2.7. Elevational Orientation

Elevational orientation was a bit tricky, considering the reflector one-half of a diagonally cut cuboid, the angle of the cube's diagonal with respect the base is $90^\circ - 35.26^\circ = 54.74^\circ$. The elevation of the base plate can be calculated as $E = 54.74^\circ - \text{Incidence angle of the acquisition}$.

So, with smaller incidence angles, the CR is pointing more towards the zenith and with the larger angles, the CR is looking more towards the horizon (Figure 36).

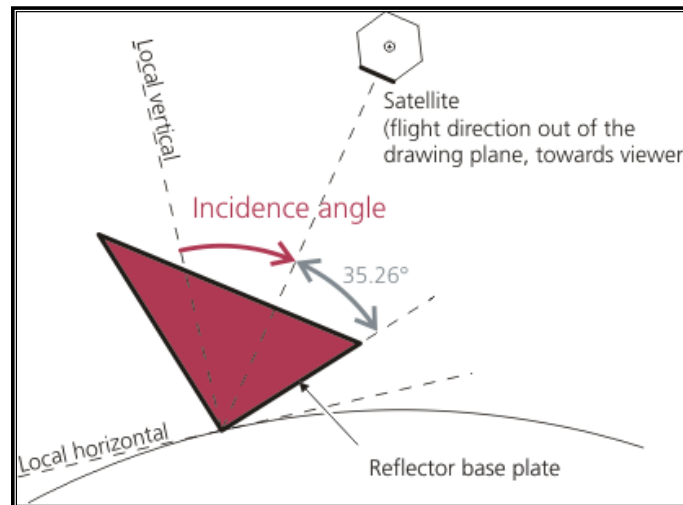


Figure 36 Elevational orientation (DLR, 2015)

3.3. Localization Method and Accuracy

For interferometric SAR, rigorous geometric conditions must be maintained. For interferometry to work, the satellites must be as close as possible to the same spatial position when the images are acquired. The time duration between consecutive acquisitions should be short. Moreover, precise co-registration of images is also required. Stereoscopic SAR is not required to satisfy such tight conditions. From a geometric point of view stereo SAR is extensively discussed in (Leberl, 1990).

The two basic equations treated as observation equations are the Doppler equations and the range equation

$$f_d(t) = \frac{2 * (\vec{V}_s(t) - \vec{V}_t(t)) \cdot (\vec{P}_s(t) - \vec{P}_t(t))}{\lambda |\vec{P}_s(t) - \vec{P}_t(t)|}$$

$$R(t) = |\vec{P}_s(t) - \vec{P}_t(t)|$$

where f_d is the Doppler frequency associated with the return echo data, λ is the radar wavelength, V_s and V_t are the velocity vector of spacecraft and target point, P_s and P_t are the position vector of the spacecraft and target point respectively. R is the sensor to target slant range. The Doppler equation defines the plane of the center of the radar beam at a special instant in time. The use of Doppler equations to define centroid plane instead of pointing direction is inherently more accurate as the Doppler frequency is precisely known.

Deployed DCR's can be seen from opposite orbits. Measured positions of these reflectors by regular geodetic methods (GPS techniques) are used to validate the positioning accuracy of our method.

3.3.1. Point Target Analysis (PTA)

As mentioned before, the product annotation contains the relevant state vectors in earth-fixed co-ordinates system. The given spacing is 10 secs in between the two state vectors. The first crucial step was to find the exact reference time for the localization of the SAR pixel in the image. The detection of the CR in the acquired SAR image is done via 'point target analysis' performed by the Radar-Tools (RAT) (Reigber and Hellwich, 2004). In order to obtain the timings a square window centered on the reflector is extracted from the SAR image. An interpolation is performed where the values are refined in the vicinity of the maximum intensity. Using such a technique, subpixel accuracy is achieved. After that these values are converted to radar timing using the annotated state vector data.

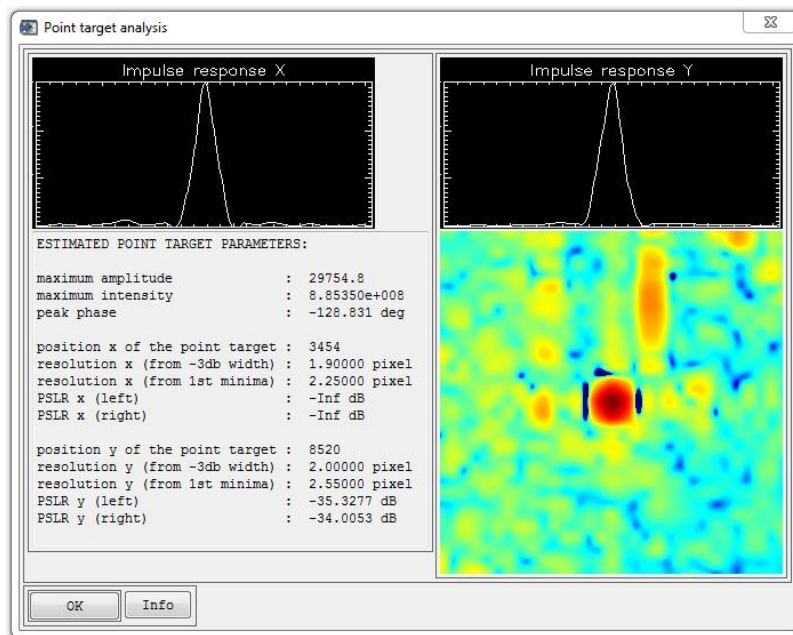


Figure 37 Point target analysis (ascending orbital acquisition)

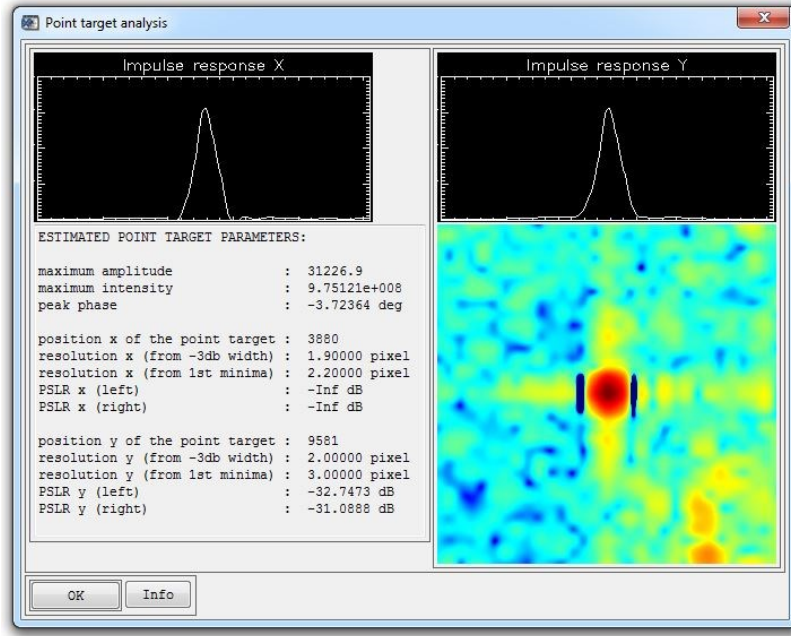


Figure 38 Point target analysis (descending orbital acquisition)

3.3.2. Orbital Interpolation

The raw data is focused to zero doppler azimuth-time by the TSX SAR processor. Azimuth time t_A is introduced via analytical trajectory model. A straightforward approach was the application of classical polynomials:

$$x_s = a_0 + a_1 t_A + a_2 t_A^2 + \dots + a_6 t_A^6$$

$$y_s = b_0 + b_1 t_A + b_2 t_A^2 + \dots + b_6 t_A^6$$

$$z_s = c_0 + c_1 t_A + c_2 t_A^2 + \dots + c_6 t_A^6$$

$$v_{x_s} = a_1 + 2a_2 t_A + \dots + 6a_6 t_A^5$$

$$v_{y_s} = b_1 + 2b_2 t_A + \dots + 6b_6 t_A^5$$

$$v_{z_s} = c_1 + 2c_2 t_A + \dots + 6c_6 t_A^5$$

The polynomial coefficients $a_0, a_1 \dots, b_0, b_1 \dots, c_0, c_1 \dots$ are estimated by least squares method from the sensors trajectory's given by orbit state vectors. A sixth-degree polynomial was chosen, increasing to a degree greater than six did not make a significant impact on the final target coordinate results (Gisinger *et al.*, 2017).

For an overdetermined system of 'm' linear equations in 'n' unknown coefficients with $m > n$, can be written in a matrix form:

$$X\alpha = y$$

where

$$X = \begin{bmatrix} x_{11} & \cdots & x_{1n} \\ \vdots & \ddots & \vdots \\ x_{m1} & \cdots & x_{mn} \end{bmatrix}, \alpha = \begin{bmatrix} \alpha_1 \\ \alpha_2 \\ \vdots \\ \alpha_n \end{bmatrix}, y = \begin{bmatrix} y_1 \\ y_2 \\ \vdots \\ y_n \end{bmatrix}$$

Such a system usually has no solution, so the goal is instead to find the coefficients which fit the equations best, in the sense of solving the quadratic minimization problem (Lai, Robbins and Wei, 1978)

$$\hat{\alpha} = \arg \min S(\alpha)$$

where objective function S is given by

$$S(\alpha) = \|Y - X\alpha\|^2$$

This minimization problem has a unique solution, provided that the 'n' columns of the matrix 'X' are linearly independent, given by solving the normal equations

$$(X^T X)\hat{\alpha} = X^T Y$$

Finally, α is the coefficient vector of the least square hyperplane expressed as

$$\hat{\alpha} = (X^T X)^{-1} X^T Y$$

Applying this least square solution to previously modeled polynomial equations takes the following form

$$X = \begin{bmatrix} 1 & t_{A1} & t_{A1}^2 & \cdots & t_{A1}^6 & 0 & \cdots & 0 \\ 1 & t_{A2} & t_{A2}^2 & \cdots & t_{A2}^6 & 0 & \cdots & 0 \\ \cdots & \cdots \\ 1 & t_{A12} & t_{A12}^2 & \cdots & t_{A12}^6 & 0 & \cdots & 0 \\ 0 & \cdots & 0 & 1 & t_{A1} & t_{A1}^2 & \cdots & t_{A1}^6 & 0 & \cdots & 0 \\ 0 & \cdots & 0 & 1 & t_{A2} & t_{A2}^2 & \cdots & t_{A2}^6 & 0 & \cdots & 0 \\ \cdots & \cdots \\ 0 & \cdots & 0 & 1 & t_{A12} & t_{A12}^2 & \cdots & t_{A12}^6 & 0 & \cdots & 0 \\ 0 & \cdots & 0 & 1 & t_{A1} & t_{A1}^2 & \cdots & t_{A1}^6 & & & \\ 0 & \cdots & 0 & 1 & t_{A2} & t_{A2}^2 & \cdots & t_{A2}^6 & & & \\ \cdots & \cdots \\ 0 & \cdots & 0 & 1 & t_{A12} & t_{A12}^2 & \cdots & t_{A12}^6 & & & \end{bmatrix} \alpha = \begin{bmatrix} a_0 \\ a_1 \\ \cdots \\ a_6 \\ b_0 \\ b_1 \\ \cdots \\ b_6 \\ c_0 \\ c_1 \\ \cdots \\ c_6 \end{bmatrix} Y = \begin{bmatrix} x_{s1} \\ x_{s2} \\ \cdots \\ x_{s12} \\ y_{s1} \\ y_{s2} \\ \cdots \\ y_{s12} \\ z_{s1} \\ z_{s2} \\ \cdots \\ z_{s12} \end{bmatrix}$$

The achieved interpolation accuracy was a fraction of a millimeter.

3.3.3. Space Intersection

After obtaining precise azimuthal position and range time, constant range circles perpendicular to the orbital plane are constructed.

To realize the plane perpendicular to the orbital plane, a tangent vector to the orbit and a normal vector to this point is required. The tangent line is given as

$$\text{tangent}(f(x)) = f(x_0) + (x - x_0) * f'(x_0)$$

Another vector from the center of this plane to this precise azimuth point was also required to obtain a perpendicular to this plane. Cross product of the two vectors (origin vector and tangent vector) resulted in the normal vector in which the plane was spanned.

The parameterization of constant range circle centered at interpolated coordinates c_x, c_y and c_z are given by

$$x(\theta) = c_x + R (\cos \theta a_x + \sin \theta b_x)$$

$$y(\theta) = c_y + R (\cos \theta a_y + \sin \theta b_y)$$

$$z(\theta) = c_z + R (\cos \theta a_z + \sin \theta b_z)$$

where a_x, a_y, a_z and b_x, b_y, b_z are two unit vectors perpendicular to the direction of the axis containing the interpolated points and to each other, θ varies from 0 to 360° to span a complete circle.

Now the intersection point was required for the two circles. Theoretically, the circles will not intersect precisely, rather pass by with some distance in between. Two locations of such a pass-by are expected of the two drawn circles. One closer to the surface of the Earth, other towards the zenith, opposite to the Earth's surface. In general, the distance between two circles is an algebraic function of the parameters defining them, but this function is not solvable in terms of radicals. The result (Neff, 1990) implies that one cannot find a "closed-form" solution for the distance between an arbitrary pair of circles. The minimum Euclidian distance was calculated exhaustively for each theta on the first circle to each theta on the second circle. However, the calculations were performed iteratively with a coarser mesh (the divisions on angle theta) initially and a finer mesh when the distance approached the minima and thus conserving time and computational resources.

For visual perception, Figure 39 shows the plotted range circles on the precisely interpolated values of the satellite trajectory. To avoid the ambiguity of the two possible intersection points, earth's surface is plotted in Figure 40 with a constant radius and without external reference data. Range circles intersecting with Earth surface is the reference point where the bi-directional reflectors are mounted.

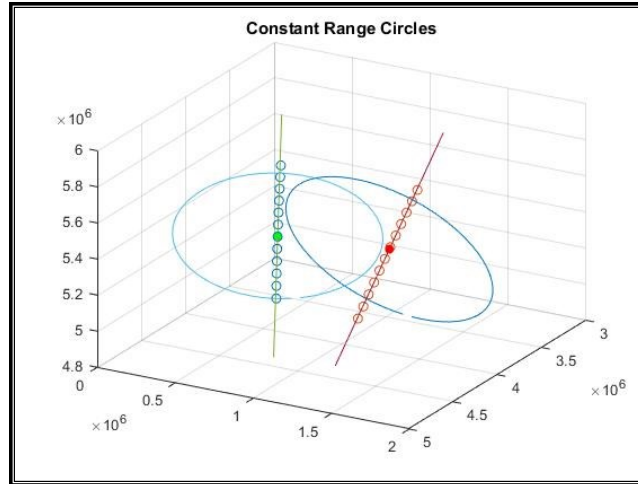


Figure 39 Range circles at zero Doppler, (green) ascending orbit, (red) descending orbit

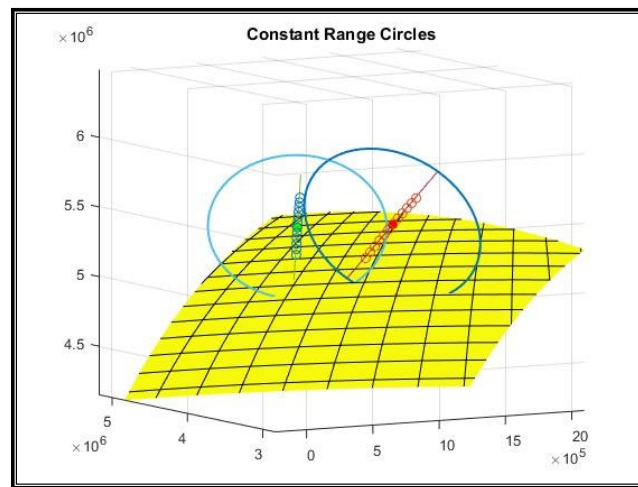


Figure 40 Range circles with earth surface and the intersection point

3.3.4. Atmospheric and other Corrections

The orbital state vectors in the metadata are shifted precisely to the SAR antenna center. Instrument's attitude information is used to make this shift which is about 0.8m in the range direction (Fritz, Breit and Eineder, 2008). Range time, which is the two-way radar pulse travel time is already corrected to the internal instrumental delay in the metadata. This range time refers to zero doppler location and the position is geometrically perpendicular to the orbit at this time. Range time, as mentioned before, is not corrected for atmospheric delays in the complex image products (Fritz, Breit and Eineder, 2008). The ionospheric delay is not significant at the X-band and causes range errors at centimeter level. The tropospheric delay is up to several meters and must be corrected to obtain precise location (Table 8). The annotation file contains the range delay polynomials for simple tropospheric and ionospheric models for corrected signal path delay. In each of the annotated file, one coefficient for a constant total delay is

given. Table 7 reviews the signal propagation effects as seen in the annotated file available with each of the TSX acquisition.

Table 7 Annotated signal propagation effects

Ascending Orbit	<pre><signalPropagationEffects> <rangeDelay modelName="averageTECU_5" modelVersion="1.0" source="IONO"> <polynomialDegree>0</polynomialDegree> <coefficient exponent="0">1.66276808693899029E-10</coefficient> </rangeDelay> <rangeDelay modelName="hydrostatic" modelVersion="1.0" source="ATMOS"> <polynomialDegree>0</polynomialDegree> <coefficient exponent="0">1.74382741705918483E-08</coefficient> </rangeDelay> </signalPropagationEffects></pre>
Descending Orbit	<pre><signalPropagationEffects> <rangeDelay modelName="averageTECU_5" modelVersion="1.0" source="IONO"> <polynomialDegree>0</polynomialDegree> <coefficient exponent="0">1.79104606352410235E-10</coefficient> </rangeDelay> <rangeDelay modelName="hydrostatic" modelVersion="1.0" source="ATMOS"> <polynomialDegree>0</polynomialDegree> <coefficient exponent="0">1.87734030914526169E-08</coefficient> </rangeDelay> </signalPropagationEffects></pre>

Table 8 Atmospheric delay corrections applied

	Range Time delay coefficient, t_d (Ascending Pass)	$(t_d \times c)/2$	Range Time delay coefficient, t_d (Descending Pass)	$(t_d \times c)/2$
Ionospheric delay (m)	1.66276808693899029E-10	0.0249 m	1.79104606352410235E-10	0.0268 m
Tropospheric delay (m)	1.74382741705918483E-08	2.6139 m	1.87734030914526169E-08	2.8141 m

3.4. Results and Discussion

To summarize, it was demonstrated that by the use of stereo image-based target localization, meter level accuracy was achieved. Where only errors of relatively larger magnitudes were incorporated. Table 9 summarizes the major error sources in the localization and their relative magnitudes. As mentioned before, the TMSP processor rectifies many error sources beforehand. The rest are to be performed by the user after the acquisition of the image.

Table 9 Summarizing the sources of errors in localization and the stage where they are corrected.

Direction of error	Source of error	Magnitude of error	Correction stage
Azimuth	Instrument time tag delay	~1.27 m	Not corrected at TMSP
Range	SAR antenna shift	~80 cm	Corrected at TMSP
	Ionospheric delay	~2.5 cm	Not corrected at TMSP
	Tropospheric delay	~2.7 m	Not corrected at TMSP

Table 10 Precise measurements of experimental setup

	TSX ascending pass	TSX descending pass
Satellite position (x,y,z)	4197710.648409 m 701210.6909137 m 5406766.270657 m	4053451.639845 m 1335478.594453 m 5397536.607417 m
Incidence angle	27.280426°	33.163966°
Radius of Earth	6378137 m	
Speed of light, c	299792458 m/s	
Slant Range time	3915855 x 10 ⁻⁹ s	4187087.2 x 10 ⁻⁹ s
Range	586971.897810 m	627628.581774 m
Range corrected	586974.536666 m	627631.422683 m

Table 10 displays the location of TSX satellite at the time of acquisition in Earth centered earth fixed coordinates (ECEF). These locations are a result of interpolation after the time and location information was extracted from the metadata. Range distance was calculated using the two-way slant range time for the localized pixel. Last row shows the corrected range after the range and azimuth errors were accounted for.

Table 11 Geodetic surveyed location of installed reflectors and ranging error

	Ascending	Descending
Surveyed target position (reflector's center) (x,y,z)	3785228.136255955 m 896703.057928829 m 5037740.635266454 m	
Range error	-0.9523857 m	-0.9986874 m

The central mounting point of the reflector pair was surveyed (Table 11) for more than fifty measurements using Leica Viva GNSS antenna. The accuracy of this survey is expected to be at the scale of few centimeters. The range error was calculated as a difference of surveyed range (distance from the surveyed reflector coordinates to the interpolated satellite orbital position) to the range calculated from localization technique. This error measurement is not the 3-d error but is only the difference in the calculated range from orbital intersection and range from surveyed coordinates. The absolute localization error between them is a couple of meters. Incidence angle adjustments were not performed and hence very small instabilities in the incident angle could lead to large errors in the absolute localization.

Moreover, minor error sources like solid earth tides, plate tectonics movement, ocean loading, atmospheric pressure loading, pole tides, ocean pole tide loading and atmospheric tidal loading were neglected as they are at millimeter range and added complexity which was not the goal of current research.

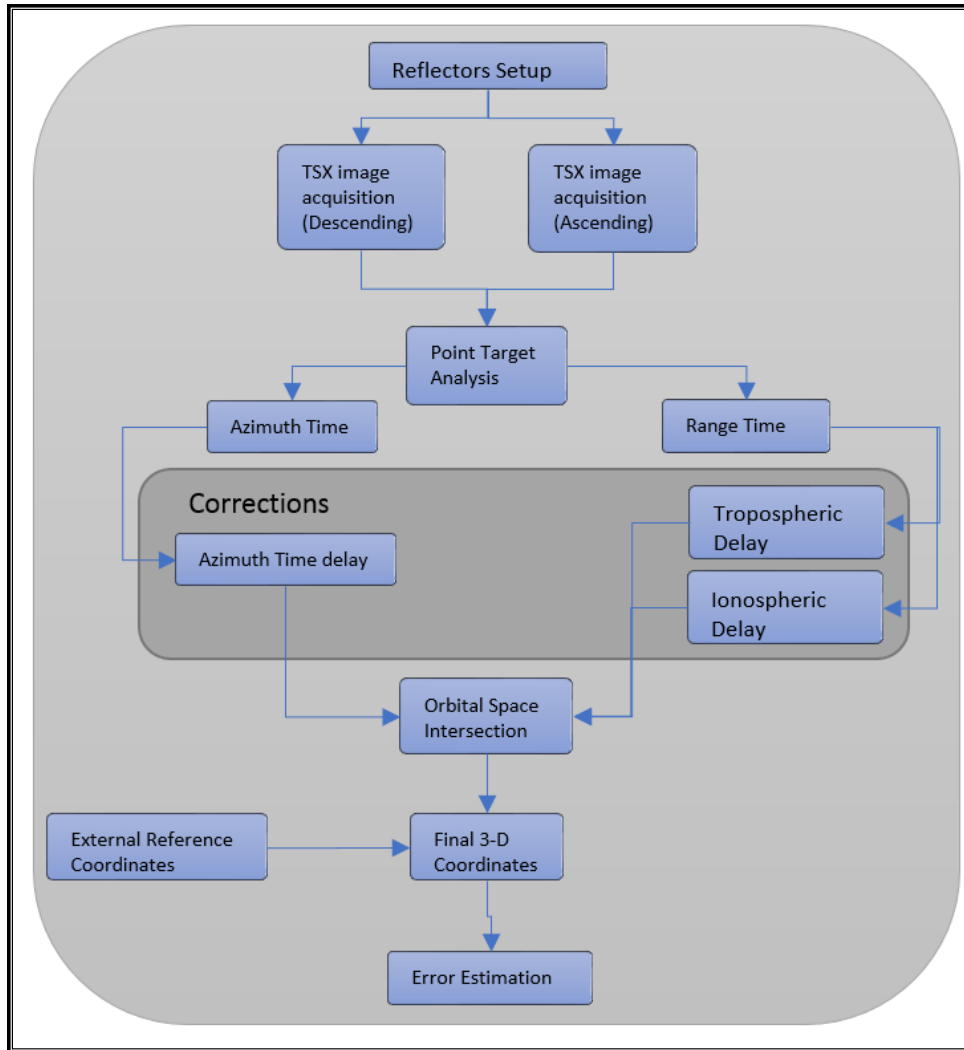


Figure 41 Flowchart summarizing the process of localization using double corner reflectors

A sequential procedure described in the current chapter is summarized using a flow chart in the Figure 41 where the corrections performed are again highlighted in the middle of the chart.

An absolutely common scattering point for both CR's viewing in opposite direction was not realizable because of the limitation of SAR acquisition geometry (20° to 55° off-nadir angle for TSX). However absolute distance measurements can be made between the center points of two separated CR's and, hence obtaining precise location. The use of poles or objects of symmetrical construction, where the visibility is not interfered from cross directional orbits is left as future work.

Chapter 4: CST for SAR Simulation and its Limitations

4.1. Introduction

This chapter gives an in-depth analysis for different types of simulators in the field of electromagnetics and the motivation for the use of CST. Each step to perform a SAR simulation using this software is elaborated. Different types of available solvers are also discussed. Afterwards, the complex SAR focusing algorithm used in the processing of TSX images is compared with the simplified range doppler algorithm adapted for our simulation. Several simulation cases using single and multiple targets are performed. Towards the end of the chapter, the unsuitability of such a simulator for large sized objects is stated. Lastly, the possible sources of errors are discussed with their effect on the accuracy of simulation and methods to mitigate them.

4.1.1. Need for Simulation

In the radar community simulation is now a well-known practice. Developing, implementing and testing actual SAR can be complicated and an expensive task, whereas a simulation provides a relatively low cost and comparatively easy solution to achieve several outcomes. Some of them are discussed below. Foremost, it allows us to study and understand the complex-scattering effects of non-naturally existing objects such as buildings, roads, bridges etc. (Hammer, Kuny and Schulz, 2014), (Auer, Gernhardt and Bamler, 2011), (Auer, 2011). With the freedom of adjusting variables, one can configure a simulation for a variety of formations such as different angles of image acquisition. For better interpretation of SAR images with controlled parameters, microwave propagation can be simulated, hence aiding to the understanding the effect of different geometries, electromagnetic properties of different urban structures etc. It's not only the interaction of EM waves and matter to be taken into account while simulating SAR, also indirect beams being diffracted from object edges, direct reflection and other SAR phenomenon already discussed in Chapter 2 are to be considered. Another such use of a simulator is where SAR images are subjected to automated or aided target recognition (Chang, Chiang and Chen, 2011), (Tupin, Bloch and Maitre, 1999), (Wu, Wang and Wen, 2016). Having one database of simulated objects helps this automated process of target recognition. Its use has also been reported for damage assessment of man-made objects after a natural disaster (Brunner, Lemoine and Bruzzone, 2010), (Di Martino *et al.*, 2007). In a field called SAR tomography, a simulator is used to produce 3-D SAR images. Accuracy assessment for SAR and interferometric SAR is also amongst the goal of SAR simulation. Lastly, not only it assists in the analysis of SAR algorithms but also works as a pre-step for the verification of new sensor designs.

In the current work, as mentioned before, SAR simulator aims to help identify the origin of backscattering contributions from the building facades and other man-made objects.

4.1.2. Comparison and Motivation for CST

As categorized by (Franceschetti, Migliaccio and Riccio, 1995) the two-distinct types of SAR simulations are 'direct image simulator' and 'raw data simulator' (Figure 42). In the first one, there are no intermediate products available and the image is simulated based on the input parameters. In the latter, raw data is generated first and after further SAR-focusing algorithms, the final image is generated. The raw signal simulator is however not a substitute to SAR simulation but helps in a better understanding of geophysical information in SAR image. Sometimes just the electromagnetic interaction of SAR signal with the object is required. A phenomenon like volumetric scattering, speckle effect can further complicate the process of simulating SAR. Moreover, nonlinear effects such as layover, foreshortening, and shadowing also need to be considered for a very accurate SAR simulator.

Another subclassification of simulators is possible, categorizing them into point target simulator and extended scene simulator. For a point target simulator, modeling system parameters are of a greater significance whereas for an extended scene one may incorporate complex backscattering models.

Raw data simulators may not be applicable for large urban areas requiring significant computational resources. Whereas direct image simulations are implemented by methods called raytracing (rendering an image by tracing the path of light and simulating the effects when the light interacts with the objects inside the plane) and rasterization which are time efficient. One reason for time efficiency might be an oversimplification of the actual SAR process. This simplification might be acceptable for assistance in image understanding or exploring other SAR phenomenon.

To break down the simulation problem to a basic level what is required is the electromagnetic characterization of the scene, more precisely how the incident and scattered fields are related. The amplitude of this scattered field is governed by so-called backscattering coefficient. Then comes the problem of the type of scattering which can be surface or volumetric scattering. Then SAR algorithms are applied to the collected backscattered electromagnetic data to obtain SAR image. For a comparison of simulated images to real SAR images, it is also important to simulate the radiometric properties. Moreover, replicating the material properties into the simulation also plays a critical role in the accuracy of the simulation.

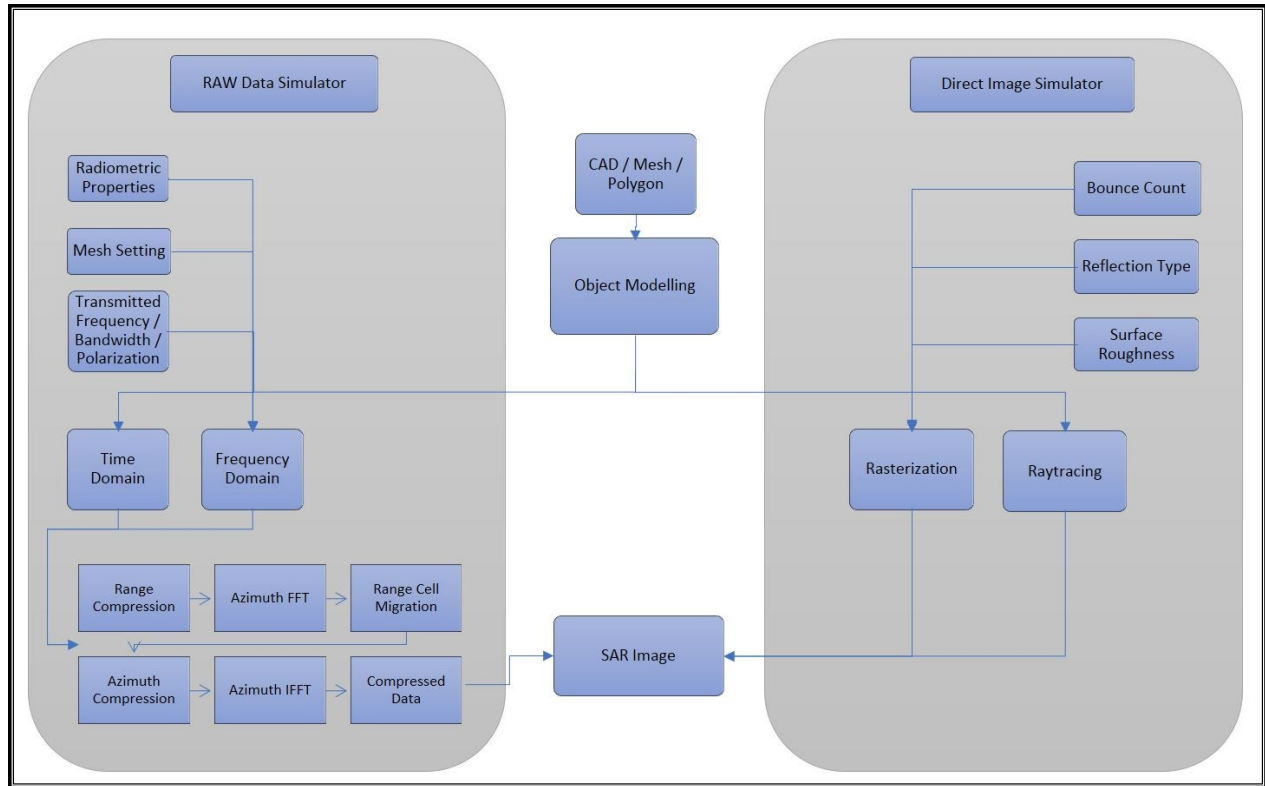


Figure 42 Overview of the two-distinct types of SAR simulators

Significant work is done in simulating SAR images and it started as early as three decades ago. SARAS, a raw signal simulator was introduced (Franceschetti *et al.*, 1992) where a reflectivity map of an extended 3-d scene was computed (One may refer to Figure 43 for graphical view of SARAS). The raw signal was evaluated by means of a system function computed in two-dimensional Fourier domain. A function describing the height profile of scene to be simulated was approximated by square plane facets. The size of facet was large compared to incident wavelength and small compared to cell resolution. Either three vertices or center coordinates with the normal direction were used to categorize these facets. Moreover, electromagnetic properties of the material such as conductivity and permittivity were allocated to each facet. After the superimposition of returns from each facet was done, the raw signal was generated. For each facet, the backscattering was calculated taking into account incident angle, polarization of the wave and surface roughness. The incident electromagnetic field was taken as

$$E_i = \hat{e}E_o \exp(-jz \cdot R)$$

where \hat{e} is the unit polarization vector, z is the propagation vector and R is the distance from the object to the antenna. The backscattering field was calculated by Kirchhoff's physical optical model (Tsang, Kong and Shin, 1985)

$$E_s(R) = \frac{jz \exp(-jzR)}{4\pi R} E_o(\underline{1} - \hat{z}\hat{z}) \cdot \int_0^A F(a, b, c) \exp(2jz \cdot \rho) dA$$

where the Fresnel coefficient of the facets are incorporated in function F. Moreover, the function incorporates the type of polarization and dependence of incidence angle. For more details one might refer to (Tsang, Kong and Shin, 1985).

For SARAS multiple reflection and volumetric scattering were completely neglected. The working of this simulator starts after locating each facet from a grids height profile where this grid is inserted from a simple numeric file. After one random starting point is selected, several facet constructions are possible where simplicity and accuracy are preferred while making a selection. With this facet model, the whole scene is approximated by a piecewise planar surface. Each facet is assumed smaller than the resolution and larger than the electromagnetic wavelength being used. After the evaluation of backscattering coefficient, its Fourier transform is computed. This particular transformation enables handling of large data and also reduces the computational and time complexity. As the last step, this Fourier transformed data is multiplied by a transfer function which also incorporates range curvature and cell migration effects. An inverse Fourier transform with some post-processing results in the final SAR raw image.

To summarize SARAS, it uses an analytic SAR system transfer function, evaluates the backscattered EM fields of an extended scene and uses a 2-d Fourier transform code to complete the process. Polarimetric backscattering and geometric distortion are also considered during the simulation.

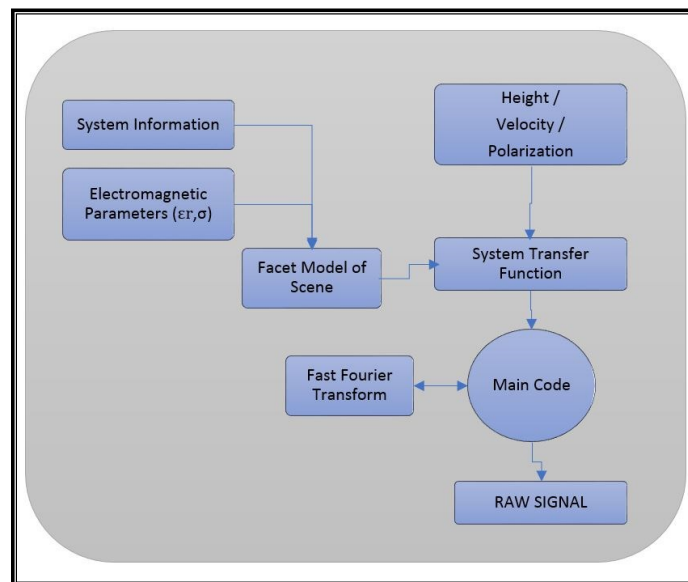


Figure 43 Overview SARAS: a raw signal simulator

For a SAR simulation, the input data format is critical, moreover how the input data is oriented plays a vital role in generating SAR image. Planar facets used in SARAS were with a uniform grid spacing. This might not be for a real acquired data. Moreover, these datasets may have their own format and grid spacing. An interpolation was required to make generally available data compatible with this simulator. A new interpolation technique was proposed (Franceschetti, Migliaccio and Riccio, 1994) and simulation results were also enhanced. Another update was presented (Franceschetti *et al.*, 2003) where a non-flat dielectric plane was introduced underneath the building. Same Kirchhoff's model approximation was applied but a closed form solution was used to evaluate the scattering contribution. Algebraic parametric formulas were solved rather solving complete integrals and equations. Moreover, multiple reflections were also forecasted using the adapted geometric model. This method was computationally feasible in terms of time consumed compared to the previous method.

Amongst several other ray tracing simulators one was CohRas (Hammer and Schulz, 2009) developed on the ray tracing concept (Amanatides and Woo, 1987). The main intent was a simulation of a small scene so that sample data could be generated for classification and training purposes. Polygons were used to model 3-d structures but with the restriction of being convex in shape. The focus was made on generating very small images and a database.

In CohRas, a twofold model was applied where Lambertian scattering was used to calculate diffuse reflection given by

$$\sigma_{diffuse} = \sigma_o \cdot \cos^2(\theta)$$

where θ was the local incidence angle and σ_o backscattering coefficient at the surface. The second type of reflection, specular reflection, was modelled as

$$\sigma_{specular} = \sigma_{max} \cdot \cos(\theta) \cdot \cos(\gamma)$$

Where an additional angle γ was added which was the angle between the specular angle and the direction towards the observer. This was motivated by the fact that reflected energy for a specular reflection is not only true in specular direction but also in shape of a cone surrounding this point.

Another worth mentioning is SAR simulator SARVIZ (Balz and Stilla, 2009) simulating runtime SAR data. Rasterization approach was used where the input image is described in vector graphics format and then converted to a raster image. Graphics processing units (GPU's) were used for processing which rendered data in runtime. The geometric accuracy was questionable as multiple bounces could not be simulated using this rasterization approach.

These simulators are compared in detail (Balz, Hammer and Auer, 2015) discussing the potentials and limitations of each of them. It was concluded that all the simulators were capable of simulating a basic object with one outperforming the other either in terms of geometric correction, time duration or computational efficiency.

A different approach to simulate SAR was to make use of existing electromagnetic field simulators which were designed for general purpose EM simulations. These general-purpose EM softwares usually have a built-in 3-d modeler to design objects. Having a different type of solver methods various scenarios can be realized. One such approach was applied (Mishra and Mulgrew, 2009) where SAR method was realized by revolving receiver antenna whereas the transmitter antenna was fixed. FEKO, a general-purpose EM software, was used to simulate in such a manner. The scattered E-field samples were converted into K-space domain (an uncommon practice). For different azimuth positions, the data was sampled so as to replicate synthetic aperture setup. The data from polar to rectangular format was converted and interpolated using keystone sampling algorithm (Jakowatz *et al.*, no date). Finally, inverse Fourier transform was taken to obtain SAR image. Bistatic SAR was implemented by having the transmitter fixed and rotating the receiver. The resolution and quality of the generated image was dependent on the bistatic angle. For an angle greater than 90° the image quality was unacceptable as k-space data is nulled at higher degrees.

To summarize, after inputting the CAD model to FEKO, setting up required parameters such as frequency, angle, step width, elevation and azimuth the simulation is started. It calculates the surface current on the simulated object, having this surface current in hand, far field is calculated at required azimuth and elevation angles. The results were not quite promising and the fact that 'bistatic SAR' was implemented instead of 'monostatic SAR' which opposes the real-world scenario.

To design another simulator from very scratch would be like reinventing the wheel. This idea of a general-purpose electromagnetic simulator was carried forward to adapt for our needs of SAR simulation. Some prerequisites were in mind before the selection of any software where the ability of the software to perform our required task was at the top of the list. For CST, expertise support was also available from within the university (Rolf Schumann, personal communication, September 01st, 2015, Berlin). It was ensured that software is capable of handling our requirements and was able to setup the simulation scenario in the required way (CST introductory course, November 24th, 2014, Darmstadt).

Amongst several other studios inside the CST studio suite, Microwave Studio is used. Following are some of the capabilities of the simulator which also motivated for the use of this software.

- For lossless and lossy materials, one can use the transient solver (discussed in section 4.3.1), it can swipe a broad spectrum from a single calculation by applying discrete Fourier transform to time signals.
- Fairfield calculations and RCS area calculations are amongst the features used in the current research.
- Having adaptive sampling, frequency domain solver (discussed in section 4.3.2) supports two types of meshes, tetrahedral as well as hexahedral.
- Two different viewing options are available for the objects, first as a 3-d model view and the second as a Schematic view, the Schematic view can be used for circuit simulations.
- Frequency domain solver also supports simulating highly resonant structures in a two-step process calculating the S-parameters first and then the fields are calculated.

4.2. Simulation Workflow

4.2.1. Coordinate System and Units

Two types of coordinate systems, Local and Global coordinates are available for modelling the structures in CST. This gives the user the flexibility to model bigger structures with several components. A structure can be defined locally when selecting local coordinate system. Now this structure is independent of the global coordinates and by performing any structural transformation other objects will not be affected. Local coordinates can be attached to any modelled object than this model will own these coordinates throughout the rest of the simulation. Local coordinates are also called working coordinates where individual objects can be modelled and transformed irrespective of the global coordinates.

Physical units, adapted from International System of Units (SI), are crucial for the clarification and validation of results. Moreover, they are needed to setup the simulation and to annotate when some sort of data is imported. The units are unambiguously defined in the SI system and more details are documented on the help page available offline within the software.

Millimeters (mm), Kelvin (K) and Gigahertz (GHz) are units set for dimensions, temperature and frequency, respectively. When a unit is changed, all expressions including this unit are multiplied with the change factor e.g. changing frequency from Hz to MHz all frequency expressions will be multiplied by 1×10^6 .

4.2.2. Materials

To allow for realistic modelling, different properties for the materials being used in the simulation must be considered. Two very basic materials available are vacuum and

Perfect Electric Conductor (PEC). Moreover, in CST any existing material can be selected from the materials library and even more complex materials can be defined. Non-linear and linear behavior can also be modelled in the frequency domain. For linear behavior magnetic material properties and dielectric material properties determine the ratio of magnetic and electric flux and field density respectively:

$$\vec{D}(\vec{r}, \omega) = \varepsilon_0 \vec{\varepsilon}(\vec{r}, \omega) \cdot \vec{E}(\vec{r}, \omega)$$

$$\vec{B}(\vec{r}, \omega) = \mu_0 \vec{\mu}(\vec{r}, \omega) \cdot \vec{H}(\vec{r}, \omega)$$

For vacuum, permeability and permittivity are defined as

$$\varepsilon_0 \cong 8.85 \times 10^{-12} [F/m]$$

$$\mu_0 \cong 4\pi \times 10^{-7} [H/m]$$

Complex permittivity and permeability come into play when modeling material losses, meaning that the parameters of the materials have a complex and imaginary part and they are frequency dependent. The losses are specified by their loss angles or their loss tangent delta values

$$\varepsilon(\omega) = \varepsilon'(\omega) - i\varepsilon''(\omega) = \varepsilon'(\omega)[1 - i \tan(\delta_e(\omega))]$$

$$\mu(\omega) = \mu'(\omega) - i\mu''(\omega) = \mu'(\omega)[1 - i \tan(\delta_m(\omega))]$$

where δ_e and δ_m are the ratio between imaginary and real parts of complex permittivity and permeability, respectively.

$$\tan(\delta_e(\omega)) = \frac{\varepsilon''(\omega)}{\varepsilon'(\omega)}$$

$$\tan(\delta_m(\omega)) = \frac{\mu''(\omega)}{\mu'(\omega)}$$

If a lossy material is simulated, there is a good penetration of electric field inside but not like that of a perfect electric conductor. A one-dimensional surface impedance model is used which takes into account the skin-depth without modifying mesh setting for these materials. This is valid only for a given frequency range where the dimensions and material properties must be accounted for. The skin depth

$$\delta = \sqrt{\frac{2}{\omega \mu_0 \mu \sigma}}$$

should be smaller than the thickness of the modelled material and to represent a good conductor a high conductivity value is needed where $\sigma \gg \omega \varepsilon_0 \varepsilon$. The lowest limit for valid frequency is defined by

$$\omega \gg \frac{2}{\mu_0 \mu \sigma (0.2 d)^2}$$

Both these constraints define a suitable frequency range for such a material type.

Modelling of surface roughness is also to be considered as its modification changes the surface impedance and may have a strong effect on losses. Amongst several models for surface roughness estimation, a gradient model (Gold and Helmreich, 2012) uses Maxwell equation-based approach where the gradient of the conductivity is computed using the mean square value of the surface height profile. For more complex materials, ferrite, biased ferrite, magnetized, spatially varying, plasma materials etc. complicated models are used which are not in the scope of the current research.

4.2.3. Modelling 3-d Structures

The design environment for CST is similar to several available computer aided design softwares. Having a hand full of basic shapes along with several modification tools it is possible to design complex models and import already existing models, supporting various file formats. After basic shape creation, transformation operations such as translate, scale, rotate, mirror can be applied to it. Bending, creating slots, Boolean operation on different shapes, solid to sheet and vice versa are some of the operations that come handy while creating complex scenarios.

Three right angular Aluminum sheets of side lengths 1000 mm and thickness 2 mm are aligned at right angle resulting in a corner reflector. Material properties of the used metal, Aluminum, are listed in Table 12, whereas Figure 44 previews a corner reflector resulting from the alignment of three such plates.

Table 12 Material properties of Aluminum used in the simulation

Material	Aluminum
Type	Lossy metal
Mu	1
Electric conductivity	3.56e+007 [S/m]
Rho	2700 [kg/m ³]
Thermal conductivity	237 [W/K/m]
Heat capacity	0.9 [kJ/K/kg]
Diffusivity	9.75309e-005 [m ² /s]
Young's modulus	69 [kN/mm ²]
Poisson's ratio	0.33
Thermal expansion	23 [1e-6/K]

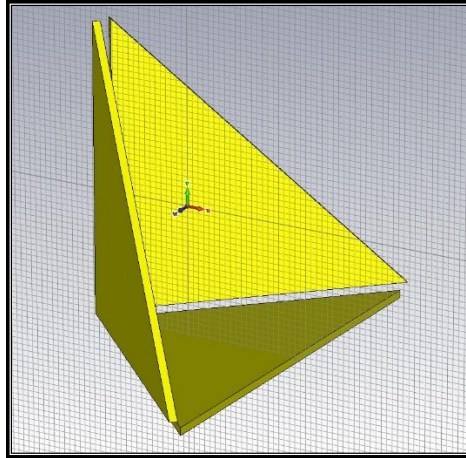


Figure 44 Trihedral reflector as seen in CST design environment

4.2.4. Boundaries and Symmetry

Due to the capability of computers to compute only the problems with a finite dimension, we need to specify the boundary conditions. Setting up these boundaries is similar as to describe the interference condition describing the behavior of EM fields. These interference conditions are discussed later (Section 4.3, Solvers Overview).

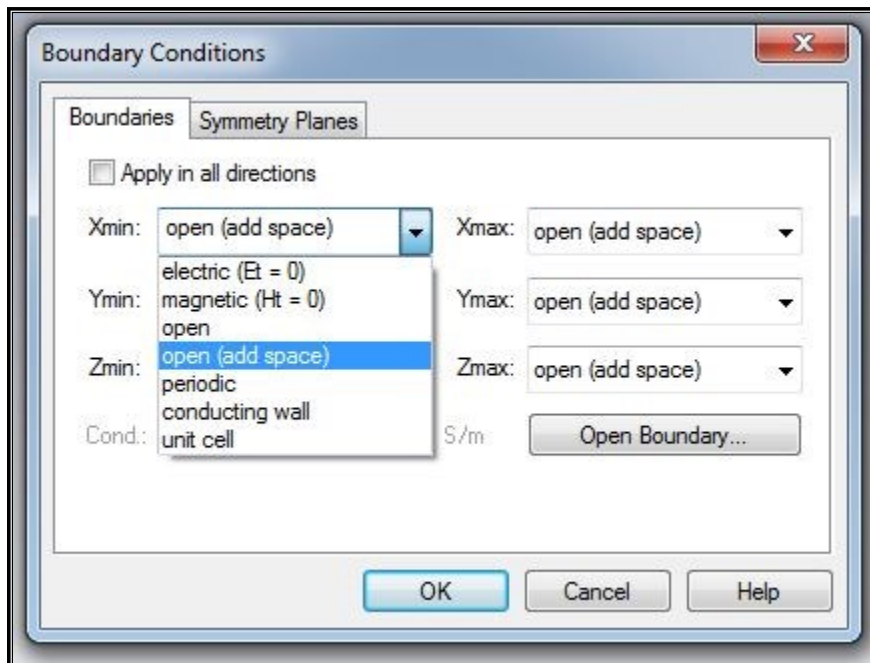


Figure 45 Boundary condition dialog box as seen in CST

Boundaries of different types can be applied to any face of the bounding box. Depending upon the frequencies, different boundary condition behave in different ways. In the current scenario, high frequency, setting a boundary as an electric boundary, acts like a perfect electric conductor (PEC). For a PEC, normal components of magnetic fluxes and

tangential components of electric fields are set to zero. Setting up a magnetic boundary behaves as a perfect magnetic conductor where normal electric fluxes and tangential magnetic fields are set to zero. Setting up an open boundary again allows two options: *Open* with perfect matched layer boundary where the open boundary is extended virtually to infinite. Incident EM waves pass through this boundary with minimal reflections. Open with 'add space', there is an extra space for far field calculations. Having minimum reflections, the perfect matched layer also absorbs additionally charged particles.

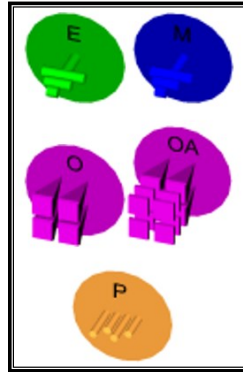


Figure 46 Symbols representing Electric, Magnetic, Open, Open with space and Periodic boundaries.

One may also set a periodic boundary where appropriate phase shifts between the boundaries makes the fields oscillate with the bounding box (Figure 45).

If the designed model is symmetric with respect to any axis, a symmetry plane can be defined. It is needed to generate the complete structure first.

Every symmetry plane in the model reduces the calculation time by a factor of two. It is recommended to specify symmetries, if they exist. There can be magnetic symmetry or electric symmetry. With a specific symmetry plane, the calculation domain is cut in half and thus reducing the calculation time by half. In Figure 47, a symmetry plane is defined across the reflector which bisects the reflector vertically. More symmetry is not obtainable for this particular structure under simulation.

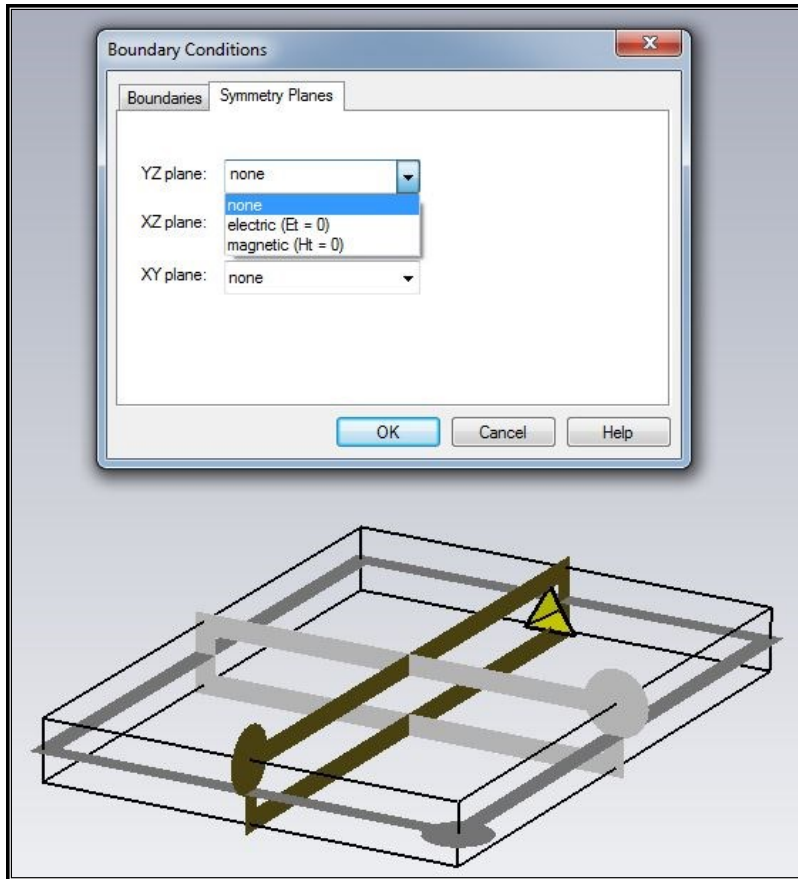


Figure 47 Defining a symmetry plane vertically across the reflector

4.2.5. Excitation Signal

A propagating wave whose wave fronts (surface having constant uniform phase) are parallel planes is called a planewave. Planewave model is widely used in physics because at a large distance, the waves emitted by any localized source are nearly planewaves when viewed over a sufficiently small area.

Planewave with different polarizations can be defined as a source-signal to the simulation. With a planewave source, an incident field can be simulated located at the boundary of the domain. Together with the use of far field monitors, the RCS of a scatter can be calculated. The incident signal is normalized to user defined input signal. The origin of the plane wave is also the reference location where the phase of the signal is calculated. With a plane wave excitation several other conditions must be fulfilled:

- Open boundary condition must exist at the direction of incidence
- There should be no other excitation ports on the same boundary
- A homogenous material should be used as a surrounding space
- The background material should not be a conducting material

Any metallic plane intersecting with the bounding box is detected as a decoupling plane. A decoupling plane is a plane that limits the plane wave excitation to the forward-facing domain. The wave is not propagated in the opposite direction when a decoupling plane is defined. Decoupling plane can also be defined manually and should only be aligned with the cartesian coordinates. Having a decoupling plane, the excitation of plane wave is restricted to the front and a reflected wave is included in the excitation. This plane also influences the RCS of the structure, RCS of this infinite PEC decoupling plane is zero thus highlighting the additional visible features in the RCS.

For linear polarization, the electric field vector is fixed, and the magnitude is equal to that of the excitation signal used. For circular polarization two orthogonal electric field vectors exists, each defining a linear polarized wave. When both are excited simultaneously with a certain time delay, it results in the circularly polarized wave. The time delay depending upon the circulation frequency and the phase shift between the two vectors is calculated. With a phase shift of +90 degrees or -90 degrees there are two possible types of circular rotations, clockwise and anticlockwise.

Other sources include far field and near field sources where the sources can also be imported in the specified format. Far field markers can be used to export a text file which can be imported in different projects. Similarly, near field sources can also be exported and imported in text formats. In principle, for a near field source, an equivalence model is applied where a closed volume is replaced by a nearfield source.

4.3. Solvers Overview

Electromagnetic modeling is the process of modeling the interaction of EM fields with physical objects and the environment. It involves using computationally efficient approximations to Maxwell's equations. Electromagnetic 'field solvers' are specialized programs that solve Maxwell's equations directly.

Solvers can be categorized into two classes of methods: (1) uses differential form of the Maxwell's equations and discretizes the entire domain in which the electromagnetic fields reside. Two approaches in this category are the finite difference (FD, the approximation of derivatives by finite differences) and finite element (FEM, subdivides a large problem into smaller, simpler parts that are called finite elements) method.

(2) are integral equation methods (FIT, finite integration technique) which instead require a discretization of only the sources of electromagnetic field. The sources exist in a smaller domain than the fields themselves, and thus the size of linear systems generated by integral equations methods is smaller than FD or FEM.

The solvers can again be subcategorized into time and frequency domain depending upon the form of Maxwell's equations used for the calculation of EM fields. Next sections discuss some of the available solvers in CST.

4.3.1. Time Domain Solver

In a time-domain solver, the development of the field is calculated at discrete time samples and locations. Basically, transmission and reflection of electromagnetic energy is calculated from the excitation source to and from the modeled structure. A single run might not be enough to calculate a wideband behavior for a wide range of frequencies. The definition of a plane wave excited by a signal (usually a chirp) is necessary to start up the simulation in our case. This time domain solver is based on FIT. FIT being a numerical method is also valid for high-frequency applications in frequency and time domain. Instead of using the differential form of Maxwell equations FIT discretizes its integral form as given below

$$\oint_{\partial A} \vec{E} \cdot d\vec{s} = - \int_A \frac{\partial \vec{B}}{\partial t} \cdot \partial \vec{A}$$

$$\oint_{\partial V} \vec{D} \cdot d\vec{A} = \int_V \rho \partial V$$

$$\oint_{\partial A} \vec{H} \cdot d\vec{s} = \int_A \left(\frac{\partial \vec{D}}{\partial t} + \vec{j} \right) \cdot \partial \vec{A}$$

$$\oint_{\partial V} \vec{B} \cdot d\vec{A} = 0$$

To proceed numerically a finite calculation domain must be defined having enclosed the problem to be solved. The mesh then divides the computational domain into small grid cells. Two orthogonal to each other hexahedral grids (Figure 48) are set onto which the spatially discretized Maxwell's equations are performed. To the first primary grid, Electric grid voltages \mathbf{e} and magnetic face fluxes \mathbf{b} are allocated. On the secondary grid, magnetic grid voltages \mathbf{h} and dielectric face fluxes \mathbf{d} are allocated.

For each facet, Maxwell's equations are formulated. Applying Faraday's law, the closed integral is written as a sum of four grid voltages and this introduces no additional errors. Similarly, the cell facet is represented as the time derivative of magnetic flux. This procedure is repeated for all facets. Topological matrix \mathbf{C} is introduced as an equivalent of curl operator. On the dual secondary grid Amperes law is applied with corresponding dual discrete curl operator $\tilde{\mathbf{C}}$. Moreover, for the discretization of divergence, discrete divergence operators \mathbf{S} and $\tilde{\mathbf{S}}$ are introduced. Thus, completing a discretized set of Maxwell equations for the grid:

$$\mathbf{C}\mathbf{e} = -\frac{d}{dt}\mathbf{b}$$

$$\tilde{\mathbf{C}}\mathbf{h} = \frac{d}{dt}\mathbf{d} + \mathbf{j}$$

$$\tilde{S}d = q$$

$$Sb = 0$$

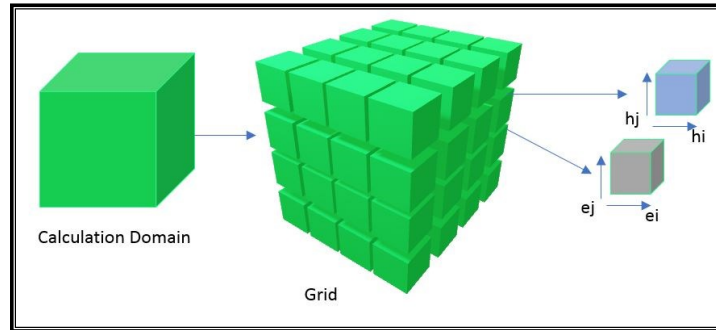


Figure 48 Calculation domain divided into dual grid cells

The only introduced numerical inaccuracy is due to the material relations. In defining these relations, the approximated integral values are used over the cell area and edges of the grid. The accuracy is moreover dependent upon the spatial resolution of the grid discussed later (Section 4.5.1). This finalizes the EM field setup of grid space which is discrete. The FIT is also applicable on general irregular shaped meshes but such mesh shape was not a scope of this project. Perfect Boundary Approximation can also be applied to FIT for better results.

During the calculations, the grid is upgraded in a leapfrog scheme manner (Figure 49) where both types of unknown variables electric voltage and magnetic fluxes are alternately located in time. The time derivatives are substituted by central differences which gives an update formulation for the lossless case. To calculate the magnetic flux at the next time step, the value of magnetic flux at the previous time step and the electric voltage at the half step before is used.

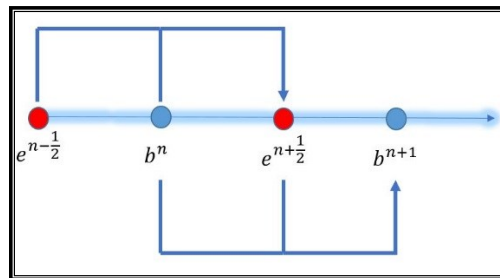


Figure 49 Leapfrog grid voltage calculation

4.3.2. Frequency Domain Solver

Phasors are used to describe fields when using a frequency domain solver instead of time domain solver. The Maxwell's equations are transformed to frequency domain equivalent where the transient fields are obtained by time factor multiplication of the phasors. For a broadband coverage, every frequency sample needs to be solved in the

equation system. However, sweeping techniques may be used to obtain a complete broadband spectrum using relatively lower frequency samples. This solver might be best suited for applications where individual frequency analysis is required.

4.3.3. Asymptotic Solver

Shooting and bouncing rays (SBR) was a method developed for computation of RCS of objects (Lee, 1989). SBR uses geometrical optics (GO, describes light propagation in terms of rays) for computing equivalent currents on structures surfaces. The scattered field is thereafter computed by integrating these currents using physical optics (PO), by the Kirchhoff's diffraction formula.

In CST, Asymptotic solver is based on SBR technique. Objects which are electrically very large and cannot be handled by other solvers can be simulated using this solver. However, there is a limitation of using only open boundary and the medium of travel should be vacuum only for this solver. This does not affect our case where the medium of propagation is a vacuum, and we are having boundaries open. Using monostatic scattering in this solver the rays are observed at the same angle as that of the excitation. Having wide areas of application for this solver here it is used in the calculation of far field, visualization of the incident and reflected rays and hotspots. At hotspots, the path ray analysis is combined with the RCS to identify which parts of the structure are producing highest reflection contributions. Certain reflections order can be selected, and others can be neglected as per requirement. Hotspots are actually RCS contributions that are localized having positive values. Each ray's RCS contribution is mapped onto a 2-d image of the structure. The result may also be filtered by a window function. By setting up an angular range, observation angles larger than this range will not contribute to the hotspot image. Moreover, using this weighting function specular contributions can be weighted as compared to others.

4.4. SAR Processing

Processing of the SAR data is a complicated process with advanced mathematical techniques and high computational costs. Several algorithms have been developed in this regard fulfilling different requirements. This section starts with a short introduction to the actual SAR processing algorithm deployed by TSX. Later, a simplified version self of algorithm is explained which is programmed solely for simulation purpose from scratch. At the last, single and multiple objects are simulated using the developed SAR processor. Each step of the simulation process is elaborated with results.

4.4.1. Complex TSX's Focusing Algorithm

The fact that TSX antenna is highly steerable allows us very different data acquisition modes. All of these modes are than processed by an Extended chirp scaling algorithm (Moreira, Mittermayer and Scheiber, 1996). The processing is carried out at the ground

segment in TMSP (See section 3.1.1). These modes include Strip-map mode, Scan-SAR mode, and spotlight mode. The signal processing common to these modes is implemented once as seen in the Figure 50, hence reducing the software costs for testing, documenting and implementation.

Consecutive blocks of azimuth data are processed repetitively. In the strip map mode, the consecutive azimuth data received is overlapped by at least one synthetic aperture. In the Spotlight mode, sub apertures are formed so as the PRF is not exceeded. For the Scan-SAR mode each burst of data is handled individually.

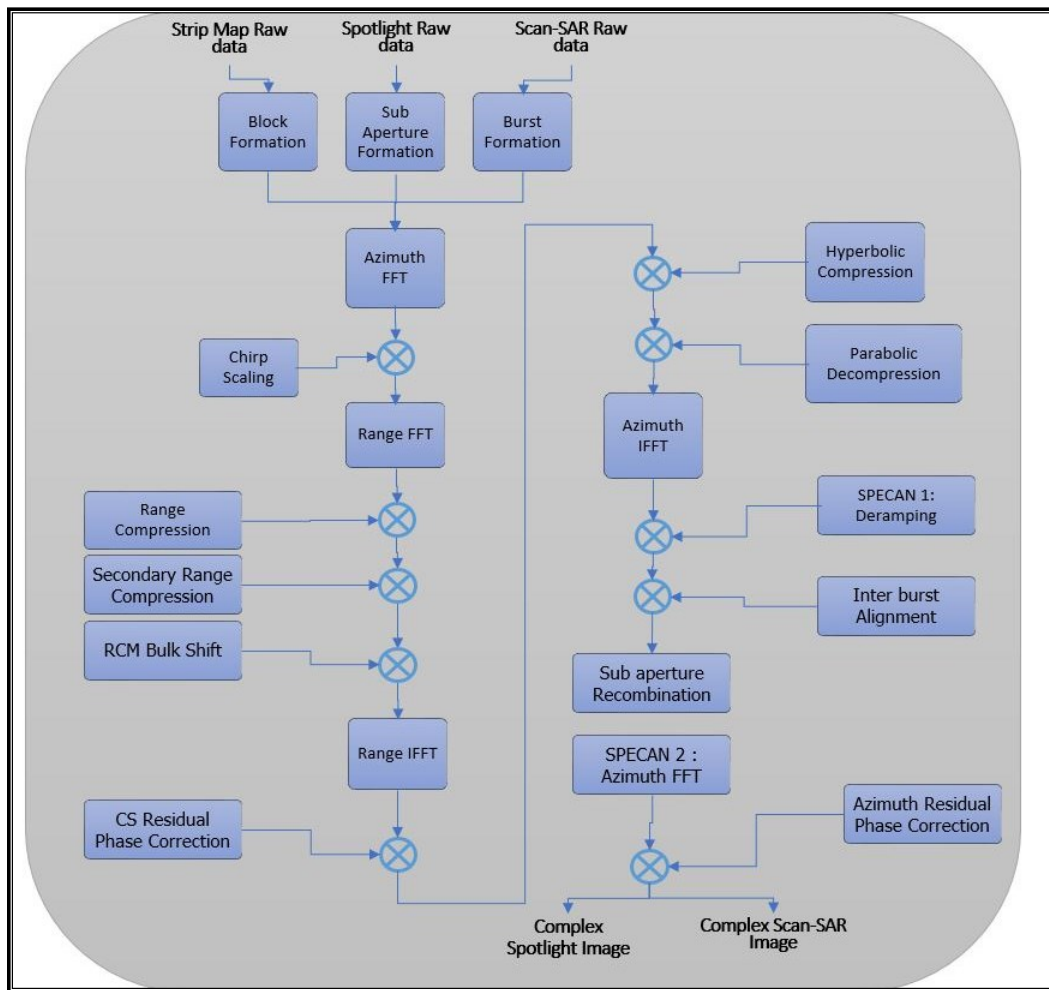


Figure 50 Processing steps in TSX image focusing performed at the ground station (Breit, H. et al 2004)

The range processing begins after the chirp scaling in the range Doppler domain where range compression, secondary range compression and then range cell migration correction takes place. Chirp scaling residual phase correction is applied which completes the range compression. Focusing in the azimuth is common for the three modes where correlation with an azimuth reference function is performed. The azimuth phase history

is modelled for complete range in form of blocks. At this point inverse Fourier transform results in the single look complex image (SSC) for strip map mode. For Scan-SAR, it is more efficient to apply Specan algorithm, where azimuth scaling makes the results highly accurate. Hyperbolic compression and parabolic decompression are applied to achieve this azimuth scaling. For better understanding of complex mathematical processing involved in the Spotlight and Scan-Sar algorithms one may refer to the literature (Mittermayer *et al.*, 1999), (Mittermayer, Lord and Borner, 2003). These resulting images are in single look complex images of different resolutions and are ready for further interferometry products and other SAR applications.

4.4.2. Simplified SAR Range Doppler Algorithm for Simulation

Basic Range Doppler Algorithm (RDA) (Figure 51) suited for the processing of relatively low squint angles is used, discussed in detail (Cumming and Wong, 2005). Range compression can be performed with fast convolution when the data is in azimuth time domain. A range Fast Fourier Transform (FFT) is performed followed by a range matched filter multiplication and then the inverse transform is applied. The fact that current RAW data is not very large having convolution in time domain is also not very time consuming and is preferred to avoid FFT artifacts.

Azimuth FFT transforms the data into range doppler domain, range cell migration which is range time and azimuth frequency dependent is performed in range-doppler domain. The targets having same slant range but separated in azimuth time all have same doppler history. By virtue of Fourier transform shift theorem the energy of all these targets will be positioned exactly in the same frequency samples, with each target having a different linear phase component. In short, targets having same range of closet approach transforms into one trajectory in RD domain. This property is exploited in RDA to gain computing efficiency.

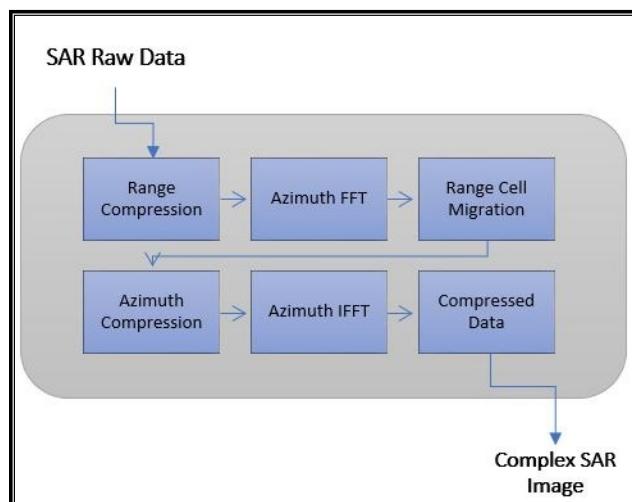


Figure 51 Simplified SAR processing for the simulated data implementing the Range Doppler Algorithm

RCMC is performed in range doppler domain which straightens out the curved trajectories that now run parallel to the azimuth frequency axis. There are two ways to implement RCMC, it can be performed by range interpolation option in RD domain. The amount of RCM to be corrected is given by

$$\nabla R(f_n) = \frac{\lambda^2 R_0 f_n^2}{8V_r^2}$$

Where V_r, R_0 and f_n are radar velocity, closed range of approach and azimuth velocity, respectively.

Another implementation involves the assumption that RCM in range invariant over a finite range region. In such case RCMC is implemented using FFT, a linear phase multiplication, and then inverse transform. The phase multiplier for a given frequency is given by

$$G_{rcmc} = \exp\left(j\frac{4\pi\nabla R(f_n)}{c}\right)$$

The correction amount is held constant for small range blocks.

4.4.3. Single Target Simulation (Sphere)

A target of very small dimension that possibly can be categorized as a zero-dimension object is called a point target. In electromagnetics, by definition, a point target gives uniform scattering when EM waves are incident onto it. The scattering of energy is isotropic, i.e. the intensity of reflected energy radiated is same in all directions. In the real world a target needs to fulfil some criteria for so that EM-object interaction is possible. The scattering of wave by an object is, wavelength and particle size dependent. So, a particle of zero-dimension does not exist practically. To measure the reflected wave intensity, a surface having zero cross section area will not be scattering any field. An object with similar properties as that of a point target is a uniform sphere. The SAR response of a sphere is a point target in the SAR image.

This section describes the use of CST to setup an object and simulate SAR processing of this object. To demonstrate the usability and validity of CST for simulating SAR, a simple geometric sphere is used. A simple sphere might be very basic, but it is relevant and meaningful in the apprehension of multiple objects. Moreover, the usability of CST to simulate SAR is verified.

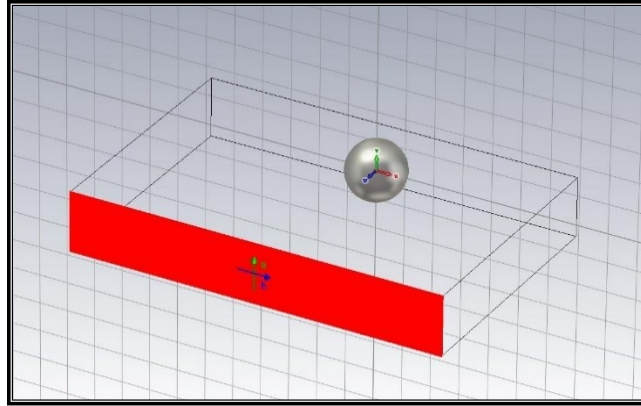


Figure 52 Plane wave excited by chirp, incident on a single sphere

Plane wave is defined as an excitation signal, where the simulation amplitude in V/m (volts per meter). Instead of using default signal to excite the plane wave, a chirp signal (Figure 53, left) is imported to CST. The chirp is filtered by a Hamming window filter or multiplied by a cosine function, which makes it amplitude gradually increasing and then decreasing hence suppressing sidelobes. Such a gradual change in the signal almost completely removes noise and artifacts that are generated by sudden changes.

The limit for range axis is dependent on number of samples in the transmitted chirp, which in turn is dependent on the sampling frequency of the chirp signal. The limit for azimuth axis is dependent on the number of farfield probes placed in front of the simulated object which serves to measure the reflected field at that location. Each reflected signal received by farfield probe serves as one row in the 2-d raw data matrix. The transmitted and received signal for a single pulse is seen in Figure 53. This signal is measured by one farfield probe which was placed directly opposite to the central axis of the sphere. Matched filtering for this single pulse is seen in Figure 54. This matched filtering is the range compression as discussed earlier (Section 2.3.5). When viewed by SAR principle, these farfield probes, fulfill two SAR criteria: first, this results in the pulse repetition frequency, where each received signal is treated as a single pulse. Secondly, having all these probes located adjacent to each other fulfills the criteria for the formation of the synthetic aperture, which is essential in SAR for image focusing. Depending on the position, each probe receives the signal with a delay compared to the previous adjacent probe. This delay accounts for the phase change which depends on the distance between the two probes. Having all these phases aligned, the SAR algorithm focuses the scattered EM energy to a point and hence achieving high resolution.

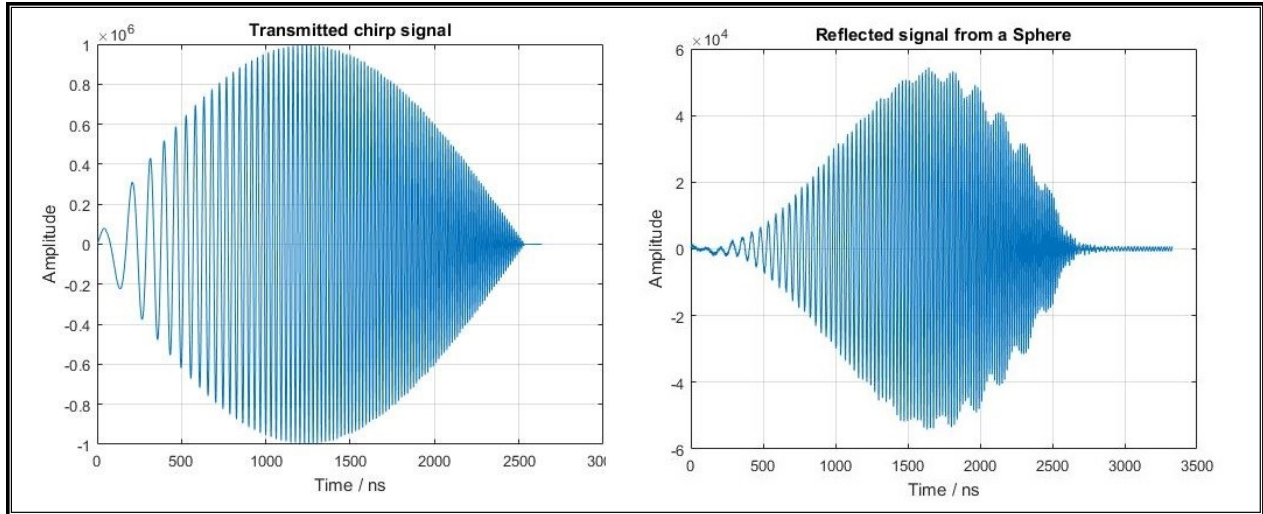


Figure 53 (Left) Transmitted chirp signal. (Right) Received signal after being reflected from sphere

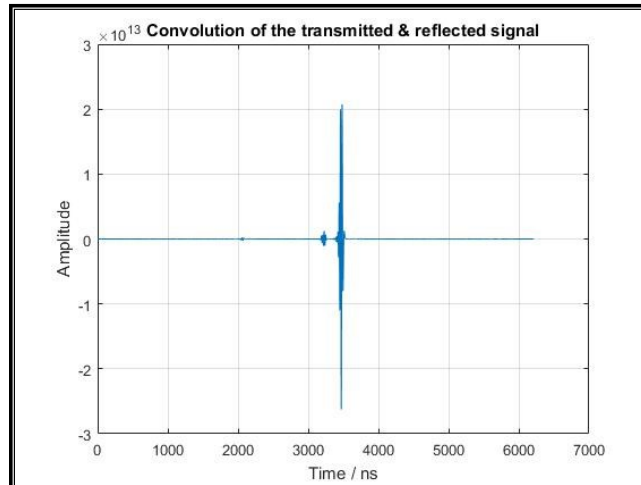


Figure 54 Range compression for a single pulse reflected by a sphere

In the current example, a simple sphere excited by a 50 ns chirp signal (Figure 52). The sampling rate of the chirp and the sampling rate of electric field plays a significant role in the formation of the resultant SAR image. Fulfilling more than what is required for the Nyquist sampling criteria, MATLAB auto selects 3000 samples for the transmitted chirp and similar number for the reflected wave (Figure 53, right).

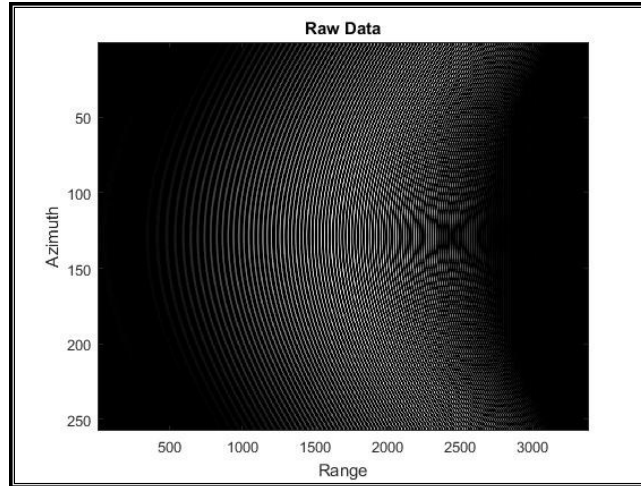


Figure 55 Unprocessed RAW data as collected from a single sphere

These 3000 samples account for the range axis as seen in the RAW data (Figure 55). The azimuth samples as mentioned before are dependent on the E-field probes responsible for collecting the reflected waves at their respective positions. Having 250 probes for collecting samples restrains the limits for the y-axis in the RAW data figure. Here we might be introducing an artifact where the resulting SAR image has unequal X and Y dimensions, hence resulting in unequal range and azimuth resolutions. Having more probes results in a larger calculation domain and hence larger memory requirements. Nonetheless, for the current setup of limited number of objects being simulated, the current number of farfield probes does not affect the results. Zero padding possibly could be done in the azimuth axis resulting in an image with similar dimensions in range and azimuth.

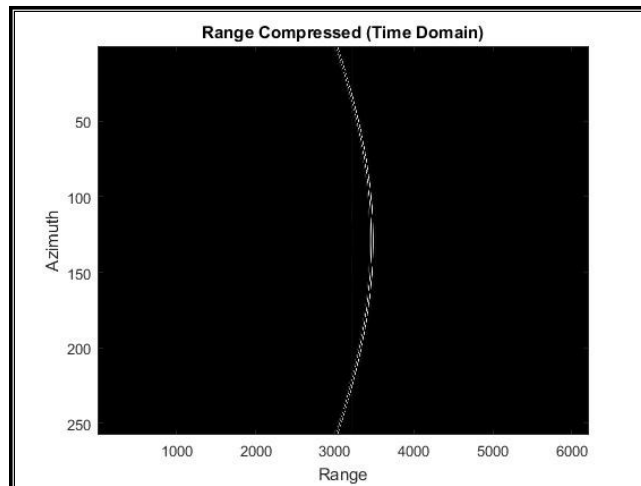


Figure 56 Raw data compressed in the range direction via convolution, range cell migration curve is evident for a single sphere

Time domain convolution of the received and transmitted signal (3000 samples each) when performed results in the twofold increase of the range axis dimensions.

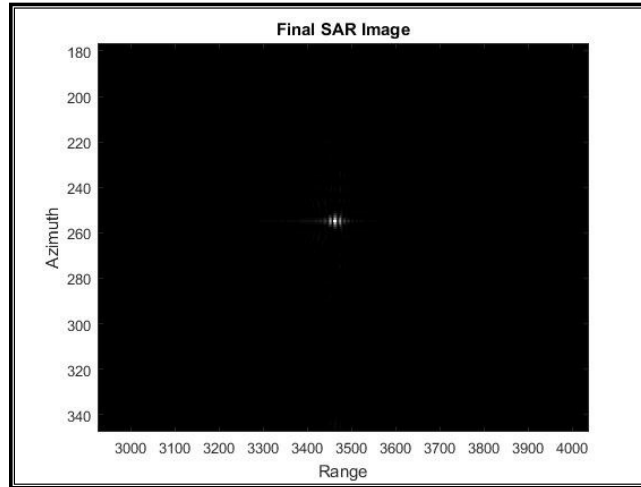


Figure 57 Final processed SAR image for single sphere (magnified)

Range cell migration correction, which is performed in the time domain for each pixel in the range compressed image. For a single object, range cell migration curve detection is relatively easier with only one curve corresponding to the object (Figure 56).

For multiple objects it is a complicated procedure. For each pixel, range cell migration curve is detected which depends on the position of pixel in the image. The scattered energy spread out in this curve is compressed via matched filtering and that particular pixel is updated. This computationally expensive calculation is done for all the pixels for the 2-d range compressed image, hence resulting in an azimuth compressed final SAR image (Figure 57).

4.4.4. Single Target Simulation (Corner Reflector)

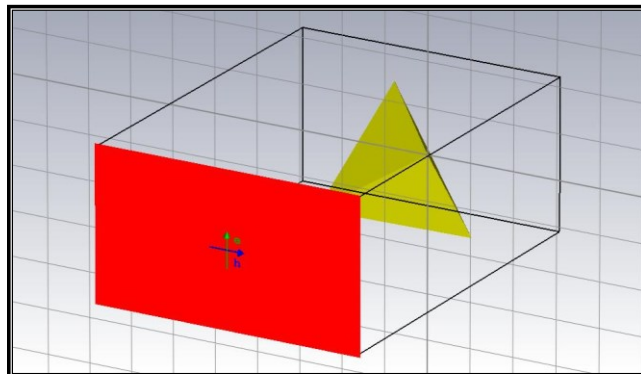


Figure 58 Plane wave excited by chirp, incident on a modelled corner reflector

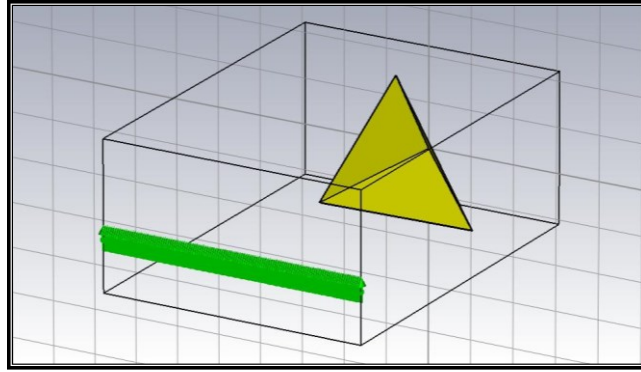


Figure 59 Far field probes at the boundary to receive the scattered EM signal

Another simple corner reflector was modelled and simulated in a similar setup. As seen in the Figure 59, far field probes (green markers) are placed at a distance large enough where transmitted and reflected field can travel back and forth without interfering with each other.

The transmitted and received signal for a single pulse is seen in Figure 60. This signal is measured by one farfield probe which was placed directly opposite to the central axis of the CR. Matched filtering for this single pulse is seen in Figure 61.

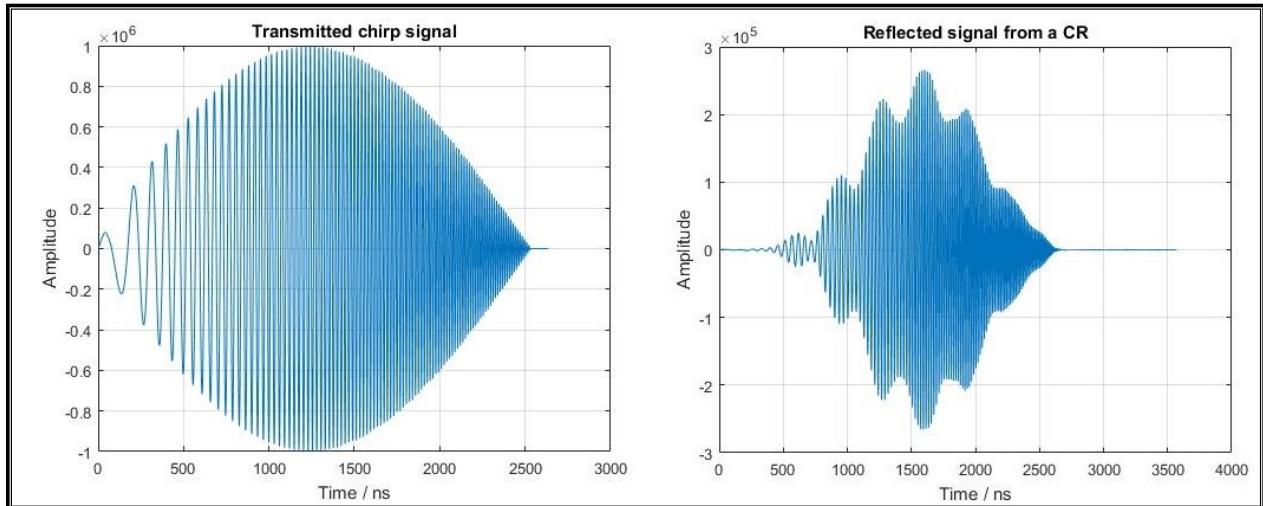


Figure 60 (Left) Transmitted chirp signal. (Right) Received signal after being reflected from CR

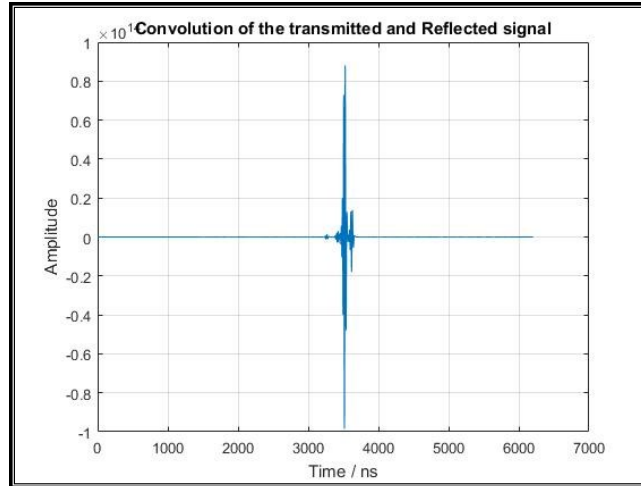


Figure 61 Range compression for a single pulse reflected by a CR

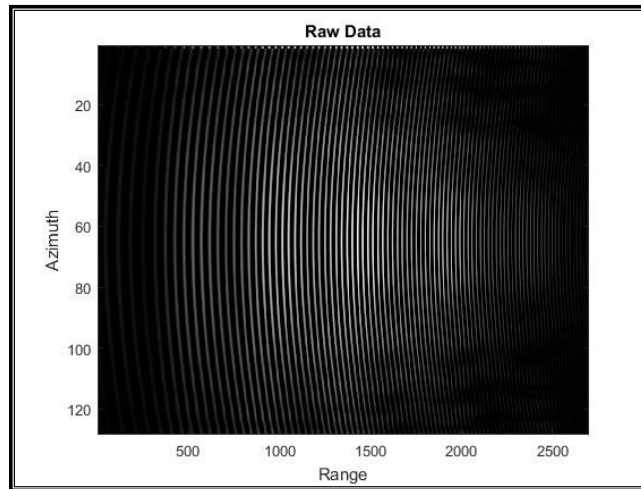


Figure 62 Unprocessed RAW data as collected from a CR

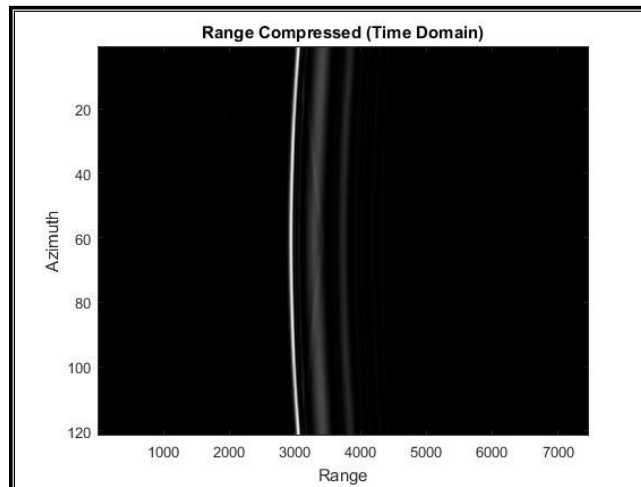


Figure 63 Raw data compressed in the range direction via convolution

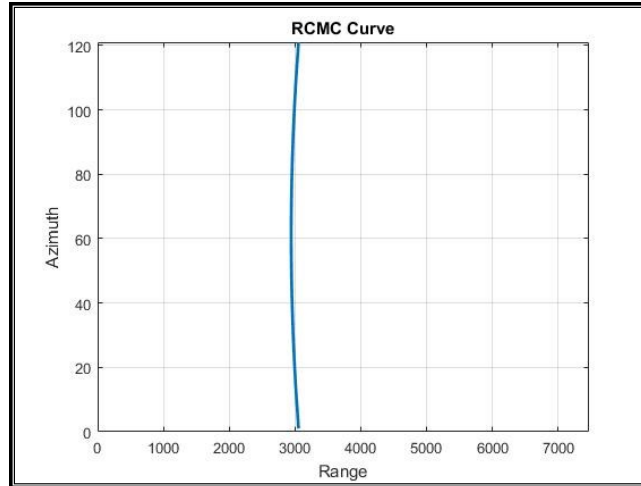


Figure 64 Range Cell Migration curve, because of SAR acquisition geometry

Range cell migration, also mentioned previously is the signal energy from a single point target follows a hyperbolic trajectory in the two-dimensional SAR data is visible in the Figure 64. This needs to be aligned within a single range-bin. Range-bin depends on the range at which the point target is in center of the antenna beam. After that the signal energy in the azimuth direction is compressed resulting in the final SAR image seen in Figure 66.

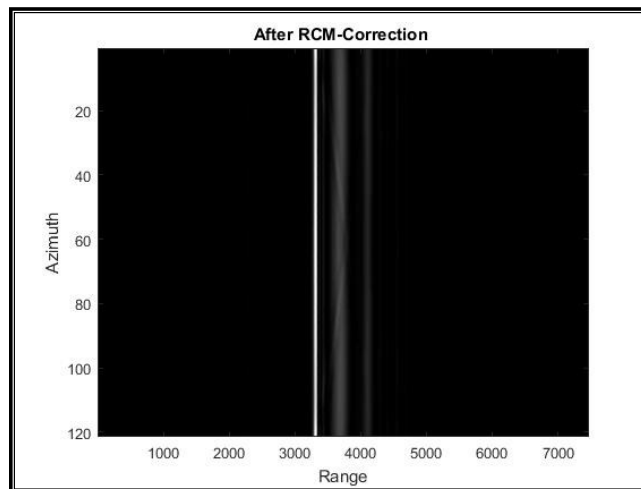


Figure 65 Corrected Range cell migration curve

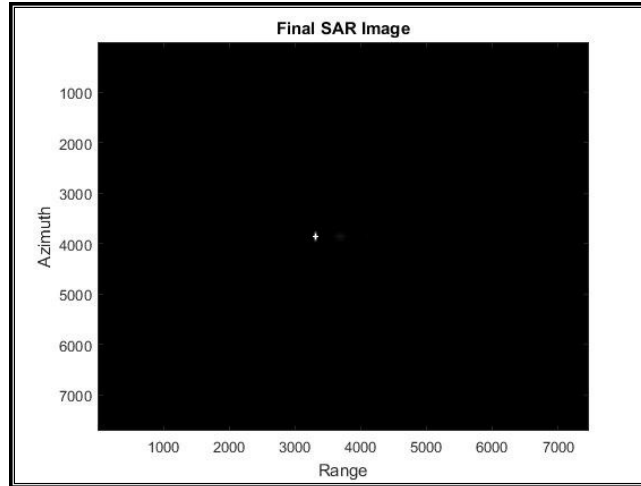


Figure 66 Final processed SAR image

4.4.5. Multiple Targets Simulation

In order to extend the simulation for multiple targets, three similar equidistant spheres are placed at a constant range (Figure 67). With a chirp incident, reflected field is collected to form a 2-d raw data matrix (Figure 68).

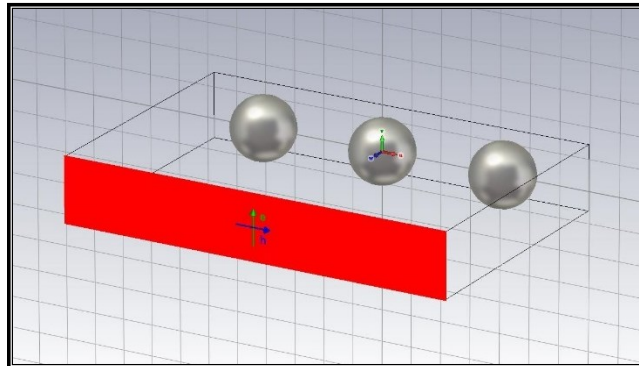


Figure 67 Plane wave excited by chirp, incident on three modelled spheres at same range

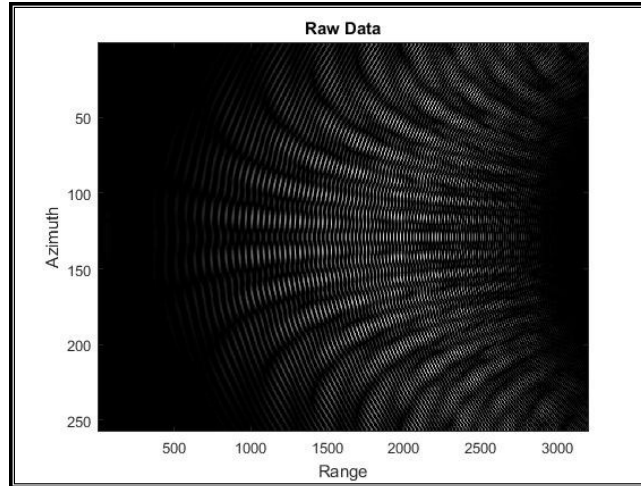


Figure 68 Unprocessed raw data as collected from three equidistant spheres

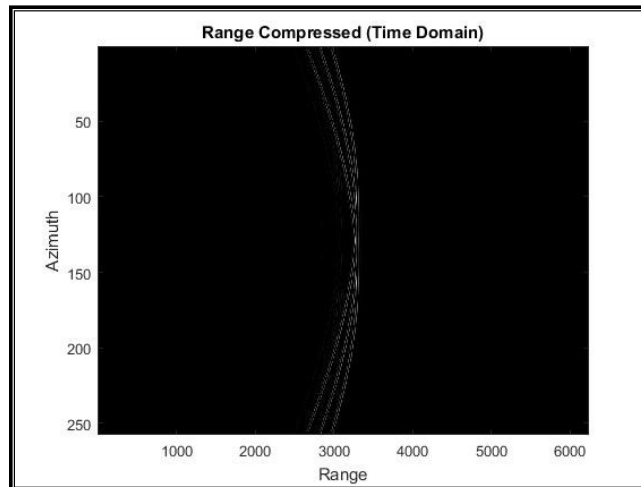


Figure 69 Raw data compressed in the range direction via convolution, three range cell migration curves are evident each for a sphere

Three distinct spheres create three range cell migration curves seen in the Figure 69. After the last two steps the final SAR image is generated. Three strong point target responses are seen in the Figure 70 which are equidistant from each other and at a constant range distance.

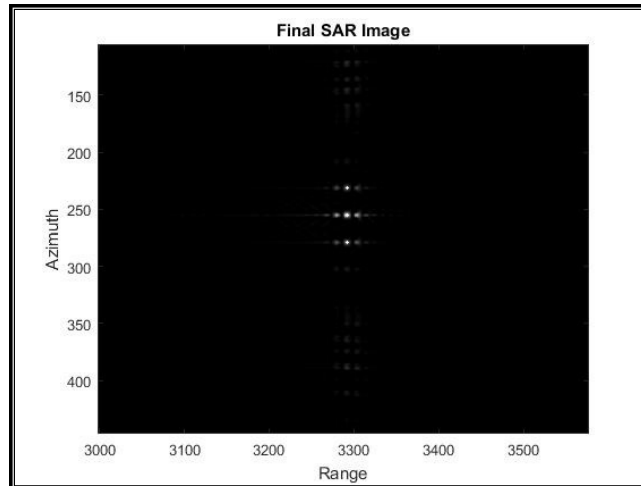


Figure 70 Final processed SAR image for three spheres (magnified)

Having a bigger simulation domain results in a problem size which is unable to fit into a computer's memory. This problem is elaborated in the next section where size of domain with respect to the memory are discussed.

4.5. Limitations of Time and Size

This section particularizes the computational requirements of the CST software while simulating any object. The complexity increases with the size of the domain which required more commutation time and resources. At the last, gridding or meshing phenomenon of the simulator is explained with the possible sources of errors and their effects on the simulation accuracy.

4.5.1. Understanding the MESH

Understanding the meshing in any electromagnetic solver is important to achieve the desired results. The accuracy of the simulation results is directly proportional to the discretizing of the model being simulated. The results converge completely when the mesh become continuous or is only differential, so very fine mesh results in a very accurate simulation. Having a finer mesh means a large number of cells and hence a large number of unknown coefficients to be solved and therefore extending the need for memory and time. Creating finer mesh cells in 'time domain solver' is relatively less memory demanding (compared to other solvers) and is linearly saleable, meaning that increasing mesh/cells increases the computation time in similar proportions. The hexahedral mesh we talked about previously is discretized by a rectangular cube of variable size. Each mesh cell is a volumetric space where magnetic and electric fields are computed. Having more mesh cells will result in a better measurement of the gradient field. A good compromise between speed and accuracy is required which is defined by a balanced mesh. It is important to know what constitutes a good mesh. A simulation is started in the time domain when a plane wave signal, typically a Gaussian

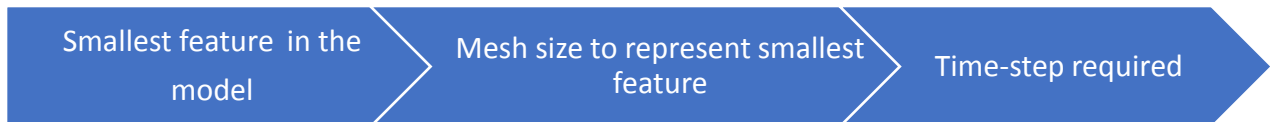
pulse or a chirp is emitted. The width of the signal is managed and adjusted depending upon the bandwidth specified. After the excitation, this signal propagates through the volume. The energy is decayed as it propagates due to loss mechanisms such as propagation loss, lossy material, absorption etc. Until the energy has not reached the user-defined minimum level the simulation will continue. Another important factor here is the speed with which the signal propagates in the bounded domain. The faster the signal propagates, the shorter the simulation time. The speed at which the signal propagates within the bounding box is defined by time step. After every iteration, the fields are advanced by one-time step. However, this value cannot be chosen arbitrarily, a large value may not perform well as the step must be small enough to satisfy the Courant stability condition as follows (CST, 2010)

$$\Delta t_{max} \leq \frac{1}{u_{max}} \left(\frac{1}{\Delta x^2} + \frac{1}{\Delta y^2} + \frac{1}{\Delta z^2} \right)^{-1/2}$$

where the phase velocity of the wave is defined by u_{max} . For a uniform cubical mesh, the step-size is governed by the mesh size. Having all lengths equal to the above equation results in

$$\Delta t_{max} \leq \frac{\Delta l}{\sqrt{3}}$$

revealing that for a fine mesh the time-step also needs to be small. To speed up the simulation the mesh cells needs to be large. The limiting factor for the smallest mesh cell is the need to represent small areas in the simulation where we want the fields to be finely sampled. Hence minimum feature size governs the smallest mesh size which then governs the smallest step-size.



Mesh cell size dependency

One may infer from the previous discussion that the larger the mesh cell size the faster the speed, but there is also a limitation on largest possible cell size for a given frequency. The mesh cell size cannot be increased arbitrarily. The numerical dispersion may occur as different frequency components propagate at a slightly different frequency in the mesh which is due to space discretization. To ensure that the mesh behaves in a similar way for all the frequency components the shortest wavelength must be sampled at at least ten cells per wavelength. So, the highest frequency, i.e. the shortest wavelength governs the largest possible cell size.

The total number of mesh cells is another quantity that governs time and accuracy, which can also not be controlled directly. It depends on the size of the computational

volume. Electrically large objects are again restrained by the computational and memory requirements. To summarize, higher frequency will increase the requirement of total mesh cells and so will the electrical size of the object being simulated. To get an idea of numbers the exact mesh memory size required per mesh cell cannot be said with certainty as there are many other memory-consuming factors such as boundary conditions, material, field monitors etc. As a rough estimate, around 10 million hexahedral cells require 1-Gb memory for closed boundaries and simple materials being simulated. To simulate a unity cubic volume at 10Ghz (0.03 m) frequency with the recommended requirement of 10 cells per wavelength will require around 40 million mesh cells and hence require 4-Gb of computational memory.

4.5.2. Accounting for Error Sources

Discretization usually introduces errors, as the model may not be identical to the actual structure or errors may occur in numerical simulation. Dense space sampling is required to minimize grid discretization error. Many of following errors are negligible but it is important to be aware of them at the time of simulation.

- The geometric dimensional error may have been neglected, this can be avoided by careful comparison with the original model.
- Material properties may not be precise enough or not exactly known, as they are also frequency dependent. Using one value for a range of frequencies may introduce error in the accuracy.
- Excitation signal may differ from the real signal, moreover, the discrete ports are not perfectly matched.
- Environmental variables, temperatures, nearfield and far-field distances are not incorporated accordingly.
- Truncation error may occur if time signals are not decayed completely or if the simulation time is smaller than the stability time where minimum energy criteria are met.
- Another type of geometrical error is when the mesh model deviates from the CAD structure. Usually, staircase approximation is used to model rounded and curved surfaces, which can again be reduced with the use of a finer mesh.
- Minors errors may occur due to mismatch at the boundaries and interpolating the fields at locations where grid does not exist and hence there are no calculated EM field values.

Chapter 5: Shooting and Bouncing Rays for Large Objects SAR Simulation

In the previous chapter, a new technique to simulate SAR was introduced but it was limited to simulate small objects only. It was also discussed how the computational size grows exponentially with an increase in the simulation's domain size. In this chapter, a previously developed raytracing technique is used to simulate bigger sized objects and several urban buildings. This chapter also gives a brief introduction to the ray-tracing techniques and its setup to simulate SAR. A short introduction is given about RaySAR (Auer, Hinz and Bamler, 2010) which is a modified version of POV-ray (a ray-tracing package, talked later in the text). Some modeling details are also elaborated using another open source CAD tool named 'Blender'.

Various types of buildings are modeled in detail and then SAR data is simulated for ascending and descending orbits. Dome-like structures are also modeled and simulated, and the results are analyzed having reference TSX data forehand. The selection of buildings to be simulated was based on the availability of TSX data and the ease of structure modeling.

5.1. POV-Ray and its Modelling Environment

Raytracing is an image synthesis technique, generally used in computer graphics, where 'emission of radiation' based algorithm is used for the occlusion determination of three-dimensional objects from a point in space. The path of light is traversed and the effects it encounters during the travel are calculated, after that virtual objects are simulated. These effects include reflection, scattering, dispersion, and refraction. It is one of the methods of projection where a three-dimensional spatial object is reduced to a two-dimensional object to create an image of it.

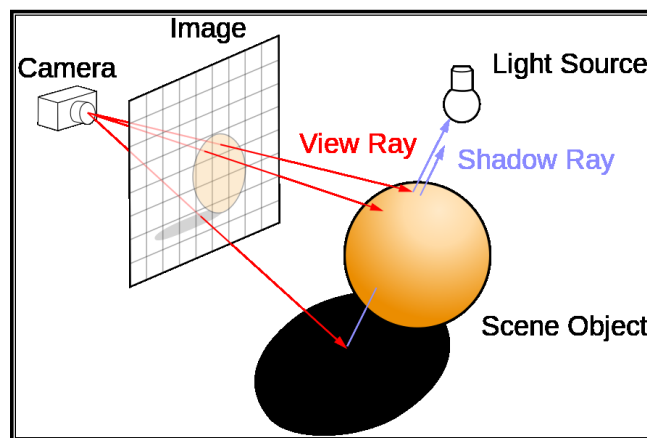


Figure 71 Overview of a Ray-tracer with a projection of 3-d object onto a 2-d plane (Ray tracing (graphics), 2008)

Forming an image of real-life object involves the projection of a 3-d scene onto a 2-d surface. In the optical photography, similar to that of a human eye, objects at a distance appear smaller than objects close-by, this is known as perspective view or perspective projection. In perspective projection, parallel orthogonal lines converge to a single point when extended to infinity, to create an illusion of depth.

POV-ray (persistence of vision), is a free and open source ray-tracing software which renders images from the text-based scenes. Linear perspective is the standard image viewing method in POV-ray. This requires a projection center (eye, or the lens of the camera) and an image plane (2-d plane, like a plane of the film or the sensor in optical photography). The image of a point in space is obtained by connecting the point with the eye (the connecting line is called the line of sight) and cutting the line of sight with the image plane (Figure 71). With straight lines, the image is not quite proportionate (the centers of the image do not change), whereas far points are mapped to finite points. The image plane can also be a cylinder, then we get the cylindrical perspective, where straight lines map into sinusoids.

In simple terms, for all the pixels of the image plane, visual rays are laid (through the eye point, a fixable point in space, or parallel to a direction). These rays may or may not hit the objects. In the case of impact, they receive a color value from the object which is then assigned to the pixel in the image plane. If the object is specular, the visual ray is reflected and may possibly hit another object. If the object is refractive, it is refracted. This is how color and brightness values are determined for each pixel of the image plane. This process can be followed for each pixel when building a ray-tracing image in POV-Ray. The image plane is processed line by line from top to bottom, which requires a certain amount of time.

The determination of the color and brightness value on a surface is also not very easy, different algorithms (not in the scope of this text) are also developed in this regard.

POV-ray uses a left-handed coordinate system where x-axis on the screen is to the right, y-axis up, and z-axis into the screen. Normally, we use the right-handed coordinate system with horizontally lying x and y-axes, which is mirror-inverted, therefore, the coordinates need to be assigned carefully.

Modeling (See Appendix) is performed in a text editor and the objects are not visually displayed until they are rendered, however, there are several other interfaces available for importing models of high details.

5.2. Introduction to RaySAR

RaySAR (Auer et al., 2010), mentioned previously, is based on the POV-Ray raytracing technique. Modifications were made to the open source ray-tracer called POV-Ray. For the urban areas, the aim was to generate very high-resolution SAR images. With the

main goal of identifying the persistent scatters, random scattering was not incorporated and hence there was no speckle effect in the simulated images. Different case studies were made for a better understanding of SAR images acquired by TSX and some unobvious SAR effects were explained. Further details are to be discussed later in the text as this simulator was also used in the current research.

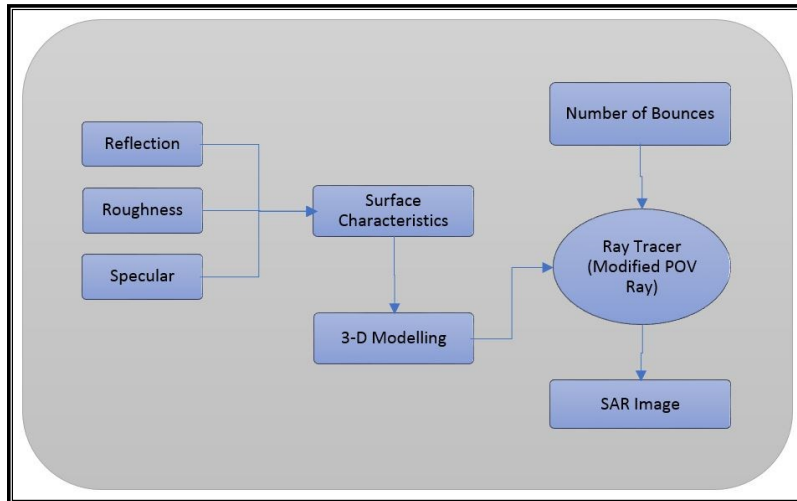


Figure 72 Overview Ray-Sar: a direct image simulator

Figure 72 gives an overview for the steps involved from modeling to final SAR image using RaySAR.

5.2.1. SAR Adaptation in RaySAR

Radar images involve a different projection compared to that of optical images. The major difference between the two imaging geometries is that microwave sensors determine distances while optical sensors measure viewing angles. In a SAR image, all the projection lines are orthogonal to the projection plane. So, to simulate a SAR system, a camera, a signal source emitting parallel light, and an orthographic projection in azimuth and elevation axis are used. The data is not gathered along a synthetic aperture and the focusing is performed directly. This step of not synthesizing a synthetic aperture is discussed in detail in Chapter 4.1.2, where a comparison is drawn between raw-image simulators and direct-image simulators (Figure 42). Focusing in azimuth is also not required as the resolution is already at a pixel level. For such a system the pixels are defined by the number of rays and the distance between them (ray density). This enables to separate the contribution from the same pixel in the elevation direction. Moreover, there is no PRF required for such simulation and the simulation is also speckle free. After the simulation, the number of bounces can be separated into different levels and hence studying each level for a specific bounce count. Having the intensity distribution in the elevation it is also possible to differentiate scatterers whose reflections are mapped into the same resolution cell.

From a central perspective, in the elevation direction, the orthogonal projection is a good approximation for SAR geometry. This approximation is also valid as the incident wave front is assumed to be flat in the farfield for an object. Having an orthographic projection, the simulation is distance independent between the object and the sensor. The downside of such orthographic projection is that this approximation may not be valid for large scenes as the incidence angle is assumed to be constant over the entire scene. This may also induce mapping errors when a large simulated scene is mapped to a simulated object. An important step to realize the virtual SAR system is that the camera and the signal source are placed at the same location, this is exactly how a real SAR system works. The SAR axis corresponds to RaySAR axis such that the azimuth and the elevation axis are the horizontal and vertical axis, whereas the range axis is perpendicular to the plane.

5.2.2. Reflection Bounce Count

After the raytracing is done for the modeled scene, all the intersection points are detected for the objects present in the scene. The resulting output information are the number of bounce levels, intensity values, and the coordinates of the scene in the slant range and azimuth axis. After assigning the measured intensity levels with respect to range and azimuth coordinates, the reflectivity map for the modeled scene is generated. As mentioned before, the receiver and the sensor are at the same location and are also having the same viewing direction. The resolution of the image depends on the number of sampling rays to illuminate the scene.

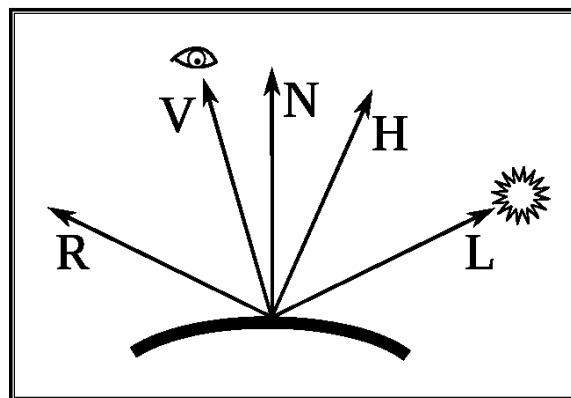


Figure 73 Vectors for calculating reflection and related effects

Different vectors involved in the process of light object interaction are shown in Figure 73, vector L is the direction vector from the point on the surface toward light source (same as the direction of viewer in SAR simulation case). N is the normal at this point on the surface. R is the direction that a specularly reflected ray of light would take from this point on the surface, and V is the direction pointing towards the viewer.

The reflection models (used in RaySAR) are optimal at the frequency of light, for better radiometric quality more appropriate models could be adapted where the wavelength is close to the one used in SAR.

The important step in the simulation is the measurement of the intensity values, where standard diffuse and specular reflection models are used, and the intensities are calculated as follows:

The diffuse intensity is given as

$$I_d = k_d \cdot I \cdot (\vec{N} \cdot \vec{L})^b$$

where the intensity of light I is scaled by the diffuse reflection constant k_d . $\vec{N} \cdot \vec{L}$ is the scalar product of the direction vector of light source \vec{L} and \vec{N} is the normal surface vector. b is a constant used to scale amplitude for metallic or shiny surfaces.

The specular reflection intensity is defined as

$$I_s = s \cdot (\vec{N} \cdot \vec{H})^{1/r}$$

Where s is the constant defining the reflectivity and parameter r defines the roughness of the surfaces which governs the sharpness of the reflected light. \vec{H} is the bisection vector between the direction of the light source \vec{L} and the direction of the reflected ray \vec{V} . Finally, both types of reflections are summed up for the signals in the modelled scene.

To calculate the intensity of the ray, the ray is traced backwards, which means that it starts from the sensor and continues its journey towards the object until it reaches the light source or is hindered by some geometrical object. A primary ray is constructed at the center of each pixel and the direction of travel for this ray is perpendicular to the image plane. Two types of information are saved during this tracing process: (1) the bounce level i.e. the number of ray-object intersections are accounted for and (2) the intensities of contributions are recorded which are normalized to unity. Most tedious task in terms of computations is the calculation of intensity after the intersection. If the ray (originating from one pixel) passes through one object, or it intersects two surfaces, then the surface with the shorter distance is treated as visible. Here the specular and diffuse reflections are calculated, these intensity values account for SAR image pixels (for the first level bounce). After this, a secondary ray is created at the intersection point and the count level for the number of bounces is incremented to two. The secondary ray has a decreased weight which depends on the reflectivity of the surface.

The tracing discontinues either when the minimum threshold level or maximum bounce level is reached or when there is a translucent object in the path way. The threshold limit and the maximum bounce level can be predefined as per requirement. The final summation of all contributions determines the intensity level for that pixel. The time

required for rendering such image is dependent on the resolution i.e. doubling the number of pixels requires four times as many rays to reach a bounce level of five.

To summarize, in the modified POV-Ray, the RaySAR, raytracing techniques are used to simulate SAR, where the object is modeled, and the depth information of the intersection point is calculated representing the slant range for a particular simulated image pixel. Basic SAR phenomenon like layover and foreshortening are incorporated by the use of an orthographic projection. Different bounce levels are also separated. As the resulting simulated data, azimuth location, range distance, amplitude value and the bounce level are stored for each ray traversed. For details of RaySAR one may refer to (Auer, Hinz and Bamler, 2010).

5.3. CAD Modelling Using Blender and Case Studies

Blender is a free and open-source 3D computer graphics software toolset used for creating animated films, interactive 3D applications, video games, visual effects, art and 3D printed models.

A wide variety of import and export scripts that extend Blender capabilities (accessing the object data via an internal application programming interface) make it possible to inter-operate with other 3D tools. This software was used for the modelling of the simulated structures.

5.3.1. Technical University Berlin ‘T-Building’

The ‘Telefunken Tower’ of the Technical University of Berlin was built from 1958 to 1960, it has 22 floors and a height of 80 meters. This building was chosen because of its orientation, symmetry and relative ease of modeling complexity. Facing east-west direction the front elevation of the structure is almost identical to the back and hence a similar signature can be expected from ascending and descending satellite passes in the SAR image.

In 2003, the Senate Departments of Economics and Urban Development of Berlin started the development and an implementation for the virtual 3D city model. To create the 3D model of the city, about 540,000 buildings on 890 square kilometers were photographed from the air, and their roofs were measured with lasers. Detailed models of about 200 buildings and attractions were created.

Through the download portal, one may request single building model as well as smaller areas of nine square kilometers in eight different data formats. The data of the Berlin 3D city model can be used as part of Berlin’s Open Data Initiative, free of cost and with several available formats. (*Berlin 3D City Model*, 2009)



Figure 74 Telefunken Tower as seen in the virtual city model

This downloaded model (Figure 74) was not useable directly as low-resolution optical images were used as textures on the top of the structure. The basic mesh structure was extracted from the building model and was taken into Blender for modifications. Having the already existing basic mesh beforehand, not only time was saved in modelling, but also the precise height and edges locations were localized with high accuracy. Further measurements were taken to get the dimensions of glass windows, metal bars and concrete pillars using manual geodetic methods. This step of modelling the fine details in the structure was important as the simulated image was to be compared with the actual one. The structure was separated into several layers while modelling, having different materials in each layer (Figure 76). It was also important to use a layered setup to assign different material properties for different type of materials used. After complete modelling the data was exported in the POV-Ray format, where glass, metal, concrete and ceramic were given different material and reflection properties (Table 14).



Figure 75 (Left) Optically acquired Telefunken building front view (Right bottom) close up view (Right top) Side view

Table 13 Time and Location for TSX image Acquisition

Coordinates / Time	Satellite pass	Azimuth	Incidence Angle	Sat Look /Pass Direction
52.511795° N 13.327393° E	2016-06-03 16:43:47	168.67°	29.74°	Right/Ascending
	2016-06-05 05:25:08	10.46°	36.30°	Right/Descending

Table 14 Materials and their properties used in the CAD modeling

Building Material	Electric Conductivity	Epsilon
Ceramic	1e-15	6
Concrete	-	-
Glass	1e-12	6.7
Metal (Lossy)	1.04e+007	-

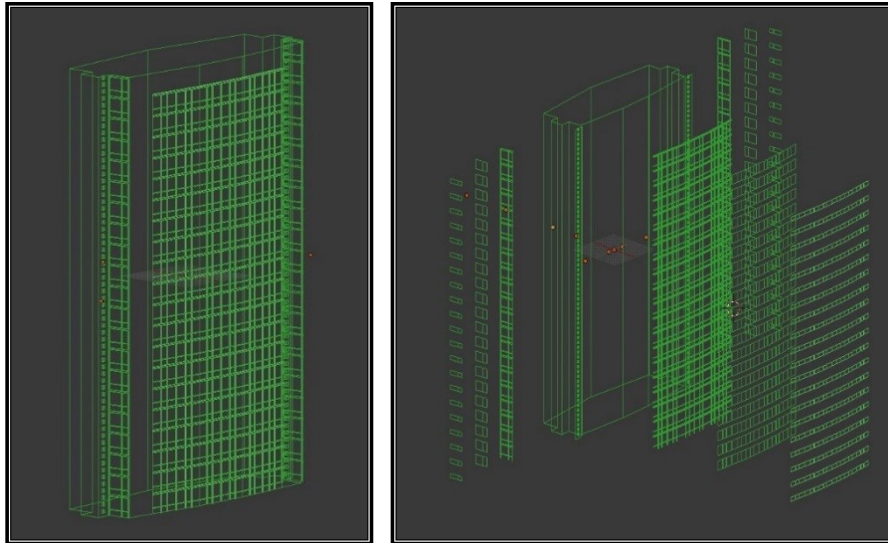


Figure 76 (Left) Modelled building (Right) Layers separated with respect to material types

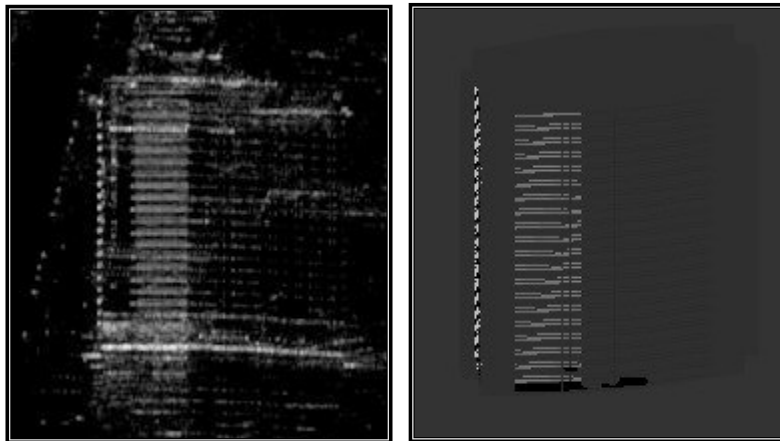


Figure 77 (Left) Acquired spotlight mode TSX image of the T-building (Right) Simulated T-building using Ray-SAR

TSX acquired image was cropped to select the T-building (Figure 77, left). The intensity of reflections was scaled logarithmically for a better visualization and for an equalized histogram of the image. As mentioned before, ESA's SNAP software is used to view and process SAR images. Figure 77 (right), is the simulated image of the same building. Twenty-two points seen in the vertical direction are mapped as the reflections originating from the metal bar running around the building on each floor. These reflections are the double bounce reflections as the metal bars are perpendicular to each other and acts as corner reflector having of a small surface area.

Although the building was modeled with quite an accuracy, some small features (roof top) were still not modeled as it was quite a tedious and time-consuming task.

The strong line at the base of the building (Figure 77, left) is not seen in the simulated image (Figure 77, right), moreover, the reflection pattern seen below this line is also not

seen in the simulated one. This strong baseline reflection and pattern under the building are missing as there is nothing modelled under as the base of the building.

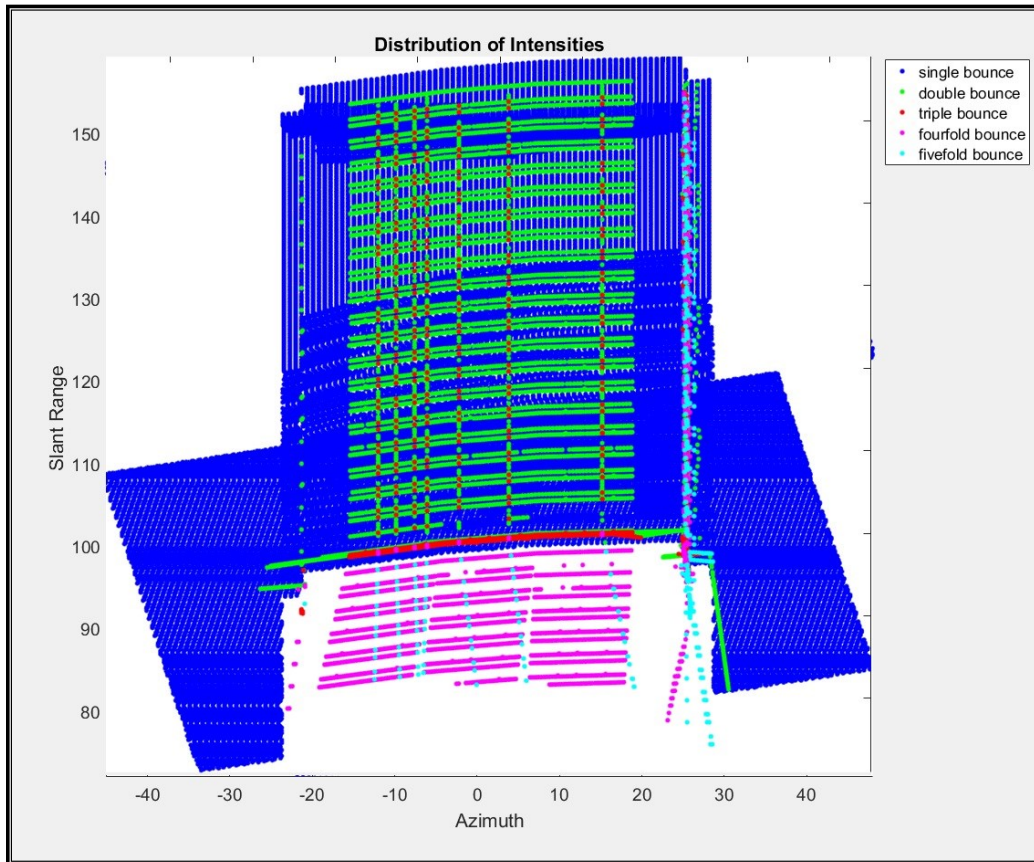


Figure 78 Detected phase centers projected onto the building with the bounce count using Ray-Sar

In the next step, the building is modelled with a base plate whose electrical properties are similar to those of stone and concrete with some surface irregularities. This is what the base of the building is essentially made up of. Seen in Figure 78, the phase centers of reflected rays are mapped onto the buildings where different number of bounce count are also separated. The addition of base plate to the building not only revealed strong triple fold reflections at the base line, also the pattern of reflection originating from the surface below the building was revealed. The blue color in the figure is a single bounce of the incident radiation, where very small energy is returned to the sensor and the rest is escaped. Similarly, green color is for double bounce and red for triple fold bounce.

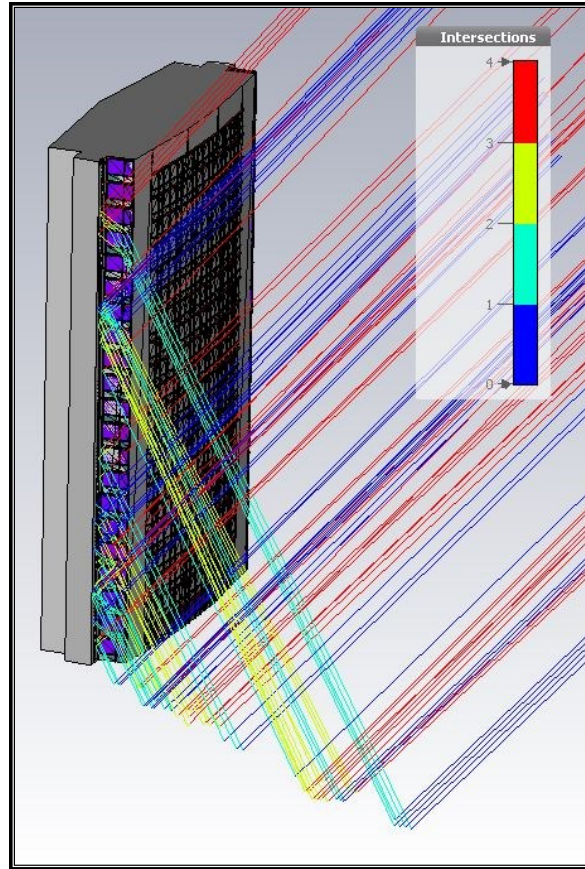


Figure 79 Visual representation of scatterers seen below the surface of the building in CST

Seen in Figure 79 is the visual representation of scatterers that were seen in the SAR image of the T-Building. The origin of reflection below the surface of building is due to the fourfold bounce as perceived in the image.

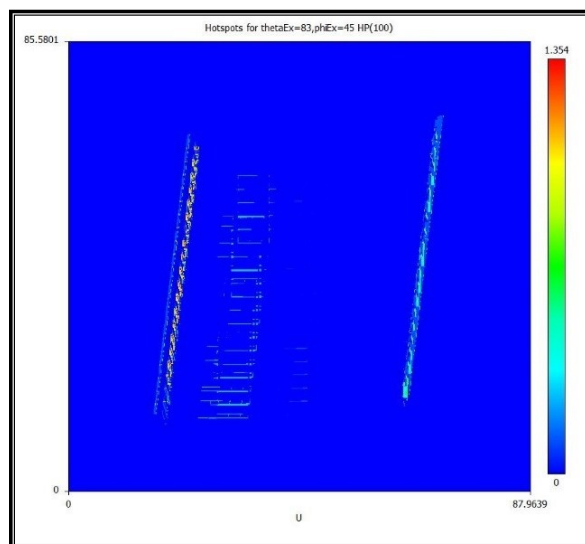


Figure 80 Hotspots referring to locations generating highest amplitude reflections using CST

The intensity of the reflected wave was mapped onto the building using CST software. Figure 80 reveals the touchable points on the building, called the hotspots which contributed to maximum backscatter. Figure 81 (right) details the up-close view of the metal railing from where the reflections are being originated. The fact that there are several rays along the metal railing is resulting in a much brighter spot seen in the SAR image (Figure 77, left). Even though the resolution of this SAR image is coarse, still we are having isolated, separated localized bright points as there is no reflection contribution from the vicinity of these railings. Close to these railings there is glass where the microwaves are penetrated into the building's inside.

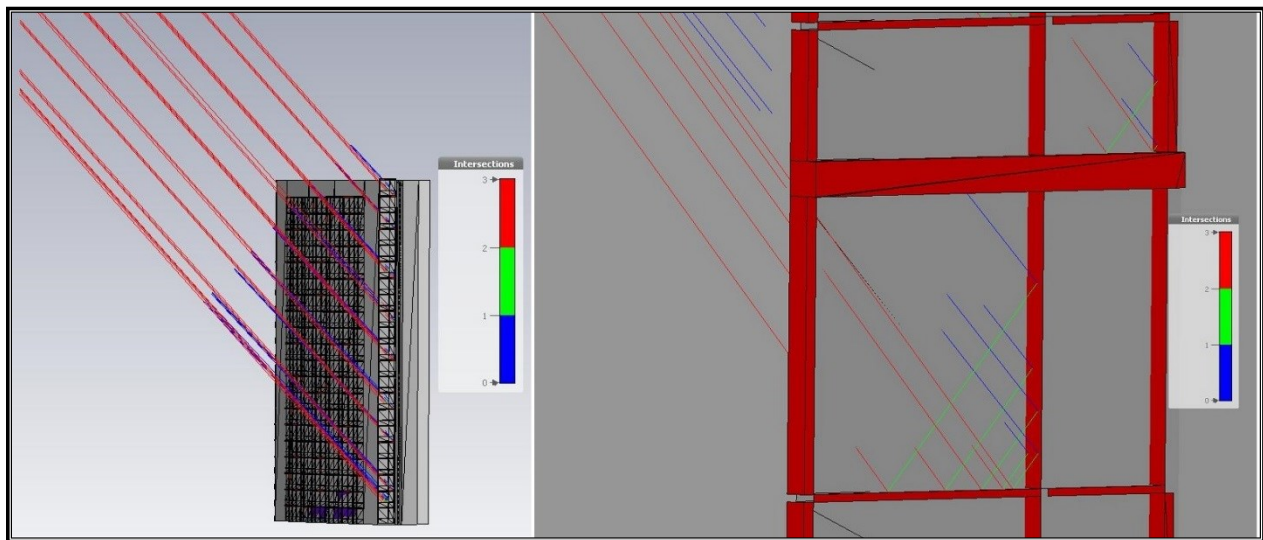


Figure 81 (Left) Overview of SBR incident onto the simulated structure (Right) Up-close view of metallic parts of building having highest amplitude contributions (CST)

5.3.2. Simplified Dome, Potsdam

In the urban architecture, domes or cupolas are structures seen usually on top of tall buildings, they provide a look-out view and may also serve as a source of light and air. The name is derived from a Latin word which resembles a cup that is upside down. Their existence in the current urban environment dates to the Roman empire. With the rise of Roman empire domes were not only constructed on the top of grand buildings but also religious buildings and cathedrals were symbolized with their presence. Having several of these structures in the city, its simulation was studied in detail revealing some insights for the SAR. Usually, it is a semi-spherical structure standing above the average scene height. It was expected that is unique SAR signature could easily be detected and localized. Moreover, having similar symmetrical geometry, it was also expected that these structures will be visible from ascending and descending satellite passes.

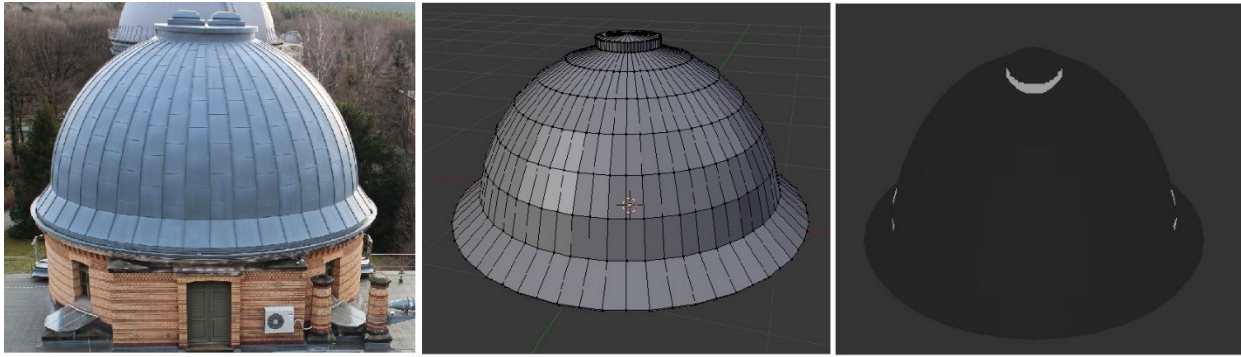


Figure 82 (Left) Optical image of dome of Astrophysical observatory, Telegraphenberg building. (Center) Modelled dome using Blender. (Right) Simulated image using RaySar

In the south-east of Potsdam in the 19th century a telegraph tower was erected at Telegraphenberg which was already at a height of 94 meters above average ground level. Astrophysical observatory is also a part of Telegraphenberg having three domes seen in Figure 83. TSX acquisition of this area was ordered with the highest possible resolution. The dome structure was modelled (Figure 82, center) and simulated with similar incidence angle as that of TSX acquisition. The circular expected structure was almost imperceptible in the simulated image. The reflection contributions were received only from the top notch of the dome which deviated from the regular spherical geometry (Figure 82, right).



Figure 83 Optical image of Telegraphenberg building, Potsdam (Google Maps, 2018b)

The acquired TSX image of this building is shown in Figure 84. Red highlighted circle in the SAR image is the area with the signature of the dome. This signature was similar to that of the simulated one where reflections were generated from top notch in a non-circular pattern. The factors degrading the simulation results are; modelling of dome without neighboring structures, the structure itself is not modelled according to the scale, the lack of speckle in the simulated image and the approximation of the surface roughness.



Figure 84 Acquired TSX's image of Telegrafenberg building, Potsdam

5.3.3. Dome, Charlottenburg Palace, Berlin

The largest palace of Berlin, Charlottenburg Palace, was built in the 17th century with huge gardens in the back and open area at the front (Figure 86). The building stands out from the neighboring architecture. On the top of the palace, there is a dome. This dome is relatively complex in architectural structure compared to previously simulated dome of Telegrafenberg building. The optical closeup image of the dome is shown in Figure 85(left). For this dome, the modelling was not done according to the original structure, neither was the precise model of the palace acquired, rather a very similar freely available CAD model was used instead. Material properties were modified, and dome was simulated. It was seen again, given this specific model, the origin of scatter was only from the area where the spherical shape of the structure was deviated from a theoretical sphere. The fine architectural designs at the top of the dome were contributing in the SAR signature (Figure 85, right). The small consecutive squares at the base of the dome resulted from the original square boxes that were modelled. The purpose of this model was a verification for the 'absence of the dome structure' within the SAR image. The acquired TSX can be seen in Figure 87. The red squared area with the signature of dome is again highlighted. Dome structure as simulated is not matched in the corresponding TSX acquisition. This un-identification is also due to the relative low resolution of TSX

compared to the simulated one. The continuous repetitive geometry almost always originating from window corners is visible in the SAR image (Figure 87).

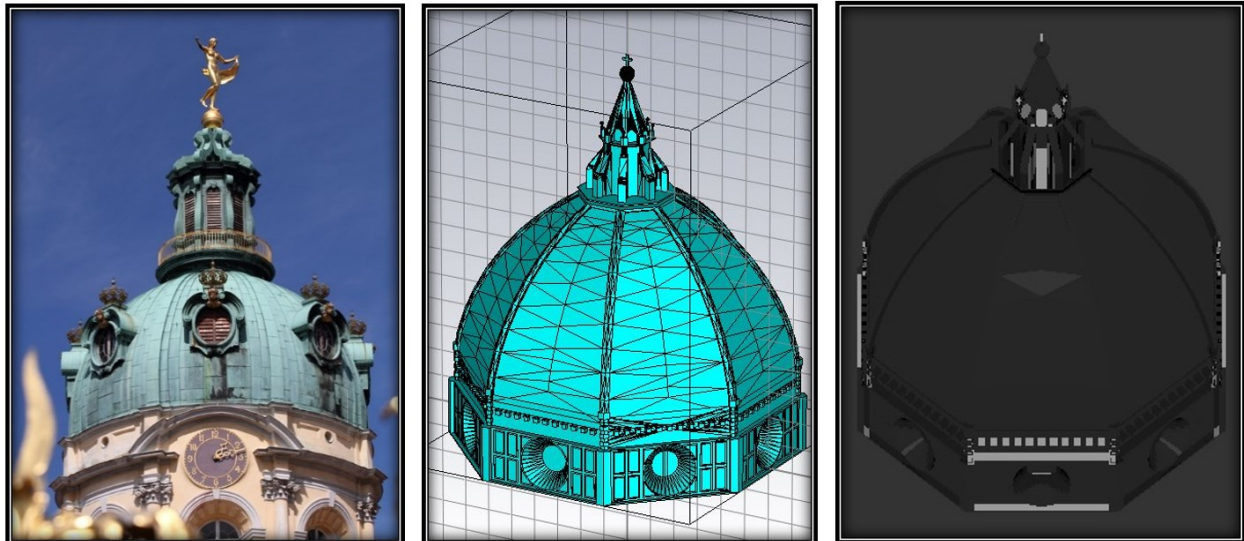


Figure 85 (Left) Optically acquired image of Charlottenburg's Palace's dome. (Middle) Similar readily available CAD model. (Right). Simulated SAR image using RaySar



Figure 86 Optical image of Charlottenburg's Palace, Berlin (Google Maps, 2018a)

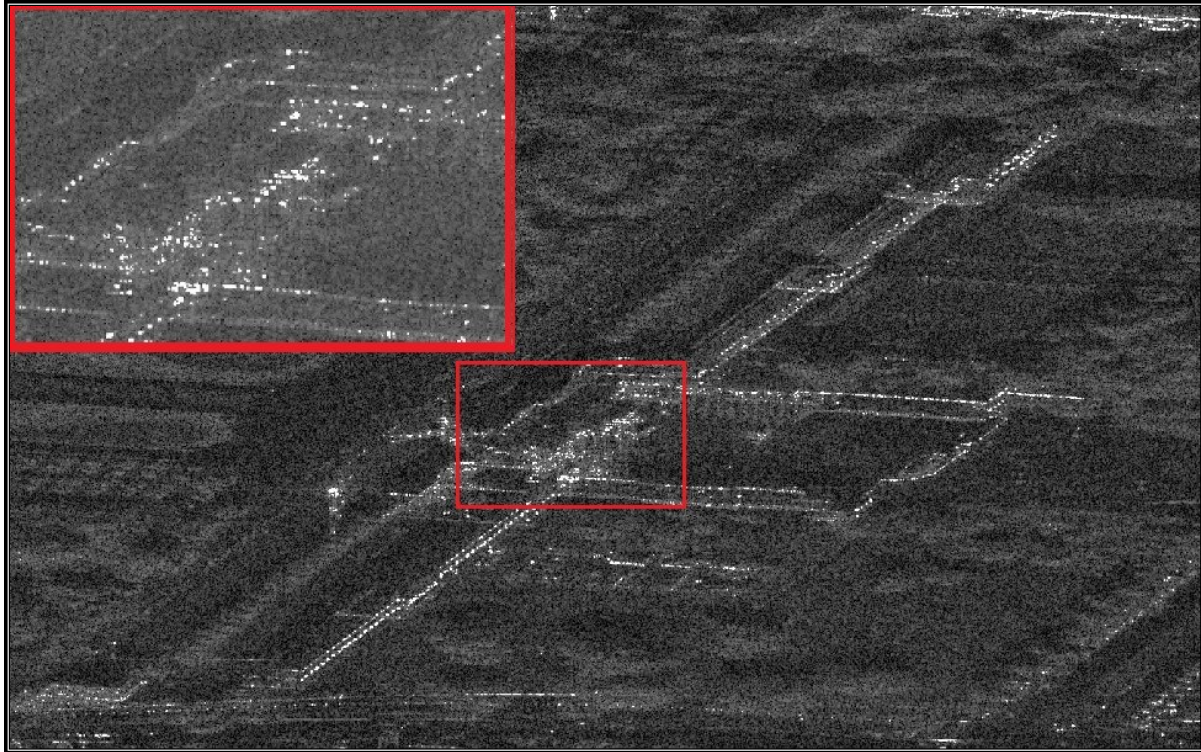


Figure 87 Acquired TSX's image of Charlottenburg's Palace, Berlin

5.3.4. The Snake Building, Berlin

Another architecture in Berlin caught our interest because of its unique shape. A 300 m long snake like building which curves back and forth along its length is a residential building for government employees located at the north bank of river spree in Berlin. Having more than 700 apartments the building was completed in 1999. Another motivation of selection of such a building was also its visibility in ascending and descending satellite SAR images.

Optical images of this building are seen in Figure 88. 3-d model of this building was again acquired from Berlin city model portal (*Berlin 3D City Model*, 2009). Details of the building were modelled on top of the basic downloaded structure, as in the original format several details were missing. Precise structure above the rooftop were not modelled as it required a lot more effort in acquiring and then modelling those details. Nonetheless, the unique pattern of window and its railings were modelled with accuracy using Blender (Figure 89).



Figure 88 Optical images of the Snake building, Berlin

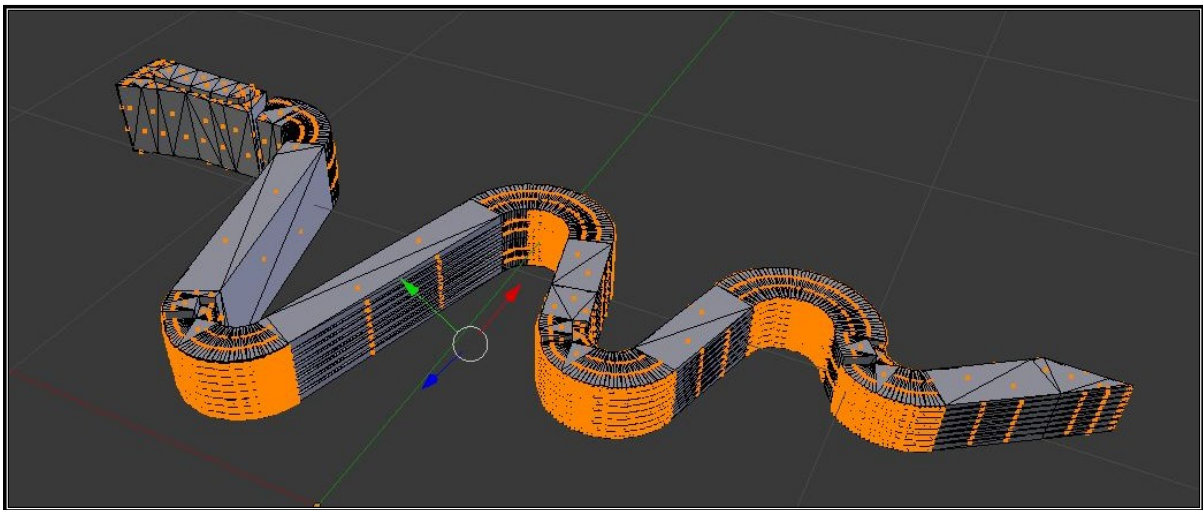


Figure 89 Modelled Snake building using Blender

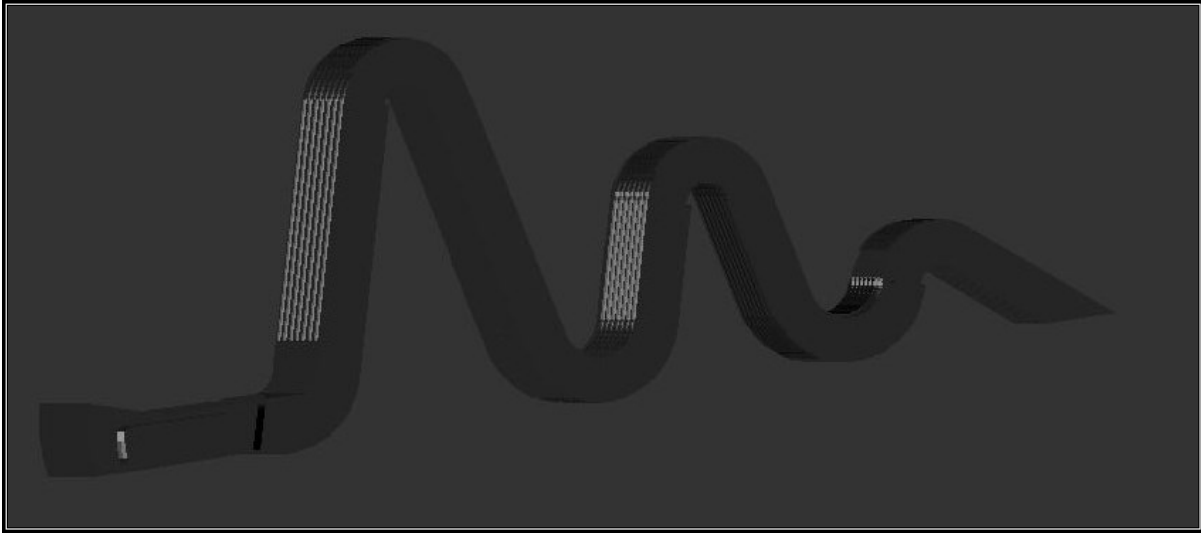


Figure 90 SAR simulated Snake building using RaySar

The resulting SAR simulation is seen in Figure 90 where the incidence and elevation angles were made similar to that of the real SAR acquisition. The metal railing at each floor level of the building was the most dominant contributor in the SAR image.

The building because of its design exhibited a unique signature pattern in the SAR image. This was clearly visible in the acquired TSX image over the area of Berlin (Figure 91).



Figure 91 Acquired TSX's of the snake building in Berlin

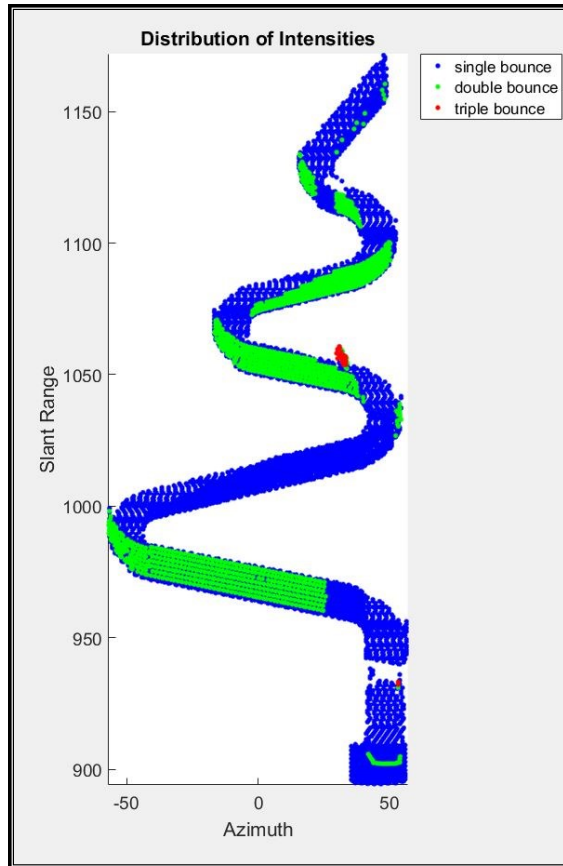


Figure 92 Detected phase centers projected onto the Snake building with the bounce count using RaySar

With the analysis of detected phase centers mapped onto the top of the building (Figure 92) it was observed that eight continuous horizontal lines were a result of the double bounce reflections originating from the metal railing.

Chapter 6: Summary and Future work

6.1. Summary

The aim of the current research was to determine the position of the real-world objects with a better accuracy using two or more SAR images acquired from both ascending and descending orbits. The challenge was finding the origin of SAR signature on complex building structures, given the fact that SAR image resolution was quite low even when acquired in highest possible resolution compared to that of optical imagery. Moreover, SAR images appeared unnatural to human viewers rendered it more complicated to identify real-world objects. Even though a symmetrical building was used, positioning unique common points visible in both ascending and descending images was not achieved. It was verified that what objects on the buildings are causing repetitive equidistant signature in the SAR image. Moreover, it was observed that a very small change in the acquisition geometry (a few degrees) rendered a quite different signature of the same object. The research question, what are the physically defined (touchable) points on the building contributing to the image was answered.

Selecting suitable material properties and varying them only impacted the amplitude of the SAR signal in the image. The novel method of SAR simulation, using CST, where time-domain solver was used, and relatively small objects were simulated, was useful in understanding the material and Electromagnetic signal interaction. Visualization of hotspots was a uniquely used method which verified the origin with the intensity of the pixels in the acquired SAR images.

The deviation in the inter-plate orthogonality was modelled for a CR and results were verified.

It was demonstrated that by the use of stereo image-based target localization, meter level accuracy was achieved. Where only errors of relatively larger magnitudes were incorporated.

An analysis for different types of simulators for of electromagnetics was made and a novel technique, use of CST for SAR simulation was introduced. Each step to perform a SAR simulation using this software was elaborated. Different types of available solvers were also discussed. Afterwards, the complex SAR focusing algorithm used in the processing of TSX images was compared with the simplified range doppler algorithm adapted for our simulation. Several simulation cases using single and multiple targets were performed. The unsuitability of such a simulator for large sized objects was stated. Possible sources of errors were discussed with their effect on the accuracy of simulation and methods to mitigate them.

A previously developed raytracing technique was used to simulate bigger sized objects and several urban buildings. A short introduction was given about RaySar which is a modified version of POV-ray. Some modeling details were also elaborated using another open source CAD tool named 'Blender'.

Various types of buildings were modeled in detail and then SAR simulated for ascending and descending orbits. The origin of reflection below the surface of building due to the fourfold bounce reflection was revealed. Dome-like structures were also modeled and simulated, and the results were analyzed having reference TSX data forehand. The non-visibility of a dome's radar signature was revealed and analyzed.

The factors degrading the simulation were highlighted. The fact that all the buildings were modelled without the neighboring structures. This ignored the inter-structural interaction of EM waves and hence neglecting the strong scatterers in the vicinity. Some structures were not modelled according to the scale, moreover, there was lack of speckle effect in the simulated images. An approximation of surface roughness for some parts of the building was used which also reduced the accuracy of simulation.

6.2. Future work

6.2.1. Modification and Testing of SAR Algorithms

A complete SAR processing algorithm was developed. This algorithm can be used for the purpose of training and can further be modified to incorporate advanced SAR techniques such a beam steering of starring spotlight mode. Several parameters of current SAR algorithm can be altered to the required need.

6.2.2. Calculation of ITRF Coordinates for the Scatterers

Obtaining precise coordinates of the simulated buildings was one of the goals of current research. Due to time constraints this goal was not accomplished and is left for future works.

6.2.3. Localization with Pole-Base

The use of CR in the localization of SAR images was a part of the current research. Construction of such reflectors require quite precision. Moreover, the mounting and installation process requires precise information about satellite acquisition, including orbital orientation and time. After the installation, reflectors are subject to weather conditions where strong winds can cause misalignments. As an alternate to the CR for localization, the installation of metal disc at the base of the pole both is suggested. In an urban environment existence of metallic poles is foreseeable with various purposes such as, traffic control lights, street lights, railway transmission lines, electricity transmission and distribution, telecommunication lines etc. Some of the obvious advantage of use of such metal disc at the base of existing poles include:

- Ease of installation and use of existing structures.
- Immune to misalignments.
- Prone to weather and environmental effects.
- Visibility from AD satellite orbits.
- High RCS for wide range of satellite look angles.

The selection of poles for the attachment of discs should be done with caution. The pole should be in an area where the view to the satellite is not hindered by the nearby buildings. Several such poles can serve as accurate control points for the localization of the SAR images. The coordinates of the selected poles can be measured by geodetic means. Knowing the precise diameter of the pole, the central point can be calculated with accuracy. Such a combination of pole and a metal base disc is modelled, and SAR simulated (Figure 93).

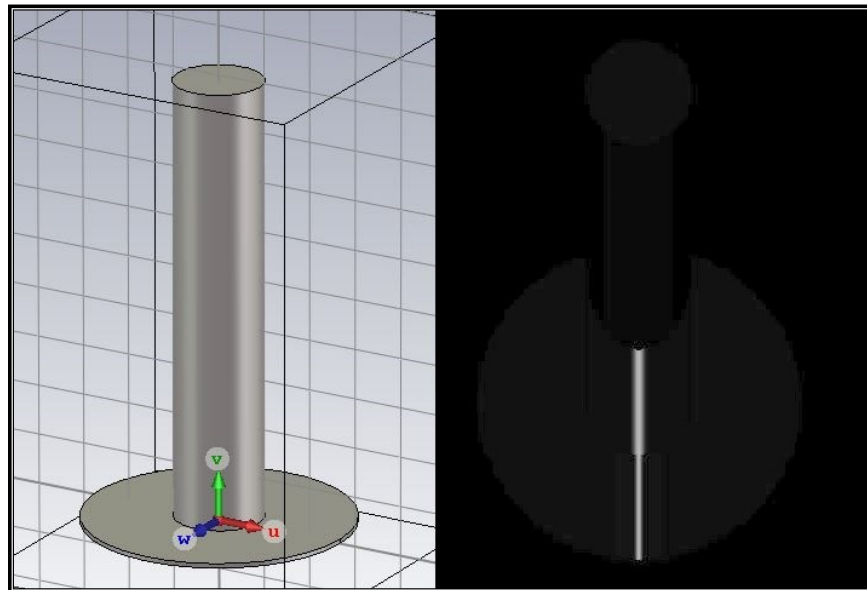


Figure 93 (Left) Modelled pole with metallic disc base. (Right) Simulated SAR signature of the corresponding image

Figure 94 shows the bounce levels for different elevational angles for the satellite. The azimuthal angle of the satellite does not need to be accounted for as the pole is symmetrically visible from all azimuthal angles. Figure 95 plots the RCS values of the pole-base for different satellite look angles. The RCS value is not high as compared to that of a CR, nonetheless it is much higher than minimum noise threshold of TSX (-23 dB), hence verifying the visibility of such a design for TSX satellite.

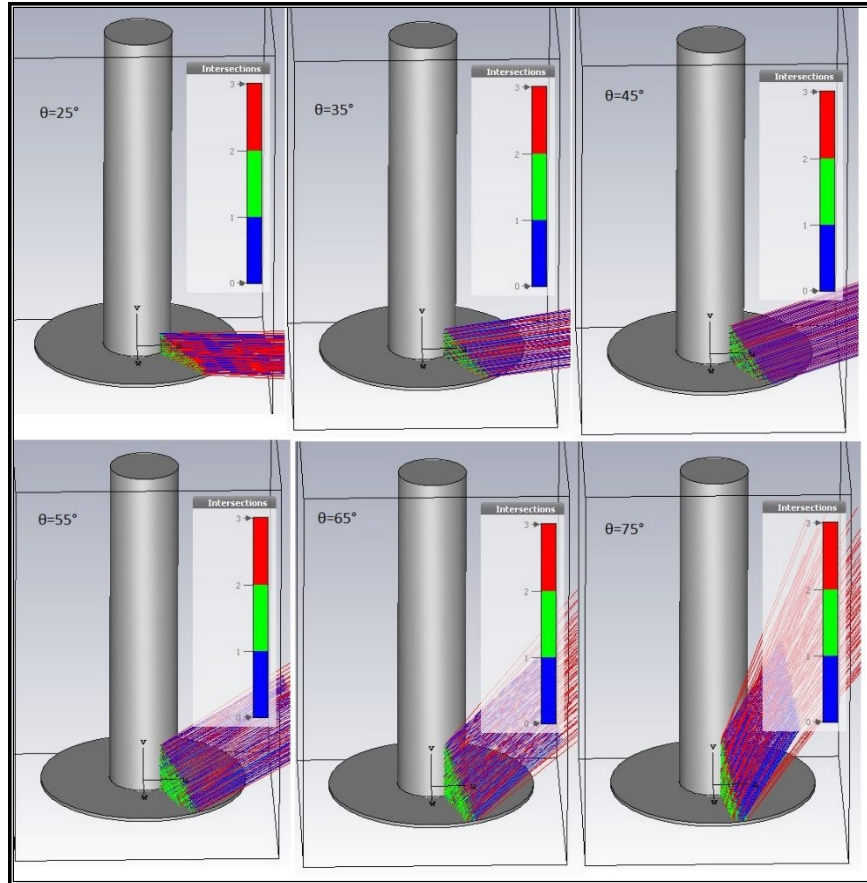


Figure 94 Bounce levels for different elevation angles for proposed setup

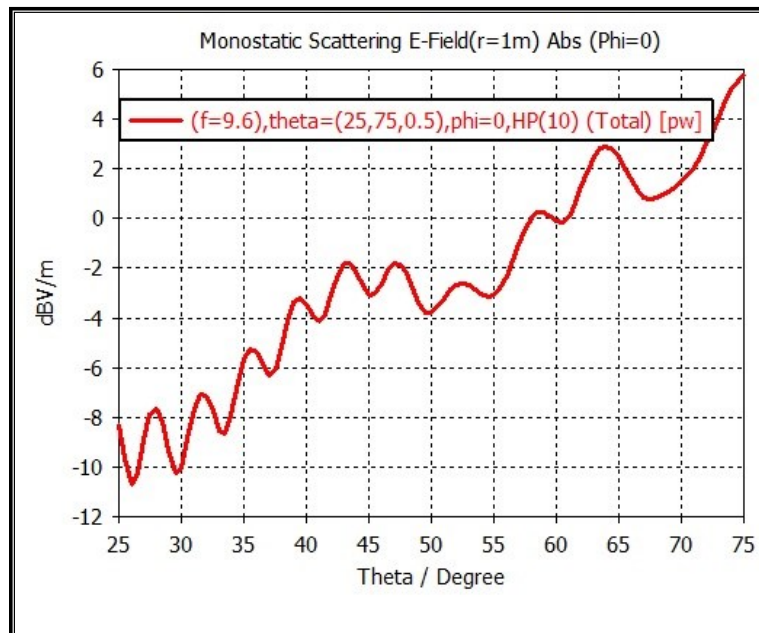


Figure 95 RCS measurements for different elevation angles

Appendix

Pov-Ray Modelling

Vectors and coordinates are declared in pointed brackets in POV-Ray, for example, $\langle 1.5, 4, 2 \rangle$. Vectors may also contain computational expressions where a large set of mathematical functions are available.

In Turbo Pascal one could write further procedures and functions and add files to the original instruction set in the form of units or include files. POV-Ray also provides such files and can be found in the include directory. These files should not be changed, but one may add files to this directory. They are included as e.g. *#include "colors.inc"*.

Camera consists of viewers viewing 'location' and viewpoint 'look_at' and is defined as:

- *camera {location $\langle 0,1,3 \rangle$ look_at $\langle 0,1,0 \rangle$ }*.

This defines the center and main beam of a perspective. The picture gets smaller as we move further outward. As a special effect, normal projections (orthographic), various cylindrical projections and spherical projections are available. Light source position and light color are defined as

- *light_source { $\langle 1000,1000, -1500 \rangle$ color white}*

Different types of light sources are available: point light, spotlight (which also emanates from a point light source, but works inside a cone), cylindrical light, light with parallel illumination and area light (a rectangular area with a number of light sources in the specific direction).

Objects can be modeled by defining geometric shapes, surface finish, reflection type, and other properties. Plane, sphere, box, cylinder, cone, torus, are the readily available basic shapes. They may undergo a geometric transformation to construct any geometry. With transformations, the basic bodies can be changed with regard to their position and form e.g.,

- scale - scale changes in xyz direction, *scale $\langle 1,2,3 \rangle$,*
- rotate - rotation around the origin, syntax for rotation by 30 ° about the x-axis, *rotate $\langle 30, 0, 0 \rangle$*
- translate - parallel shift, specified by shift vector; *translate $\langle 1,2,3 \rangle$*

For the surface finish of the object, the texture could be defined where color is must and translucency (if necessary), syntax:

- *pigment {color RGB $\langle 1, 0.5, 0.2 \rangle$ }*

The color is defined in RGB values (red-green-blue) where the maximum value is 1. The surface roughness (optional), e.g. grainy:

- *normal {bumps 0.075 scale 0.25}*.

Light conditions are defined by 'finish': ambient light 'ambient', light by illumination 'diffuse', reflections by 'reflection' and 'phong' provide highlights; e.g.:

- *texture {pigment {color RGB <1,0.65,0>} finish {ambient 0.15 diffuse 0.85 phong 1}}*

References

- Amanatides, J. and Woo, A. (1987) 'A Fast Voxel Traversal Algorithm for Ray Tracing', *Eurographics*, 87(3), pp. 3–10. doi: 10.1.1.42.3443.
- Auer, S., Gernhardt, S. and Bamler, R. (2011) 'Investigations on the nature of persistent scatterers based on simulation methods', *Joint Urban Remote Sensing Event, (JURSE)*, pp. 61–64. doi: 10.1109/JURSE.2011.5764719.
- Auer, S., Hinz, S. and Bamler, R. (2010) 'Ray-tracing simulation techniques for understanding high-resolution SAR images', *IEEE Transactions on Geoscience and Remote Sensing*, 48(3 PART2), pp. 1445–1456. doi: 10.1109/TGRS.2009.2029339.
- Auer, S. J. (2011) *3D Synthetic Aperture Radar Simulation for Interpreting Complex Urban Reflection Scenarios*.
- Balss, U. et al. (2013) 'Precise 2-D and 3-D Ground Target Localization With Terrasar-X', *ISPRS International Archives of the Photogrammetry, Remote Sensing and Spatial Information Sciences*, XL-1/W1(May), pp. 23–28. doi: 10.5194/isprsarchives-XL-1-W1-23-2013.
- Balss, U. et al. (2014) 'Precise measurements on the absolute localization accuracy of TerraSAR-X on the base of far-distributed test sites', in *European Conference on Synthetic Aperture Radar (EUSAR)*, pp. 993–996.
- Balz, T., Hammer, H. and Auer, S. (2015) 'Potentials and limitations of SAR image simulators – A comparative study of three simulation approaches', *ISPRS Journal of Photogrammetry and Remote Sensing*. International Society for Photogrammetry and Remote Sensing, Inc. (ISPRS), 101, pp. 102–109. doi: 10.1016/j.isprsjprs.2014.12.008.
- Balz, T. and Stilla, U. (2009) 'Hybrid GPU-Based Single- and Double-Bounce SAR Simulation', *IEEE Transactions on Geoscience and Remote Sensing*, 47(10), pp. 3519–3529.
- Berlin 3D City Model* (2009). Available at: <https://www.businesslocationcenter.de/berlin3d-downloadportal/#/export>.
- Breit, H. et al. (2010) 'TerraSAR-X SAR processing and products', *IEEE Transactions on Geoscience and Remote Sensing*, 48(2), pp. 727–740. doi: 10.1109/TGRS.2009.2035497.
- Brunner, D. et al. (2011) 'Radar imaging simulation for urban structures', *IEEE Geoscience and Remote Sensing Letters*, 8(1), pp. 68–72. doi: 10.1109/LGRS.2010.2051214.
- Brunner, D., Lemoine, G. and Bruzzone, L. (2010) 'Earthquake damage assessment of buildings using VHR optical and SAR imagery', in *IEEE Transactions on Geoscience and Remote Sensing*, pp. 2403–2420.
- Chang, Y.-C., Datchev, I. and Habib, A. (2009) 'A photogrammetric system for 3-D

reconstruction of a scoliotic torso', in *American Society of Photogrammetry and Remote Sensing*, pp. 126–137. Available at: [http://www.ucalgary.ca/engo_webdocs/AH/08.20274.YC\(David\)Chang.pdf](http://www.ucalgary.ca/engo_webdocs/AH/08.20274.YC(David)Chang.pdf).

Chang, Y., Chiang, C. and Chen, K. (2011) 'SAR image simulation with application to target recognition', *Progress In Electromagnetics Research*, 119(July), pp. 35–57. doi: 10.2528/PIER11061507.

Cong, X. *et al.* (2012) 'Imaging geodesy-centimeter-level ranging accuracy with TerraSAR-X: An update', *IEEE Geoscience and Remote Sensing Letters*, 9(5), pp. 948–952. doi: 10.1109/LGRS.2012.2187042.

CST (2010) 'Understanding Time Domain Meshing in CST MICROWAVE STUDIO', *Elements*. CST, pp. 1–17.

Cuenca, M. C. *et al.* (2014) 'Deployment and design of bi-directional corner reflectors for optimal ground motion monitoring using InSAR', in *European Conference on Synthetic Aperture Radar (EUSAR)*, pp. 378–381.

Cumming, I. G. and Wong, F. H. (2005) *Digital processing of synthetic aperture radar data*. Boston: Artech House.

DLR (2015) *TerraSAR-X or TanDEM-X reference target alignment angles*. Available at: <https://sar-calibration.dlr.de/>.

Eineder, M. *et al.* (2011) 'Imaging geodesy - Toward centimeter-level ranging accuracy with TerraSAR-X', *IEEE Transactions on Geoscience and Remote Sensing*, 49(2), pp. 661–671.

Franceschetti, G. *et al.* (1992) 'SARAS: A Synthetic Aperture Radar (SAR) Raw Signal Simulator', *IEEE Transactions on Geoscience and Remote Sensing*, 30(1), pp. 110–123. doi: 10.1109/36.124221.

Franceschetti, G. *et al.* (2003) 'SAR raw signal simulation for urban structures', *IEEE Transactions on Geoscience and Remote Sensing*, 41(9), pp. 1986–1995. doi: 10.1109/TGRS.2003.814626.

Franceschetti, G., Migliaccio, M. and Riccio, D. (1994) 'SAR raw signal simulation of actual ground sites described in terms of sparse input data', *IEEE Transactions on Geoscience and Remote Sensing*, 32(6), pp. 1160–1169. doi: 10.1109/36.338364.

Franceschetti, G., Migliaccio, M. and Riccio, D. (1995) 'The SAR Simulation: an Overview', in *International Geoscience and Remote Sensing Symposium*, pp. 2283–2285.

Fritz, T., Breit, H. and Eineder, M. (2008) 'TerraSAR-X Products – Tips and Tricks', in *TerraSAR-X Workshop*, p. 61.

Gisinger, C. *et al.* (2015) 'Precise Three-Dimensional Stereo Localization of Corner Reflectors and Persistent Scatterers With TerraSAR-X', *IEEE Transactions on Geoscience and Remote Sensing*, 53(4), pp. 1782–1802.

Gisinger, C. *et al.* (2017) 'Differential geodetic stereo SAR with TerraSAR-X by exploiting small multi-directional radar reflectors', *Journal of Geodesy*. Springer Berlin Heidelberg, 91(1), pp. 53–67. doi: 10.1007/s00190-016-0937-2.

Gold, G. and Helmreich, K. (2012) 'A physical model for skin effect in rough surfaces', in *European Microwave Conference (EuMC)*, pp. 1011–1014. Available at: http://ieeexplore.ieee.org/xpls/abs_all.jsp?arnumber=6459235.

Google Maps, I. (2018a) *Schloss Charlottenburg*. Available at: <https://www.google.de/maps/@52.5184977,13.2916485,291a,35y,46.41h,47.87t/data=!3m1!1e3> (Accessed: 12 June 2018).

Google Maps, I. (2018b) *Telegrafenberg Potsdam*. Available at: <https://www.google.de/maps/@52.3810431,13.0631371,84a,35y,126.56h,48.75t/data=!3m1!1e3> (Accessed: 12 June 2018).

Gray, A. L. *et al.* (1990) 'Synthetic aperture radar calibration using reference reflectors', *Geoscience and Remote Sensing, IEEE Transactions on*, 28(3), pp. 374–383. doi: 10.1109/36.54363.

Hammer, H., Kuny, S. and Schulz, K. (2014) 'Amazing SAR Imaging Effects – Explained by SAR Simulation 3 SAR phenomena and their explanation using SAR simulation', in *European Conference on Synthetic Aperture Radar (EUSAR)*. VDE, pp. 1105–1108.

Hammer, H. and Schulz, K. (2009) 'Coherent simulation of SAR images', in *Image and Signal Processing for Remote Sensing*. SPIE Remote Sensing, pp. 1–9. doi: 10.1117/12.830380.

Jakowatz, C. V. *et al.* (no date) *Spotlight-Mode Synthetic Aperture Radar: A Signal Processing Approach*. Springer.

Jehle, M. *et al.* (2008) 'Estimation of atmospheric path delays in TerraSAR-X data using models vs. measurements', *Sensors*, 8(12), pp. 8479–8491. doi: 10.3390/s8128479.

Lai, T. L., Robbins, H. and Wei, C. Z. (1978) 'Strong consistency of least squares estimates in multiple regression', *Proceedings of the National Academy of Sciences of the United States of America*. Available at: https://en.wikipedia.org/wiki/Linear_least_squares.

Leberl, F. (1990) *Radargrammetric image processing, SERBIULA (sistema Librum 2.0)*. Boston, London: Artech House.

Lee, S. W. (1989) 'Shooting and Bouncing Rays: Calculating the RCS of an Arbitrarily Shaped Cavity', *IEEE Transactions on Antennas and Propagation*, pp. 194–205. doi: 10.1109/8.18706.

Di Martino, G. *et al.* (2007) 'Disaster monitoring by extracting geophysical parameters from SAR data', *International Geoscience and Remote Sensing Symposium (IGARSS)*, pp. 4948–4952. doi: 10.1109/IGARSS.2007.4423972.

Mishra, A. and Mulgrew, B. (2009) 'Generation of SAR Image for Real-life Objects using

General Purpose EM Simulators', in *IETE Technical Review*, p. 18. doi: 10.4103/0256-4602.48465.

Mittermayer, J. *et al.* (1999) 'Spotlight SAR data processing using the frequency scaling algorithm', *IEEE Transactions on Geoscience and Remote Sensing*, 37(5), pp. 2198–2214. doi: 10.1109/36.789617.

Mittermayer, J., Lord, R. and Borner, E. (2003) 'Sliding spotlight SAR processing for TerraSAR-X using a new formulation of the extended chirp scaling algorithm', *IEEE International Geoscience and Remote Sensing Symposium*, 3(C), pp. 1462–1464. doi: 10.1109/IGARSS.2003.1294144.

Moreira, A., Mittermayer, J. and Scheiber, R. (1996) 'Extended chirp scaling algorithm for air and spaceborne SAR data processing in stripmap and ScanSAR imaging modes', *IEEE Transactions on Geoscience and Remote Sensing*, 34(5), pp. 1123–1136. doi: 10.1109/36.536528.

Neff, C. A. (1990) 'Finding the distance between two circles in three-dimensional space', *IBM Journal of Research & Development*, 34(5), pp. 770–775. doi: <http://dx.doi.org/10.1147/rd.345.0770>.

Quin, G. and Loreaux, P. (2013) 'Submillimeter Accuracy of Multipass Corner Reflector Monitoring by PS Technique', *IEEE Transactions on Geoscience and Remote Sensing*, 51(3), pp. 1775–1783. doi: 10.1109/TGRS.2012.2206600.

Ray tracing (graphics) (2008). Available at: https://en.wikipedia.org/wiki/File:Ray_trace_diagram.svg.

Reigber, A. and Hellwich, O. (2004) 'RAT (Radar Tools): A free SAR image analysis software package', in *European Conference on Synthetic Aperture Radar (EUSAR)*, pp. 1–4.

Roth, A., Huber, M. and Kosmann, D. (2004) 'Geocoding of TerraSAR-X data', *Proceedings of the International Society for Photogrammetry and Remote Sensing Congress*, pp. 840–844. doi: 10.1.1.1.122.7570.

Speck, R., Turchi, P. and Süß, H. (2007) 'An end-to-end simulator for high-resolution spaceborne SAR systems', *Proceedings of SPIE - The International Society for Optical Engineering*, 6568, pp. 1–8. doi: 10.1117/12.717222.

Tsang, L., Kong, J. and Shin, R. (1985) *Theory of microwave remote sensing*. New York: J. Wiley & Sons. Available at: <http://ntrs.nasa.gov/search.jsp?R=19850058641>.

Tupin, F., Bloch, I. and Maitre, H. (1999) 'A first step toward automatic interpretation of sar images using evidential fusion of several structure detectors', *IEEE Transactions on Geoscience and Remote Sensing*, 37(3 I), pp. 1327–1343. doi: 10.1109/36.763297.

Wefelscheid, C., Hänsch, R. and Hellwich, O. (2012) 'Three-dimensional building reconstruction using images obtained by unmanned aerial vehicles', *ISPRS International*

Archives of the Photogrammetry, Remote Sensing and Spatial Information Sciences
International Archives of the Photogrammetry, Remote Sensing and Spatial Information
Sciences, XXXVIII-1/(1/C22), pp. 183–188. doi: 10.5194/isprsarchives-XXXVIII-1-C22-183-2011.

Wohlers, M. *et al.* (1980) 'Computer simulation of synthetic aperture radar images of three-dimensional objects', *IEEE Transactions on Aerospace and Electronic Systems*, AES-16(3), pp. 258–271. doi: 10.1109/TAES.1980.308894.

Wu, F., Wang, C. and Wen, X. (2016) 'SAR Image Simulation for Object ' s Feature Analysis', in *International Workshop on Earth Observation and Remote Sensing Applications*, pp. 1–5.

Zhang, L., Balz, T. and Liao, M. (2012) 'Satellite SAR geocoding with refined RPC model', *ISPRS Journal of Photogrammetry and Remote Sensing*. International Society for Photogrammetry and Remote Sensing, Inc. (ISPRS), 69, pp. 37–49. doi: 10.1016/j.isprsjprs.2012.02.004.

Zhu, X. X. *et al.* (2014) 'Geodetic TomoSAR - Fusion of SAR imaging geodesy and TomoSAR for 3D absolute scatterer positioning', *International Geoscience and Remote Sensing Symposium*, (4), pp. 1317–1320. doi: 10.1109/IGARSS.2014.6946676.

Van Zyl, J. J. (1990) 'Calibration of polarimetric radar images using only image parameters and trihedral corner reflector responses', *IEEE Transactions on Geoscience and Remote Sensing*, 28(3), pp. 337–348. doi: 10.1109/36.54360.

List of Figures

Figure 1 SAR Geometry	7
Figure 2 SAR Switching Operation	8
Figure 3 RAW data in a 2-D Array	11
Figure 4 SAR Geometry 2-d Illustration.....	12
Figure 5 Raw Data Matrix	13
Figure 6 Single house target visualization	14
Figure 7 One (top) and Three (bottom) point targets Raw Data	14
Figure 8 SAR Focusing	15
Figure 9 SAR Processing real dataset	16
Figure 10 SAR processor coherent summation block diagram	19
Figure 11 Doppler Frequency	21
Figure 12 Phase history of a scatterer: coherent (b) and non-coherent (c) summation	23
Figure 13 Phase and amplitude illustrated.....	24
Figure 14 Flow chart SAR processing (frequency domain)	26
Figure 15 Two scatters visualized in raw data matrix	27
Figure 16 Point target after compression in SLC image	27
Figure 17 Range cell migration curve	28
Figure 18 SAR simulated example	29
Figure 19 Multibook Processing.....	32
Figure 20 One look vs nine looks	33
Figure 21 Spotlight mode in SAR processing	34
Figure 22 Overview TMSP Level-0 SAR Data screening process (Breit et al., 2010)	38
Figure 23 Overview TMSP Level 1 SAR data process (Breit et al., 2010)	38
Figure 24 Elevation angles for a horizontally placed CR (RCS calculation).....	43
Figure 25 (Left) RCS in Azimuth (CR without gap); (Right) RCS in Azimuth (CR with gap)	44
Figure 26 Inter-plate orthogonality deviation modelled for RCS calculation	45
Figure 27 RCS results for different degrees of deviation of α	45
Figure 28 RCS results for different degrees of deviation of β	46
Figure 29 Corner Reflector Pair (Zero Elevation)	48
Figure 30 Corner Reflector Pair (30° Elevated)	48
Figure 31 Side view and front view of the reflector with small triangular plates (0.5m side length) assembled together to form a bigger reflector (1m side length)	49
Figure 32 Mounted reflectors viewing in different orbital directions	50
Figure 33 CR as seen in the high resolution TSX image from the ascending orbital pass	50

Figure 34 CR as seen in the high resolution TSX image from the descending orbital pass	51
Figure 35 Azimuthal orientation (DLR, 2015)	51
Figure 36 Elevational orientation (DLR, 2015).....	52
Figure 37 Point target analysis (ascending orbital acquisition).....	53
Figure 38 Point target analysis (descending orbital acquisition).....	54
Figure 39 Range circles at zero Doppler, (green) ascending orbit, (red) descending orbit	57
Figure 40 Range circles with earth surface and the intersection point	57
Figure 41 Flowchart summarizing the process of localization using double corner reflectors	61
Figure 42 Overview of the two-distinct types of SAR simulators	64
Figure 43 Overview SARAS: a raw signal simulator.....	65
Figure 44 Trihedral reflector as seen in CST design environment	71
Figure 45 Boundary condition dialogue box as seen in CST	71
Figure 46 Symbols representing Electric, Magnetic, Open, Open with space and Periodic boundaries.....	72
Figure 47 Defining a symmetry plane vertically across the reflector	73
Figure 48 Calculation domain divided into dual grid cells	76
Figure 49 Leapfrog grid voltage calculation	76
Figure 50 Processing steps in TSX image focusing performed at the ground station (Breit, H. et al 2004)	78
Figure 51 Simplified SAR processing for the simulated data implementing the Range Doppler Algorithm	79
Figure 52 Plane wave excited by chirp, incident on a single sphere	81
Figure 53 (Left) Transmitted chirp signal. (Right) Received signal after being reflected from sphere	82
Figure 54 Range compression for a single pulse reflected by a sphere	82
Figure 55 Unprocessed RAW data as collected from a single sphere	83
Figure 56 Raw data compressed in the range direction via convolution, range cell migration curve is evident for a single sphere	83
Figure 57 Final processed SAR image for single sphere (magnified).....	84
Figure 58 Plane wave excited by chirp, incident on a modelled corner reflector	84
Figure 59 Far field probes at the boundary to receive the scattered EM signal	85
Figure 60 (Left) Transmitted chirp signal. (Right) Received signal after being reflected from CR.....	85
Figure 61 Range compression for a single pulse reflected by a CR.....	86
Figure 62 Unprocessed RAW data as collected from a CR.....	86
Figure 63 Raw data compressed in the range direction via convolution	86
Figure 64 Range Cell Migration curve, because of SAR acquisition geometry	87
Figure 65 Corrected Range cell migration curve.....	87

Figure 66 Final processed SAR image	88
Figure 67 Plane wave excited by chirp, incident on three modelled spheres at same range	88
Figure 68 Unprocessed raw data as collected from three equidistant spheres	89
Figure 69 Raw data compressed in the range direction via convolution, three range cell migration curves are evident each for a sphere	89
Figure 70 Final processed SAR image for three spheres (magnified)	90
Figure 71 Overview of a Ray-tracer with a projection of 3-d object onto a 2-d plane (Ray tracing (graphics), 2008)	93
Figure 72 Overview Ray-Sar: a direct image simulator	95
Figure 73 Vectors for calculating reflection and related effects	96
Figure 74 Telefunken Tower as seen in the virtual city model	99
Figure 75 (Left) Optically acquired Telefunken building front view (Right bottom) close up view (Right top) Side view	100
Figure 76 (Left) Modelled building (Right) Layers separated with respect to material types.....	101
Figure 77 (Left) Acquired spotlight mode TSX image of the T-building (Right) Simulated T-building using Ray-SAR.....	101
Figure 78 Detected phase centers projected onto the building with the bounce count using Ray-Sar	102
Figure 79 Visual representation of scatterers seen below the surface of the building in CST	103
Figure 80 Hotspots referring to locations generating highest amplitude reflections using CST	103
Figure 81 (Left) Overview of SBR incident onto the simulated structure (Right) Up-close view of metallic parts of building having highest amplitude contributions (CST)	104
Figure 82 (Left) Optical image of dome of Astrophysical observatory, Telegraphenberg building. (Center) Modelled dome using Blender. (Right) Simulated image using RaySar	105
Figure 83 Optical image of Telegrafenberg building, Potsdam (Google Maps, 2018b)	105
Figure 84 Acquired TSX's image of Telegrafenberg building, Potsdam	106
Figure 85 (Left) Optically acquired image of Charlottenburg's Palace's dome. (Middle) Similar readily available CAD model. (Right). Simulated SAR image using RaySar	107
Figure 86 Optical image of Charlottenburg's Palace, Berlin (Google Maps, 2018a)	107
Figure 87 Acquired TSX's image of Charlottenburg's Palace, Berlin	108
Figure 88 Optical images of the Snake building, Berlin	109
Figure 89 Modelled Snake building using Blender	109
Figure 90 SAR simulated Snake building using RaySar	110
Figure 91 Acquired TSX's of the snake building in Berlin	110
Figure 92 Detected phase centers projected onto the Snake building with the bounce count using RaySar	111

Figure 93 (Left) Modelled pole with metallic disc base. (Right) Simulated SAR signature of the corresponding image 114
Figure 94 Bounce levels for different elevation angles for proposed setup 115
Figure 95 RCS measurements for different elevation angles 115

List of Tables

Table 1 Summarizing the orbital parameters of the TSX satellite	37
Table 2 Launch site, date and other spacecraft properties for TSX	37
Table 3 Azimuth resolution for TSX in different modes	39
Table 4 CST Simulated RCS at different elevations for corner reflector	44
Table 5 RCS comparison at different deviation angles.....	47
Table 6 Time and location for TSX image acquisition	49
Table 7 Annotated signal propagation effects.....	58
Table 8 Atmospheric delay corrections applied	58
Table 9 Summarizing the sources of errors in localization and the stage where they are corrected.	59
Table 10 Precise measurements of experimental setup	59
Table 11 Geodetic surveyed location of installed reflectors and ranging error	60
Table 12 Material properties of Aluminum used in the simulation	70
Table 13 Time and Location for TSX image Acquisition.....	100
Table 14 Materials and their properties used in the CAD modeling	100

List of Abbreviations

CAD	Computer aided design
CR	Corner reflector
DCR	Double corner reflector
DEM	Digital elevation map
DLR	Deutschen Zentrums für Luft und Raumfahrt (German aerospace center)
ECEF	Earth centered earth fixed coordinates
ERS	European Remote-Sensing Satellite
GPS	Global positioning system
PO	Physical optics
POV	Persistence of vision
PRF	Pulse repetition frequency
RCS	Radar cross section
SAR	Synthetic-aperture radar
TSX	TerraSAR-X (Imaging radar Earth observation satellite)